

The kaobook class

Use this document as a template

Millikelvin Confocal Microscopy of Semiconductor Membranes and Filter Functions for Unital Quantum Operations

Customise this page according to your needs

Tobias Hangleiter*

August 15, 2025

* A \LaTeX lover/hater

The harmony of the world is made manifest in Form and Number, and the heart and soul and all the poetry of Natural Philosophy are embodied in the concept of mathematical beauty.

– D'Arcy Wentworth Thompson

Contents

Contents	iii
I A FLEXIBLE PYTHON TOOL FOR FOURIER-TRANSFORM NOISE SPECTROSCOPY	1
II CHARACTERIZATION AND IMPROVEMENTS OF A MILLIKELVIN CONFOCAL MICROSCOPE	2
III OPTICAL MEASUREMENTS OF ELECTROSTATIC EXCITON TRAPS IN SEMICONDUCTOR MEMBRANES	3
1 Introduction	4
2 Photoluminescence and excitons in semiconductors	8
2.1 Photoluminescence in doped GaAs/Al _x Ga _{1-x} As heterostructures	8
2.2 The quantum-confined Stark effect	10
2.2.1 In-plane confinement	11
2.3 Excitonic complexes	14
3 The mjolnir measurement framework	16
3.1 Rationale	16
3.2 Instrument abstraction	16
3.2.1 Excitation path	18
3.2.2 Detection path	18
3.2.3 Sample	18
3.3 Calibrations	18
3.3.1 CCD calibration	19
3.3.2 Power calibration	19
3.3.3 Rejection feedback	20
3.4 Measurement routines	21
3.5 Plotting	22
4 Photoluminescence measurements of doped semiconductor membranes	24
4.1 Photoluminescence spectroscopy	25
4.1.1 Quantum-confined Stark shift	26
4.1.2 Power dependence	28
4.1.3 Spatial dependence	31
4.2 Photoluminescence excitation spectroscopy	33
4.3 Transfer-matrix method simulations of the heterostructure membrane	36
4.3.1 Electric fields in layered thin films	37
4.3.2 Quantum well absorptance	39
4.3.3 Field emission	40
5 Conclusion & outlook	42
IV A FILTER-FUNCTION FORMALISM FOR UNITAL QUANTUM OPERATIONS	46

APPENDIX	47
A Dependence of TMM simulations on epoxy thickness	48
B Additional measurements	49
B.1 Self-consistent Poisson-Schrödinger simulation of the membrane band structure	49
B.2 Additional data	49
B.2.1 Combined plot of PL and PLE data	49
B.2.2 2DEG PL as function of power	50
Bibliography	51
List of Terms	59
Declaration of Authorship	61

List of Figures

2.1	Generated by img/py/experiment/pl.py.	9
2.2	Generated by img/py/experiment/qcse.py.	10
2.3	Generated by img/py/experiment/qcse.py.	11
2.4	Generated by img/py/experiment/qcse.py.	12
2.5	Generated by img/py/experiment/qcse.py.	14
3.1	Generated by img/tikz/experiment/mjolnir_instruments.tex.	17
3.2	Generated by img/tikz/experiment/mjolnir_tree.tex.	18
3.3	Generated by img/py/experiment/calibration.py.	20
3.4	Generated by img/py/experiment/pl.py.	23
4.1	Sample: DOPED M1_05_49-2. $\lambda_{\text{exc}} = 795 \text{ nm}$. $P = 0.92 \mu\text{W}$. Generated by img/py/experiment/pl.py.	25
4.2	Sample: HONEY H13. $\lambda_{\text{exc}} = 795 \text{ nm}$. $P = 1 \mu\text{W}$. Generated by img/py/experiment/pl.py.	26
4.3	Sample: DOPED M1_05_49-2. $V_{\text{CM}} = -1.3 \text{ V}$. $\lambda_{\text{exc}} = 795 \text{ nm}$. $P = 10 \mu\text{W}$. Generated by img/py/experiment/pl.py.	27
4.4	Sample: DOPED M1_05_49-2. $V_{\text{DM}} = -2.7 \text{ V}$. $V_{\text{CM}} = -1.3 \text{ V}$. $\lambda_{\text{exc}} = 795 \text{ nm}$. Generated by img/py/experiment/pl.py.	28
4.5	Sample: DOPED M1_05_49-2. $V_{\text{B}} = 0 \text{ V}$. Generated by img/py/experiment/pl.py.	30
4.6	Sample: FIG F10. $\lambda_{\text{exc}} = 795 \text{ nm}$. $V_{\text{y}} = 30 \text{ V}$ Generated by img/py/experiment/pl.py.	31
4.7	Sample: DOPED M1_05_49-2. $V_{\text{DM}} = -0.43 \text{ V}$. $V_{\text{CM}} = -3.75 \text{ V}$. $V_{\text{y}} = V_{\text{z}} = 30 \text{ V}$. $P = 1 \mu\text{W}$. $\lambda_{\text{exc}} = 795 \text{ nm}$. Generated by img/py/experiment/pl.py.	32
4.8	Sample: DOPED M1_05_49-2. $V_{\text{CM}} = -1.3 \text{ V}$. $P = 1 \mu\text{W}$. Generated by img/py/experiment/pl.py.	34
4.9	Generated by img/py/experiment/tmm.py.	40
4.10	Generated by img/py/experiment/tmm.py.	40
4.11	Generated by img/py/experiment/tmm.py.	41
A.1	Generated by img/py/experiment/tmm.py.	48
B.1	Sample: DOPED M1_05_49-2. $V_{\text{CM}} = -1.3 \text{ V}$. $P = 1 \mu\text{W}$. Generated by img/py/experiment/pl.py.	49
B.2	Sample: DOPED M1_05_49-2. $\lambda_{\text{exc}} = 795 \text{ nm}$. Generated by img/py/experiment/pl.py.	50

Part I

**A FLEXIBLE PYTHON TOOL FOR
FOURIER-TRANSFORM NOISE
SPECTROSCOPY**

Part II

CHARACTERIZATION AND IMPROVEMENTS OF A MILLIKELVIN CONFOCAL MICROSCOPE

Part III

**OPTICAL MEASUREMENTS OF
ELECTROSTATIC EXCITON TRAPS IN
SEMICONDUCTOR MEMBRANES**

JUST as quantum computers are conceived as the quantum analogon of classical computers with bits and logic operations switched out by quantum counterparts, so can one devise *networks* of such objects, where quantum information generated or processed at a quantum *node* is distributed across long distances through the quantum counterparts of classical information channels [1, 2]. Famously envisioned by Kimble [3], the concept can be extended to the idea of a *quantum internet*. A wide array of ideas has been put forth that make use of the theoretical capabilities of such quantum networks.

Initially, quantum networks were studied in the context of quantum cryptography [4–7]. There, the no-cloning theorem and clever use of entanglement ensure quantum-secured communication between distant parties that cannot be eavesdropped upon or tampered with by adversarial parties without detection.¹ Considerable attention has also been paid to the notion of distributed quantum computation [10]. As quantum computers do not appear to be on the same course of miniaturization as classical computers have been, there might turn out to be a limit to the physical size of quantum computers and, hence, a limit to the processing power of a monolithic node. Distributed quantum computation resolves this bottleneck by allowing computations to be executed across separate nodes much like classical supercomputer clusters. Although a comprehensive resource assessment of the feasibility of such approaches is still outstanding, initial results are promising [11], and experimental demonstrations of small computations have recently been shown [12]. A concept combining distributed quantum computation with quantum cryptography is blind quantum computation [13, 14], which promises a form of cloud-based quantum computation. Also here first experimental demonstrations have been achieved [15].

Next, quantum networks have garnered interest in the field of quantum sensing [16]. This term refers to the branch of quantum technology in which individual quantum systems are employed as highly sensitive sensors, for example of magnetic fields, or, more generally, to perform measurements of physical quantities [17, 18]. For example, there exist proposals to employ quantum networks for long-baseline telescopes that use optical interferometry to enhance the resolution of astronomical imaging [19, 20], akin to the techniques used to produce the first image of a supermassive black hole [21], or global networks of quantum clocks [22]. Going beyond technological applications, the capability to coherently transmit quantum states across large distances opens the pathway to tests of quantum theory itself, and where it might fail [23].² At least since the publication of the Einstein-Podolsky-Rosen (EPR)–paradox [24], tests of the non-locality of quantum mechanics have been proposed [25, 26] and performed [27, 28]. More recently, for example, a small quantum network was used to rule out a description of quantum theory by real numbers [29] and we may expect more such experiments to come [30]. Indeed, as the first small-scale experimental demonstrators arrive [31–34], research into complex quantum networks and their properties and possible applications is still in its beginnings [35].

So how does such a quantum network work? In the “canonical quantization” picture we already adopted previously, we might simply replace

1: As ever in cryptography, new protocols keep getting hacked and loop-holes are discovered [8, 9]. It will be interesting to see, therefore, if the security will faithfully transfer from theory to experiment.

2: This area of physics is termed *foundations of physics*.

classical, optical links by quantum versions thereof and similarly transmit *flying* qubits instead of bits through those channels. However, even optical fibers, the backbone of the modern internet, are lossy, and since the photon loss scales exponentially with distance, there would be little hope to build networks larger than a few to a few tens of kilometers.³ In classical networks, this problem is remedied by repeater stations that simply produce copies of incoming photons and thus amplify the signal. In quantum mechanics, however, this is forbidden by the no-cloning theorem, which states that one cannot achieve a perfect copy of a qubit prepared in an arbitrary and unknown quantum state [37, 38]. To the rescue comes, then, entanglement. By letting two adjacent repeater stations share a bipartite maximally entangled state (often referred to as a EPR or Bell pair), a station, Charlie, positioned between two others, Alice and Bob, each of whom Charlie shares Bell pairs with can perform a Bell measurement on the two halves of the pairs in his possession and thereby project Alice and Bob's halves into a state that is maximally entangled between the two of them. This technique of entangling two states that have never interacted with each other is known as entanglement swapping [39, 40]. Briegel et al. [41] and Dür et al. [42] then proposed a quantum repeater protocol that uses entanglement swapping, enhanced by entanglement distillation,⁴ to successively entangle neighboring pairs of entangled states whose resource requirements scale logarithmically with the length of the quantum channel between the ends of which entanglement needs to be established. What is more, the protocol tolerates error and loss rates on the percent level and is thus much more benign than quantum error correction (QEC). Following the initial proposal, more improved schemes were developed that tolerate higher errors [43] or employ entirely different techniques [44], see Reference 36 for a review, and recently also experimental realizations have been shown [45].

A crucial detail of the protocol is that it requires storing Bell states until the heralding of successful entanglement in a quantum memory.⁵ In practice, this means that quantum repeaters require a coherent light-matter interface between photonic flying qubits and stationary quantum memory since storing photons is not feasible. Such an interface has been the subject of intense research and there exist a large number of competing approaches that differ in choice of material platform for the memory and choice of encoding for the photon [47, 48]. Among the most advanced are atomic and defect-based systems. Atomic (and ionic) systems are a natural choice as the energy scales of atomic transitions are compatible with photons in the telecom range (~ 1550 nm) [32, 33, 45, 49, 50]. Nuclear spins coupled to defects in crystal lattices have long spin lifetimes at the same time as optical transitions [31, 34, 51–53]. Optically interfacing semiconductor spin qubits⁶ or superconducting qubits, on the other hand, is arguably more challenging because of a separation of energy scales. While qubits in these systems have energy splittings in the GHz regime, telecom photons have energies of hundreds of THz, and so bridging this gap requires some sort of intermediary or *transducer*. For superconducting qubits, approaches based on mechanical resonators [54] and electro-optic nonlinear materials [55] have been pursued among others. For spin qubits, excitons (or complexes thereof) confined in optically active quantum dots (OAQDs) such as self-assembled QDs [56–59] appear to be most promising owing to their excellent optical properties. Due to the fast recombination speeds of excitons, their suitability as a qubit is limited. Single charge carriers confined to self-assembled quantum dots (SAQDs) have been explored instead [60], but still face the problem that the growth of SAQDs is random and as such coupling two or more qubits is extremely challenging. By contrast, spin

3: We can expect a survival probability of 1 % over a distance of 100 km [36]. There is therefore arguably no feasible alternative to optical transmission over long distances.

4: Also known as entanglement purification.



5: I note that there exist also protocols for memoryless, all-optical quantum repeaters [36, 46].

6: By semiconductor spin qubits, I refer to qubits encoded in the spin of one or more electrons or holes confined in quantum dots (QDs), in contrast to spins attached to charged defect centers or nuclear spins.

qubits confined in gate-defined quantum dots (GDQDs) have reached a high level of maturity [61, 62], and the promise of scalability by leveraging the highly advanced industrial semiconductor fabrication technology still holds true.

Jöcker et al. [63] thus proposed a protocol for transferring the quantum state of a photonic, polarization-encoded qubit to that of a spin qubit confined in a GDQD by means of a OAQD serving as intermediary in order to benefit from the benign optical properties of the latter and the long coherence times and processing capabilities of the former. In the protocol, an incident photon generates an exciton in the OAQD, transferring the quantum state to the exciton. By application of a strong in-plane magnetic field, bright and dark states of the exciton are mixed and electron and hole remain in a product state with all information encoded in the electron spin. This allows discarding the hole and subsequently transferring the electron state to the GDQD, the details of which depend on the encoding chosen, either single-spin (Loss-DiVincenzo (LD)) or two-spin (singlet-triplet (ST)) qubit. The protocol is agnostic to the precise realization of the OAQD, although it adopts parameters from SAQDs. A crucial ingredient of the protocol is that the OAQD be in tunnel-coupling distance to the GDQD in order to enable exchange coupling or the adiabatic transfer of the photo-electron. For SAQDs this is a challenging endeavor since, as mentioned above, their growth is random and therefore requires one to first locate the dots and then align the gates during fabrication of the GDQD. Because of the exponential dependence of tunnel coupling on the distance, this alignment needs to be very precise indeed.

An alternative to an SAQD was proposed by Descamps [64] in form of an electrostatic exciton trap. Here, excitons are designed to be confined not by local modifications of the band structure during growth but by application of out-of-plane electric fields through gate electrodes. This tilts the band structure and lowers the exciton energy by the quantum-confined Stark effect (QCSE), where exciton dissociation is prevented by charge carrier confinement in a quantum well (QW). To avoid dissociation by lateral electric fields, Descamps [64] developed a fabrication process to thin down the semiconductor heterostructure to a thin membrane symmetric about the QW, allowing lithographic patterning of laterally aligned, nanometer-scale gate electrodes on both sides of the membrane [65]. Application of voltages of the same magnitude but opposite polarity to gates on the top and bottom side of the membrane then produces – to leading order – a local electric field without changing the chemical potential in the QW itself, while voltages of the same polarity have just the opposite effect. Together with the out-of-plane confinement by the QW, this should in theory provide 0D-confinement of exciton purely by electrostatic means and allow for the top-down, scalable fabrication of OAQDs in close proximity to other, conventional GDQDs. What is more, the confinement strength and potential relative to the neighboring GDQD can be finely tuned by well-established techniques.

In Reference 65, Descamps et al. demonstrated the implementation of the membrane fabrication process as well as initial progress towards forming a GDQD in transport and optical measurement of the lowering of the local exciton potential by the QCSE. Yet unobserved was the signature of QD-behavior in an exciton trap as manifested by, for example, the resolution of orbital splittings or single-photon emission. In this part of the present thesis, I present optical measurements of exciton traps towards this goal. It is outlined as follows. In Chapter 2, I give an introduction to the physics of photoluminescence (PL) in semiconductors as well as the influence of electric fields. Following that, I introduce the Python

measurement framework I wrote to control the experiment in Chapter 3. Then, in Chapter 4, I present measurements of doped membranes. I show data of an exciton trap and discuss the voltage, power, and position dependence of the PL emission as well as photoluminescence excitation (PLE) measurements. Finally, I perform simulations of the membrane structure to explain the quenching of PL intensity observed when focusing a gate and propose slight modifications to the heterostructure design to mitigate this effect. I conclude with an outlook in Chapter 5.

Photoluminescence and excitons in semiconductors

2

SEMICONDUCTORS form the basis of the modern age of technology. In large parts, this is due to their favorable optical properties, determined chiefly by their band gap on the order of 1 eV, that enable wide-ranging applications from semiconductor lasers over photo-detectors to optical communication technology. Semiconductors can be classified into *direct* and *indirect* categories, where the terminology refers to the location of the band gap, that is, the smallest energy difference between valence and conduction band in the Brillouin zone. A direct semiconductor's band gap features a valence band maximum at the same point in k -space as a conduction band minimum. Such materials, a prime example of which is the compound GaAs with a band gap of $E_g = 1.519$ eV at $T = 0$ K in the near-infrared (NIR) spectrum [66], emit electromagnetic radiation with energy $h\nu = E_g$ when electrons are excited from the valence into the conduction band. When the excitation occurs through optical absorption, this effect is known as photoluminescence.

Of course, besides their optical applications, semiconductors are also the backbone of the modern electronics industry. Their band gap allows tuning the conductivity by means of the field effect wherein the potential and thereby the band structure is locally modified by means of a voltage applied to a gate electrode. This facilitates the construction of voltage-controlled transistors. The development of remote-doping techniques then enabled the growth of extremely high-mobility two-dimensional electron gases (2DEGs) in GaAs/Al_xGa_{1-x}As heterostructures [67]. In these structures, dopants are introduced into the AlGaAs barrier layer some 50 nm away from the GaAs layer and thus spatially separated by a AlGaAs spacer layer. This reduces Coulomb scattering in the 2DEG induced by the doping and produces very high-quality samples as evidenced for example by the observation of the fractional quantum Hall effect [68]. It is hence not at all surprising that early quantum dot experiments also took place in this well-understood material system. While undoped approaches to electron and hole spin qubits in GaAs exist [69–72], they introduce added complications because of the need to electrostatically induce a 2DEG and reliably contacting it [73]. What is more, these issues are exacerbated when the structures need to be thinned down to a membrane [64, 74]. Therefore, to accommodate GDQDs next to the OAQD in the membrane, the devices measured in this part of the present thesis are fabricated on doped heterostructures hosting a 2DEG. In the following, I discuss the optical behavior of these structures under illumination.¹

2.1 Photoluminescence in doped GaAs/Al_xGa_{1-x}As heterostructures

Consider an intrinsic, direct-gap, Zincblende semiconductor such as GaAs with a band gap of $E_g = 1.519$ eV at zero temperature [66]. At the Γ -point, the conduction band is well approximated by a parabolic band with effective mass $m_c^*/m_e = 0.067$ and is offset by $E_g/2$ above the Fermi level μ . Offset by the same absolute amount in the opposite direction is the valence band, which close to Γ is fourfold degenerate with heavy and light

1: The *electrical* behavior is another matter; there, illumination can lead to the creation, trapping, and de-trapping of free charge carriers that alter the transport properties of the device, leading to electrical hysteresis and instability [74–78].

holes with effective masses $m_{\text{hh}}^*/m_e = 0.34$ and $m_{\text{lh}}^*/m_e = 0.09$, respectively [79]. The third valence band² is split off by the spin-orbit interaction and lies 0.34 eV below the other valence bands [80]. Introducing confinement in one direction, for example by doping a GaAs/Al_xGa_{1-x}As heterojunction or growing a GaAs QW sandwiched between two layers of AlGaAs, lifts the fourfold degeneracy of light and heavy holes and leaves – under usual conditions – the latter as the valence band ground state.

Doping in sufficiently high concentration then raises the Fermi level from mid-gap to inside the conduction band in the plane of confinement, resulting in a band structure as sketched in Figure 2.1. The bands remain parabolic as function of the in-plane wave vector k_{\parallel} close to Γ . The conduction band is filled up to μ where, measured from the conduction band edge, $E_c(k_{\parallel} = k_F) = E_F = \hbar^2 k_F^2 / 2m_c^*$ with the Fermi wave vector $k_F \sim 10^8 \text{ m}^{-1}$. Now, absorption of a photon incident on the semiconductor demands conservation of energy and momentum. The latter condition implies that hole and electron have close to equal momentum because $k_y = 2\pi/\lambda \approx 8 \times 10^6 \text{ m}^{-1}$ is much smaller than k_F . Thus, excitation of an electron-hole pair from the valence into the conduction band occurs only for $k \geq k_F$. By contrast, recombination can take place for any k in principle. In practice, however, photo-electrons quickly relax down to the Fermi level, and recombination takes place between electrons inside the Fermi sea and photo-holes somewhere in the valence band at $k \leq k_F$.³ The former condition then implies $E_{\gamma} \geq E_g + E_F (1 + m_c^*/m_{\text{hh}}^*)$ because no free electron states are available in the conduction band below μ due to the Pauli exclusion principle and where the term in parentheses is due to the valence band dispersion. Many-body effects due to localized photo-holes scattering with electrons of the Fermi sea can lead to a strong enhancement of luminescence intensity at the Fermi edge, the so-called Fermi-edge singularity (FES) [82–84]. The intensity of the PL at the Fermi edge relative to recombination at the band edge ($k_{\parallel} = 0$) is thus an indicator of the QW interface quality and degree of alloy fluctuations, both of which lead to hole localization [85, 86].

Free electron-hole pairs created by photo-excitation can form hydrogenic bound states due to the Coulomb attraction of their opposite electric charges, *excitons*. In two dimensions, this effect is strongly enhanced due to the increased overlap of electron and hole wave functions. Furthermore, the reduced dimensionality also enhances the binding energy from $\sim 4 \text{ meV}$ in bulk GaAs to up to four times that in GaAs QWs [87, 88]. Rather than the continuum of the joint density of states of valence and conduction band discussed previously, excitons are discrete states whose energy is lower than the band gap energy by the binding energy, $E_X = E_g - E_b$. In doped QWs hosting a 2DEG, the free carriers can screen the exciton binding energy and lead to an ionized electron-hole plasma [89]. This is known as the insulator-to-metal (Mott) transition in semiconductors [90]. Competing with this are so-called Mahan excitons [82, 83] that give rise to the FES [91].

Next, I discuss the influence of an electric field on excitons. For this, we return to undoped structures for simplicity.

2: The valence bands are *p*-like and hence contain contributions from three twofold degenerate atomic orbitals.

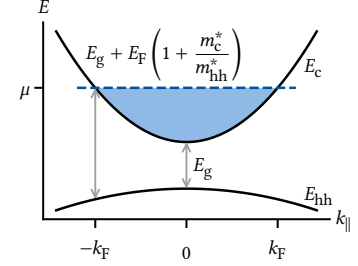


Figure 2.1: Band structure diagram of a doped heterostructure (after Reference 81). Due to the *n*-type doping, the conduction band is filled up to the Fermi level μ . Photonic excitation of an electron-hole pair can only occur at $|k| > k_F$ into the free states above μ due to the small photon momentum. Recombination can occur within a bandwidth of $E_F(1 + m_c^*/m_{\text{hh}}^*)$.

3: For sufficiently localized states in real space, a wide range of k states in the valence band is available for recombination as states are extended in k -space. We can estimate the localization length required for states up to k_F to participate by $\Delta x \geq 1/2\Delta k = 1/2k_F \sim 5 \text{ nm}$ for a typical 2DEG.

2.2 The quantum-confined Stark effect

Consider the electron-hole pair in bulk GaAs in the co-moving frame of the hole. The hole generates the Coulomb potential

$$V(r) = \frac{e}{4\pi\epsilon_0\epsilon_r|r|}, \quad (2.1)$$

where $\epsilon_r = 13.3$ is the relative permittivity of GaAs at low temperatures, which attracts the electron by the Coulomb energy $E(r) = qV(r) = -eV(r)$. Figure 2.2 depicts the Coulomb potential in magenta and the bound electron's wave function sketched in black. The electron-hole separation r is shown in units of the exciton Bohr radius in two dimensions [92]

$$a_B = \frac{2\pi\epsilon_0\epsilon_r\hbar^2}{\mu e^2} = 6 \text{ nm} \quad (2.2)$$

with μ the reduced effective mass of conduction and heavy-hole valence bands.

We now apply an electric field F . This modifies the potential seen by the electron by erF as sketched in green Figure 2.2. Ignoring changes to the electron wave function, we can see that the electron can tunnel out of the Coulomb potential, leading to *field-induced ionization* of the exciton. Now place the exciton in a QW instead of in bulk with the electric field pointed such that it is out-of-plane of the QW. The field still tilts the potential, but because electrons and holes are confined into a quasi-two-dimensional plane, they cannot escape and hence do not dissociate. This is the QCSE [93].

In order to obtain a qualitative understanding of the QCSE, consider an undoped GaAs/Al_{0.33}Ga_{0.66}As QW of width $L = 20 \text{ nm}$. We take a 57:43 ratio for the band offsets [79], resulting in discontinuities of height $\Delta E_c = 0.24 \text{ eV}$ and $\Delta E_{hh} = 0.18 \text{ eV}$ at the interfaces for the conduction and the heavy-hole valence band, respectively, and $m_c^*/m_e = 0.067$ and $m_{hh}^*/m_e = 0.34$ for the effective masses.⁴ Assuming an infinitely deep well for simplicity, the eigenenergies are

$$E_n = \frac{1}{2m^*} \left[\frac{\pi\hbar n}{L} \right]^2 \quad (2.3)$$

and the eigenstates are

$$\psi_n(z) = \sqrt{\frac{2}{L}} \sin\left(\frac{n\pi z}{L}\right). \quad (2.4)$$

The ground state energy is then 14 meV (3 meV) above (below) the conduction (valence) band edge, corresponding to 6 % (2 %) of the respective band offsets and implying that the infinite-well approximation is acceptable,⁵ while the first excited state lies 42 meV higher than the ground state. The upper panel of Figure 2.3 depicts the first two wave functions of electrons and holes in a band structure diagram. Due to the symmetry of the confining potential, the wave functions are symmetric around the center of the well.

Now, applying an out-of-plane electric field tilts the bands and pulls electrons and holes to opposite interfaces of the QW. The Hamiltonian for

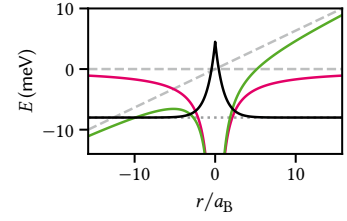


Figure 2.2: Effect of an in-plane electric field on an exciton wave function. In the hole's reference frame, the electron sees a static attractive Coulomb potential (magenta), resulting in a bound state (dotted gray line, wave function sketched in black). Applying an electric field ($F = 100 \text{ mV}/\mu\text{m}$, dashed gray lines) tilts the Coulomb potential (green) and leads to a transparent barrier through which the electron can tunnel out.

4: I note that the literature knows many different values for the hole effective mass in the plane of a quantum well, suggesting that one should actually measure it to be confident in the actual value.

5: In a finite well, the wave functions decay exponentially into the barriers and result in slightly lower eigenenergies. However, the qualitative behavior remains the same.

the electrons in this case reads [80, 94, 95]

$$H = -\frac{\hbar^2}{2m^*} \frac{d^2}{dz^2} + eFz \quad (2.5)$$

if we take z to be zero at an interface and choose $F \geq 0$. Introducing the length and energy scales [80]

$$\tilde{\epsilon} = \left[\frac{(\hbar e F)^2}{2m^*} \right]^{\frac{1}{3}}, \quad (2.6)$$

$$\tilde{z} = \left[\frac{\hbar^2}{2m^* e F} \right]^{\frac{1}{3}} = \frac{\tilde{\epsilon}}{eF}, \quad (2.7)$$

and defining

$$Z_n(z) = z/\tilde{z} - \epsilon_n/\tilde{\epsilon} \quad (2.8)$$

with ϵ_n the eigenvalues of H , the Schrödinger equation becomes [94]

$$\frac{d^2}{dZ_n^2} \psi_n(Z_n) = Z_n \psi_n(Z_n). \quad (2.9)$$

Equation 2.9 is known as the Stokes or Airy equation and has the general solution

$$\psi_n(Z_n) = \alpha_n \text{Ai}(Z_n) + \beta_n \text{Bi}(Z_n), \quad (2.10)$$

where $\text{Ai}(z)$ and $\text{Bi}(z)$ are the Airy functions. $\text{Ai}(z)$ and $\text{Bi}(z)$ oscillate for $z < 0$ and decay (grow) exponentially for $z > 0$, respectively. As we assumed infinitely high barriers at $z = 0$ and $z = L$, the boundary conditions impose

$$\psi_n(Z_n(0)) = \psi_n(Z_n(L)) = 0, \quad (2.11)$$

which completely determines the eigenstates and -energies. For large well widths or fields ($eFL/\epsilon_n \gg 1$), the second term is exponentially suppressed and the eigenenergies are given by the zeros of $\text{Ai}(Z_n)$. For zero field, one recovers the square well solution (Equations 2.3 and 2.4).

The finite-field case is shown in the lower panel of Figure 2.3 for $F = 5 \text{ V}/\mu\text{m}$. Due to the larger effective mass of the heavy holes, the characteristic length scale \tilde{z} is shorter and hence the corresponding wave functions are narrower than their electronic counterparts. The ground state transition energy at this field is 10 meV below the gap or 27 meV lower than in the zero-field case.

For a full quantitative accounting of the transition energies, the exciton binding energy as well as finite barrier heights would need to be included. The former is on the order of 6 meV to 9 meV in GaAs and becomes smaller as the overlap of the electron and hole wave functions is reduced when applying an electric field, pulling the wave functions to opposite interfaces [93]. Miller et al. [95] found that finite-well properties could be reproduced by using effective well widths with infinite-well models. The latter should have a small effect on the ground state energy as argued above.

2.2.1 In-plane confinement

So far, we have considered the QCSE in a single dimension, as if we were to apply a global electric field. However, as we saw before, the field lowers the exciton energy below the QW confinement and hence, if applied locally, results in an effective confinement potential in the plane of the

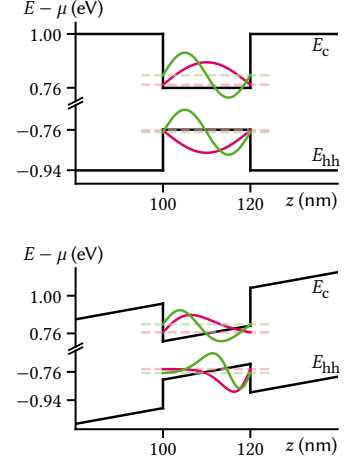


Figure 2.3: QCSE in an undoped QW. Top: conduction and heavy-hole valence band profiles along the growth direction. The wave functions of the first two eigenstates in the well are drawn in magenta and green, respectively. The ground state transition is larger by $\Delta E = 17 \text{ meV}$ than the gap E_g due to the confinement. Bottom: same structure as above with an out-of-plane electric field applied across the structure ($F = 5 \text{ V}/\mu\text{m}$). Analytical wave functions in the infinite-well approximation are shown in magenta and green again. The wave functions get pushed to opposite interfaces of the QW, lowering the ground state transition energy by $\Delta E = -10 \text{ meV}$. Excitonic effects are not included.

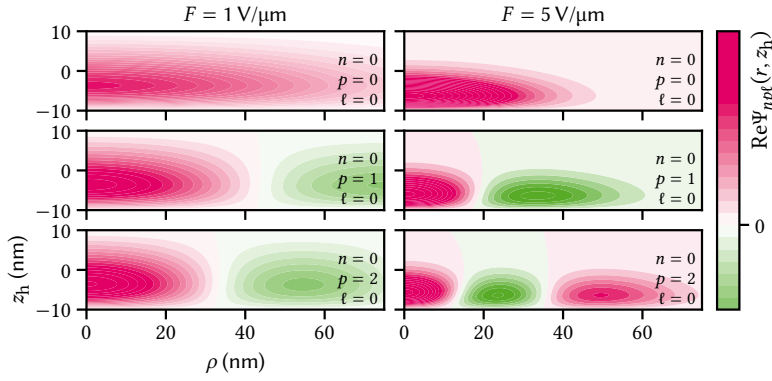


Figure 2.4: Center-of-mass exciton wave function (hole sector) in a harmonic trap under an electric field. Left column shows the low-field and right column the high-field case. Top row is the ground state, middle and bottom row the first and second excited state in the plane, respectively. The out-of-plane wave function is the ground state in all cases ($n = 0$) and the trap confinement strength $\omega/2\pi = 738$ GHz for $F = 5$ V/ μm [64, Section 2.2.2] and linearly interpolated for 1 V/ μm (see text).

QW. Descamps [64] performed numerical simulations for a geometry with circular gate electrodes with 200 nm diameter on both sides of a membrane, finding a confinement depth of $V_0 = 20$ meV at $F = 5$ V/ μm that is well approximated by a single-particle harmonic potential for the center-of-mass wave function of the exciton, $V(\rho) = M\omega^2\rho^2/2 - V_0$, with mass $M = m_c^* + m_{hh}^*$ and confinement strength $\omega/2\pi = 738$ GHz corresponding to an oscillator length $\xi = \sqrt{\hbar/M\omega} = 20$ nm. To obtain a qualitative picture, let us interpolate this result for different fields. The depth of confinement corresponds to the energy shift induced by the QCSE and is quadratic in F , $V_0 = -\alpha F^2$. At vanishing field, there should be no in-plane potential, $\omega = 0$. Hence, we can assume that $\omega \propto F$ to leading order and thus $V(\rho) = \beta M F^2 \rho^2/2 - \alpha F^2$.

How does this in-plane confinement modify the wave function? We ignore the relative motion of electron and hole as the optical properties of the exciton are dominated by the behavior at zero separation for $a_B/\xi < 1$ [96], and consider only $\Delta n = 0$ transitions, *i.e.*, electron and hole in the same z quantum state, as $\Delta n \neq 0$ transitions are much weaker [80]. Let us further initially assume a separable wave function and choose cylindrical coordinates according to the symmetry of the potential. We then have

$$\Psi_{npl}(z_e, z_h, \rho, \phi) = \psi_n(z_e)\psi_n(z_h)\chi_{pl}(\rho)\exp(i\ell\phi) \quad (2.12)$$

where⁶ [97]

$$\chi_{pl}(\rho, \phi) = \sqrt{\frac{2p!}{2\pi\xi^2(p+|\ell|)!}} \exp(-\tilde{\rho}^2/2) \tilde{\rho}^{|\ell|} L_p^{|\ell|}(\tilde{\rho}) \quad (2.13)$$

with the associated Laguerre polynomial $L_p^{|\ell|}(x)$ and we used the shorthand $\tilde{\rho} = \rho/\xi$. The numbers $p \in \mathbb{N}$ and $\ell \in \mathbb{Z}$ denote the principal and orbital momentum quantum numbers. The eigenenergies of the harmonic oscillator solution, Equation 2.13, are given by

$$\epsilon_{pl} = \hbar\omega(2p + |\ell| + 1). \quad (2.14)$$

To account for a finite well width ($L \approx \xi$ in our case), we can to a first approximation perform the replacement $\rho \rightarrow r = \sqrt{\rho^2 + z^2}$ in Equation 2.12. The resulting wave function $\Psi_{npl}(r, z_h)$ at fixed electron coordinate z_e is shown in Figure 2.4 for $n = \ell = 0$ (which makes it independent of ϕ). For $\ell = 0$ Ψ_{npl} has n nodes along z and p nodes along ρ .

At last, we can use the exciton wave function $\Psi_{nml}(r, \phi, z_e, z_h)$ to esti-



6: Note that Karimi et al. miss a factor 2π in the normalization.



mate the *oscillator strength*, a quantity often quoted in semiconductor spectroscopy. The oscillator strength puts in relation the quantum mechanical transition rate with the emission rate of a classical oscillator with frequency $\omega = \Delta E/\hbar$ matching the transition energy [98]. For a dipole transition from state $|i\rangle$ to state $|j\rangle$, it may be written as [80]

$$f_{ji} = \frac{2\mu\Delta E_{ji}}{\hbar^2} |\langle j|\mathbf{r}|i\rangle|^2, \quad (2.15)$$

where μ is the reduced mass of the exciton. As the selection rules only allow in-plane dipole transitions for heavy holes, we write [96]

$$f_{npl} = \frac{2\mu\epsilon_{npl}}{\hbar^2} J_r^2 J_\phi^2 |\langle u_c|x|u_{hh}\rangle|^2 \quad (2.16)$$

for transitions with $\Delta n = \Delta p = \Delta \ell = 0$, where

$$J_r = \int_0^L dz \int_0^\infty d\rho \rho \psi_n^{(e)}(z) \psi_n^{(h)}(z) \chi_{pl}(\sqrt{\rho^2 + z^2}), \quad (2.16a)$$

$$J_\phi = \int_0^{2\pi} d\phi \exp(i\ell\phi), \quad (2.16b)$$

$$\epsilon_{npl} = \epsilon_n + \epsilon_{pl}, \quad (2.16c)$$

and $|u_{c(hh)}\rangle$ are the Bloch functions of the valence and conduction band, respectively, that we have neglected so far. From Equation 2.16b, we immediately see that the oscillator strength of states with nonzero orbital momentum ($\ell \neq 0$) vanishes, $f_{np0} = 0$! This in turn implies from Equation 2.14 that the exciton level spacing in a radially symmetric trap is given by $\Delta E = 2\hbar\omega = 1$ meV, a factor of two larger than assumed by Descamps [64].

As we tilt the bands, energy levels below the QW become available in the barrier once $\Delta E_{c(hh)} - \epsilon_n \sim eFd$ with d the width of the barrier. This allows confined carriers to escape the QW with a finite probability by tunneling through the barrier, an effect known as Fowler-Nordheim tunneling. Following Reference 80, we can estimate the tunneling probability as⁷

$$\mathcal{T}_n(F) \approx \exp \left\{ -\frac{\sqrt{4m^*[\Delta E_{c(hh)} - \epsilon_n]^3}}{eF\hbar} \right\}. \quad (2.17)$$

7: The same result up to a slightly different numerical prefactor in the exponent is obtained more formally from the WKB approximation [64].

The tunneling rate Γ_n can then be estimated by the frequency that a confined charge carrier “visits” the edge of the QW multiplied by the probability that it tunnels, \mathcal{T}_n [99]. That is, we take ϵ_n to be a kinetic energy and calculate the velocity as

$$v_n = \frac{\hbar k_n}{m_{c(hh)}^*} = \sqrt{\frac{2\epsilon_n}{m_{c(hh)}^*}}. \quad (2.18)$$

Then the frequency of one round trip inside the QW is

$$\tau_n^{-1} = \frac{v_n}{2L} = \frac{1}{L} \sqrt{\frac{\epsilon_n}{2m_{c(hh)}^*}} \quad (2.19)$$

and

$$\Gamma_n = \frac{\mathcal{T}_n}{\tau_n}. \quad (2.20)$$

What is the order of magnitude of τ_n ? For an energy of $\epsilon_n = 10$ meV,

$\tau_n \approx 200$ fs for electrons and 400 fs for holes. The tunneling probability \mathcal{T}_n therefore needs to be quite small indeed for the rate Γ_n to remain small.

Figure 2.5 summarizes the QCSE in a QW additionally confined in the plane by local electric fields. The top panel shows the exciton transition energy ΔE_{np} for $\Delta n = \Delta p = 0$ in solid lines.⁸ The first three in-plane sublevels due to the harmonic potential are drawn in less saturated colors but hard to see because the level spacing is much smaller than the out-of-plane QW subband spacing, ~ 1 meV/50 meV. The ground state shows the expected quadratic dependence on the electric field also obtained, for example, from perturbation theory. Drawn as a dashed line is the induced dipole moment,

$$\mathbf{p}_{np}(F) = \frac{\partial \Delta E_{np}}{\partial F} \hat{\mathbf{e}}_z, \quad (2.21)$$

which is monotonously decreasing for the ground state as function of electric field F , consistent with a continuous lowering of energy. For the first excited state, the induced dipole moment is actually positive below 2 V/ μm , leading to a repulsive interaction and hence a raising of the transition energy by up to 1 meV. The lower panel shows the oscillator strength, Equation 2.16, normalized to its value of the ground state at zero field, $f_{00}(F = 0)$. For the ground state it decays exponentially with the electric field as the overlap between electron and hole wave functions, which decay exponentially into the QW themselves, is reduced. f_{0p} for higher in-plane orbital states ($p > 0$, magenta, decreasing saturation) has an envelope following the ground state's exponential decay but vanishes at p points in F due to the fact that the wave function has p nodes. By contrast, f_{10} for the first excited QW state (green) does not decay to zero at large fields but also has a zero at an intermediate field because of the wave function's node along z .

Finally, the right axis shows the estimated tunneling rates (Equation 2.20) of the electron (hole) ground (excited) states in dashed (dash-dotted) magenta (green) lines, respectively. Rates of electrons are at least four orders of magnitude larger than those of holes owing to their smaller effective mass despite the larger band offset. At $F = 5$ V/ μm corresponding to a voltage of 1 V across a membrane of 200 nm thickness, the electron tunnel rate is on the order of 1 Hz, but rises very quickly above that. Considering once again a QW hosting a 2DEG and neglecting associated band bending effects, this rate corresponds to a current through a circular area of 1 μm in diameter of 600 aA at an electron density of $n = 5 \times 10^{11} \text{ cm}^{-2}$, but already 600 pA at 7.5 V/ μm .

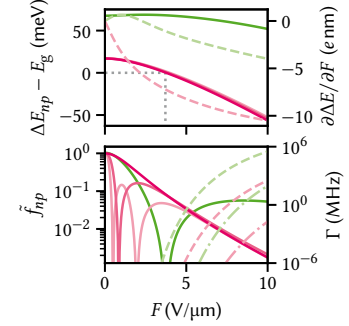


Figure 2.5: Electric field dependence of the QCSE for the first two energy levels in the QW. Top: the ground state energy (magenta) shows the expected quadratic dependence; the confinement energy is compensated at around $F = 3.7$ V/ μm . Higher in-plane orbital levels are shown for the QW ground state in decreasing saturation. For zero field, the splitting is zero as there is no in-plane confinement. At maximum field, the splitting is $2\hbar\omega = 2$ meV. Dashed lines (right axis) show the derivative, revealing that the QW excited state is actually raised in energy at low fields. Bottom: oscillator strengths (same color code as above). Dashed lines (right axis) show the electron tunneling rate through the barrier, dash-dotted the holes.

8: Note again that we neglected the exciton binding energy, which decreases with increasing field and hence slightly reduces the redshift [93].

2.3 Excitonic complexes

If we liken the exciton to a Hydrogen atom⁹ with modified binding energy E_b and Bohr radius a_B , it is natural to expect molecules and ions of these states to exist. The simplest molecule, or excitonic complex, is the biexciton, the analog of the H_2 molecule. Following a similar argument as for the binding energy of the exciton, we expect that of the biexciton to also increase as the dimensionality of the system is reduced. Indeed, in QWs it has been measured to be on the order of 1 meV, 3 to 4 times larger than in 3D [100], although also negative binding energies, corresponding to an anti-bonding state, have been reported [101–103]. A

9: Although positronium is a better analogon.

signature of biexcitons is the power dependence of their PL. The steady-state density of electron-hole pairs, which is proportional to the exciton density at low enough powers, is proportional to the irradiance, *i.e.*, the excitation power. Conversely, the probability to form a two-body bound state is proportional to the square of the density of those bodies and we hence expect the power under the PL peak of a biexciton emission to be proportional to the square of the laser power used to excite the sample.

Besides the neutral biexciton, there exist also charged states consisting of three or more bodies. Here, additional electrons or holes bind to an exciton, forming negative or positively charged trions similar to H^- or He^+ ions. Naturally, this process is favored when a large number of surplus charge carriers is present in the sample such as is the case in doped QWs with a 2DEG (or two-dimensional hole gas (2DHG)) [104]. In these structures, the trion binding energy has been found to also be on the order of 1 meV [105, 106].

The mjolnir measurement framework

3

To facilitate the optical experiments in this part of the present thesis, I wrote a software package that controls the measurement workflow and all other interactions with the setup described in Part II, mjolnir¹ [107]. The package is written in Python, is open source, and has a documentation as well as some rudimentary tests.² In this chapter, I lay out the goals and non-goals behind its development and briefly describe the design, features, as well as the typical workflow.

1: https://git-ce.rwth-aachen.de/qutech/lab_software/python-mjolnir

2: Testing code interacting with hardware is notoriously difficult to achieve in an automated manner.

3.1 Rationale

There exist various software solutions for measurement control, ranging from commercial (e.g., Keysight Labber³) over open source (quantify,⁴ labcore⁵) to home-built (elicit,⁶ QuMADA⁷). While most of these frameworks attempt to achieve some degree of universality and not be tailored towards a specific type of experiment or setup, some bias always exists and most are geared towards fully electrical experiments. On the other hand, software for optical experiments naturally exists as well, but it often suffers the same shortcomings coming from a different direction, and there is fairly little on offer for experiments at the interface of quantum optics and transport. An added complication is the availability of drivers. Striving for full automation of the setup, a number of different drivers are required given the complexity of the setup and the mix of electrical, optical, and mechanical instruments (Part II). Thus, QCoDeS forms a good basis for our specific needs due to its large driver coverage. However, the wide array of physical instruments demands some level of abstraction to promote reproducibility and ease-of-use. Furthermore, while QCoDeS provides measurement functionality, their definition involves a large amount of repetitive setup code that needs to be duplicated for each measurement, invites errors, and degrades legibility. The `dond`⁸ functionality abstracts some of this away for multi-dimensional loops but is not flexible enough for our purposes.

3: <https://www.keysight.com/de/de/products/software/application-software/labber-software.html>

4: <https://quantify-os.org/>

5: <https://github.com/toolsforexperiments/labcore>

6: <https://git-ce.rwth-aachen.de/qutech/frameworks/qool-tool>

7: <https://github.com/qutech/qumada>

8: <https://microsoft.github.io/QCoDeS/api/dataset/index.html#qcodes.dataset.dond>

By contrast, the experiments conducted in the present thesis do not place high demands on timing accuracy and measurement speed as typical PL integration times are relatively long. The software thus does not need to prioritize sophisticated triggering and pulsing logic required by qubit experiments. Because the requirements are rather specific, mjolnir is therefore single-minded. It does not aspire to be suitable for applications other than the ones it is designed for. The implementation is extremely biased towards the particular set of instruments in use in the lab and does not attempt to generalize to allow for different instruments to be used. At the same time, it is designed to be modular, and different functionalities should be able to easily be replaced by other solutions.

3.2 Instrument abstraction

Central to the mjolnir package is the abstraction of physical instruments into logical ones, thereby grouping logical functionality provided by different physical devices. Take for instance the tunable continuous-wave (cw) M Squared Solstis laser. It is cooled by a Thermotek T225p chiller

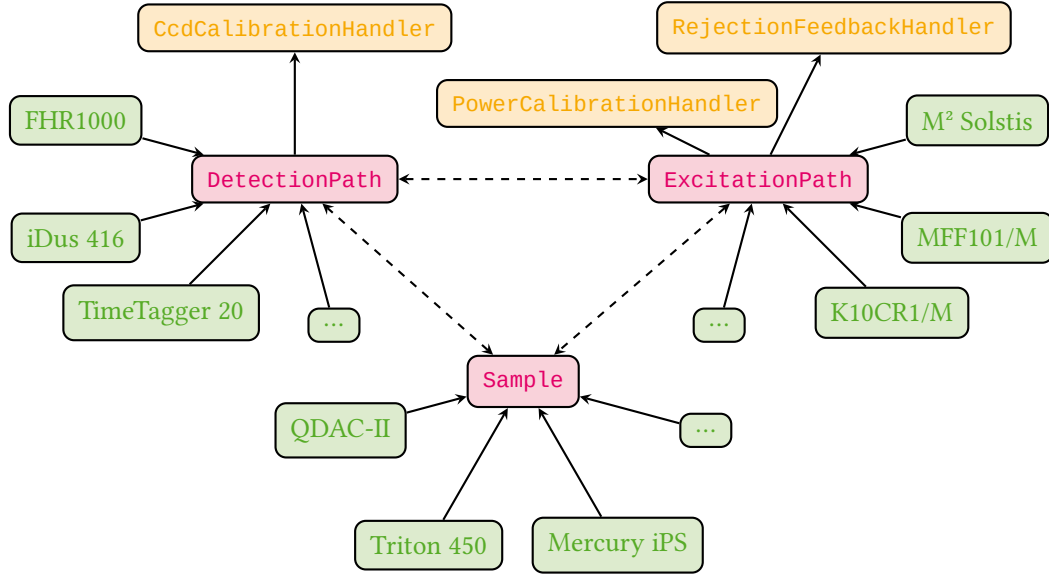


Figure 3.1: Abstraction of physical instruments. mjoInir defines three logical instrument classes (magenta) that represent different aspects of the experiment and group various physical instruments (green). Logical instruments expose various logical parameters that include communication with multiple physical instruments. Sample can be subclassed to suit the particular type of device under investigation. Calibration handlers (orange) are controlled by the logical instruments governing the optical path. Logical instruments are part of a QCoDeS Station and can interact with each other as indicated by the dashed arrows.

and pumped by a Lighthouse Photonics Sprout-G diode-pumped solid state (DPSS) laser. Behind its exit aperture, a Thorlabs MFF101/M acts as a shutter, a neutral-density (ND) filter mounted on a Thorlabs K10CR1/M controls the output power, while a Thorlabs PM100D monitors the power at the optical head and an Attocube AMC100 controls the polarization state of the optical head. Thus, seven different instruments from five different manufacturers are required to control the illumination state of the sample. As a user, however, one would simply like to en- or disable the laser and set wavelength, power, and polarization configuration of the optical head.

To simplify and abstract away the particularities of the physical instruments providing control over parts of a user-facing parameter such as the excitation wavelength,⁹ three logical instruments implemented as subclasses of the QCoDeS Instrument class govern the experimental apparatus:

1. **ExcitationPath**. Controls all physical instruments related to illumination of the sample, including the white light source.
2. **DetectionPath**. Controls instruments related to the detection of radiation emitted by the sample, *i. e.*, the spectrometer, charge-coupled device (CCD), and photon counting card.
3. **Sample**. Controls the QDevil QDAC-II voltage source, cryostat, and magnet, and implements a software representation of the device under test (DUT).

9: For example, the power meter needs to be informed when changing the wavelength to keep the internal calibration up to date.

Figure 3.1 shows a graph outlining the relationship between physical and logical instruments. In the following, I give a brief overview of the functionalities comprised by these logical instruments.

3.2.1 Excitation path

As already outlined above, the `ExcitationPath` object controls everything related to the illumination of the sample. The `active_light_` source parameter switches between laser, white light, and no illumination. Turning on the laser comprises enabling the chiller, switching on the pump laser, waiting for it to ramp up, and asserting the wavelength lock is acquired. For safety reasons, confirmation by the user that they are physically in the lab is required. Furthermore, the `ExcitationPath` instrument implements setting the excitation power by means of a calibration of the ND filter, see Section 3.3. Since the output power of the laser varies depending on wavelength, the object furthermore provides a `wavelength_constant_power` parameter that automatically recalibrates the power once a new wavelength is set. Finally, it manages the state of the automatic excitation rejection control, see Section 3.3.

3.2.2 Detection path

The `DetectionPath` object is responsible for the optical analysis. Chiefly, it manages the Horiba FHR1000 spectrometer and provides convenient shorthands for selecting grating (`active_grating`) and exit port (`active_detection_path`, either `"ccd"` or `"apd"`). It handles initialization of the spectrometer and the CCD including the CCD cooler and oversees calibration of the CCD pixel-to-wavelength relation, see Section 3.3. From the CCD calibration and its pixel size, the dispersion at the imaging plane of the currently selected grating can be obtained, allowing the user to set the monochromator bandwidth of the spectrometer in terms of a wavelength window rather than the more abstract exit slit width.

3.2.3 Sample

The `Sample` class initializes the QDevil QDAC-II digital-to-analog converter (DAC) and magnet power supply. Mainly, though, it serves as an abstraction of the actual DUT and its “control knobs” such as gates. Users implement subclasses for different sample designs. As the samples we are concerned with in the present thesis, I discuss the main implementation, `TrapSample`, representing samples with exciton traps. On a single sample, there are any number of traps consisting of one or both sets of top and bottom “central” and “guard” gates. Each trap is implemented as a QCoDeS `InstrumentModule`, `Trap`, that is part of a `ChannelList`. The currently active trap (*i.e.*, the one currently in focus by the microscope) is selected by the `active_trap` parameter and accessible through the `trap` property of the `TrapSample` object. A `Trap` exposes the virtual gate parameters¹⁰ `difference_mode` and `common_mode` (see Subsection 4.1.1) as the difference and sum of top and bottom gate voltages, respectively, as well as the unmodified top and bottom gate voltage and corresponding leakage current parameters. DAC channels are mapped to their corresponding `Trap` parameters using `yaml` configuration files specific to each sample and hosted in a separate repository.

3.3 Calibrations

`mjolnir` implements three automatic calibration procedures in the classes `CcdCalibrationHandler`, `PowerCalibrationHandler`, and `Rejection_`

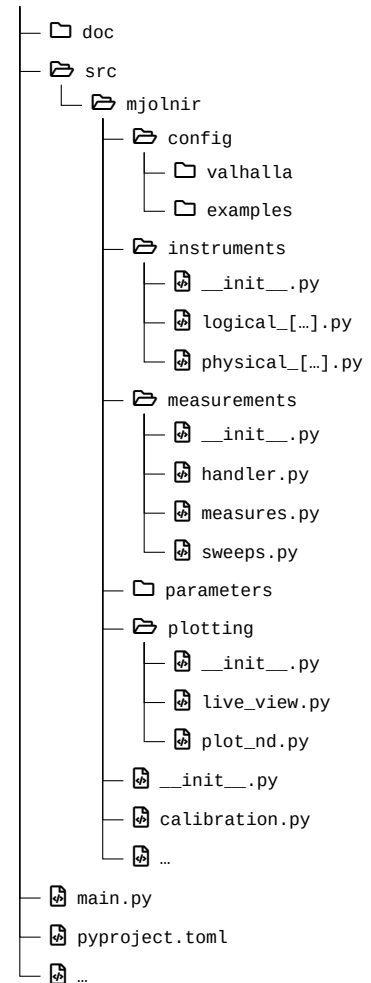


Figure 3.2: Source tree structure of the `mjolnir` package. Logical QCoDeS instruments and parameters are defined in the `instruments` and `parameters` modules, respectively. Instruments are configured using `yaml` files located in a `config` subdirectory. The `measurements` module provides classes for the abstraction of measurements using QCoDeS underneath. Live plots of instrument data as well as a plot function for multidimensional measurement data are defined in the `plotting` module. `calibration.py` contains routines for power, CCD, and excitation rejection calibrations. The `main.py` file is a code cell-based script that serves as the entrypoint for measurements.

¹⁰: Using the QDevil QDAC-II’s built-in `ArrangementContext` virtual gate functionality.

`FeedbackHandler` (see Figure 3.1). As their names suggest, these handle calibration of the CCD pixel-to-wavelength conversion, the power transmission through the rotatable ND filter, and the waveplate and polarizer angles for optimal laser rejection, respectively.

3.3.1 CCD calibration

Because the dispersion of the spectrometer gratings depends to a small degree on wavelength, the calibration function converting horizontal CCD screen pixels into wavelengths needs to be updated for every central wavelength selected using the grating. In principle, this requires measuring the position of several reference wavelengths on the CCD screen and fitting a polynomial of second or third degree. As the tunable cw laser is coupled to a wavelength meter with built-in calibration lamp (HighFinesse WS6), it lends itself naturally as a source of the reference wavelength. In practice, the deviation from an established calibration function is usually small enough that simply shifting the center pixel (that is, the zeroth-order polynomial term) suffices for reasonably small wavelength ranges of tens of nanometers. The `CcdCalibrationHandler` implements three different calibration schemes specified as the `ccd_calibration_update_mode` parameter of the `DetectionPath` instrument:

1. **"full"**. The pixel position of the maximum intensity of nine equidistant wavelengths centered around the grating central wavelength and spread out over the entire range of the CCD screen (~ 45 nm for the 600 gr/mm grating and ~ 9 nm for the 1800 gr/mm grating) is measured sequentially and fitted to a third-degree polynomial.
2. **"fast"**. The laser is set to the grating central wavelength and the zeroth-order coefficient of the previous calibration polynomial is shifted by the pixel distance between the peak and the horizontal center of the CCD screen.
3. **"dirty"**. The zeroth-order coefficient of the calibration polynomial is shifted by the difference in nominal grating and laser wavelengths.

By default, the **"dirty"** mode is enabled as it does not require any grating moves or wavelength changes and is therefore the fastest. Rather than recalibrating, old calibration data can also be loaded from disk if it is not older than a user-specified date. Finally, note that the spectrometer grating motor also requires occasional recalibration. Both the coefficient of linearity (converting motor steps to selected central wavelength) and the offset in motor steps can change over time. Currently, this calibration is not automated but is instead compensated for by shifting the central wavelength on the CCD screen. In principle, the driver for the Horiba FHR1000 spectrometer implements all necessary functionality for automating the calibration procedure already.

3.3.2 Power calibration

The ND filter¹¹ mounted on the Thorlabs K10CR1/M rotation stage has a continuously variable optical density (OD) (??) of 0.04 to 4.0, which depends quite sensitively on the wavelength. In order to allow reliably setting a specified excitation power at any excitation wavelength, the *mjolnir* package automates the calibration of the filter angle against transmitted power. Two modes are implemented, **"full"** and **"fast"**. In the former mode, the transmitted power is sampled at a given angular

11: Thorlabs NDC-25C-4 [108].

interval and the resulting data fitted using a quadratic smoothing spline. Figure 3.3 shows a typical measurement and spline fit at 795 nm. The specified power is then set by inverting the spline and evaluating at the given power.

As performing the full calibration is quite time-consuming and furthermore the inversion not fully reliable, the "fast" calibration update mode sets the rotator angle by performing a noisy optimization. Here, first the last valid full calibration is loaded and its spline scaled to the current power level. Then, the residual sum of squares between the target power and the power meter reading is minimized using the `noisyopt` package [109] with the starting value given by the angle predicted by the rescaled calibration spline.

3.3.3 Rejection feedback

The excitation rejection by means of cross-polarization extinction has already been discussed in ???. As shown there, the OD achieved by cross-polarizing the excitation beam with the analyzer mounted in the detection path reaches a maximum close to 6 and is extremely sensitive to small variations in the angles of the $\lambda/4$ - and $\lambda/2$ -plates controlling polarization state. Close to the optimum, the OD is well-described by a parabola as function of those angles, with a second-order polynomial coefficient on the order of $-0.15/\text{mdeg}^2$. Since the optics including the waveplates display chromatic dispersion, the excitation rejection needs to be re-optimized whenever the laser wavelength is changed, and the exponential angular dependence of the transmitted intensity places high demands on the dynamic range of the photo-detector used for measurement. Therefore, the reflected laser intensity is measured with the avalanche photodiode (APD) signal digitized by the Swabian Instruments Time Tagger 20 on the side exit port of the spectrometer.¹² The Time Tagger can reliably cover a count rate range from 10^2 cps to 10^6 cps, compared to the Andor iDus 416 CCD covering only 10^3 cps to 10^5 cps.

In the `mjoInir` package, the calibration is then carried out as a bivariate noisy minimization using `noisyopt` [109]. Upon initialization the power is set to a small value to avoid overexposing the detectors. Then, the spectrometer is set to select the laser wavelength, the side exit port is selected, and the optimization over the $\lambda/4$ - and $\lambda/2$ -angles is run within conservatively set bounds of $[-2.5^\circ, 2.5^\circ]$, which has been found to be a good compromise of robustness and convergence speed. A caching mechanism stores the optimal angles together with the current wavelength, which serves as a starting guess upon subsequent calibration runs. The calibration is quite tedious and time-consuming for several reasons. Chiefly, moving the waveplate angles is slow simply because it is a mechanical movement, and optimizers typically do not take into account the distance between subsequent sample points, potentially resulting in unnecessarily inefficient exploration of the parameter space. Incorporating a penalty on the sample distance into the optimization algorithm would hence improve the convergence speed. Additionally, due to vibrations in the cryostat (??), the root mean square (RMS) intensity of the back-scattered laser is large – and larger the closer the excitation rejection is to its optimal value¹³ – and thus requires long averaging times for a robust measurement. Finally, the algorithm outlined above fails when the starting guess is too far away from the optimum, such as when the new wavelength is on the order of tens of nm away from the

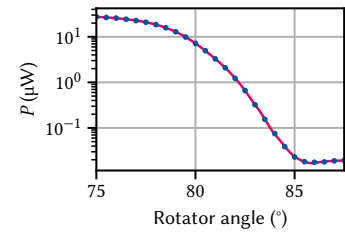


Figure 3.3: Power calibration using the continuously variable ND filter. Error bars from statistics are too small to see. Magenta line is a quadratic smoothing spline.

12: The signals from both APDs are combined to achieve the best signal-to-noise ratio (SNR), see Part II.

13: The count rate can vary by up to a factor of two with the frequency of the pulse tube refrigerator (PTR) pulses.

previously optimized one. A good – albeit time-consuming – strategy is then to incrementally update the wavelength.

3.4 Measurement routines

Measurements in `mjolnir` use the `QCoDeS` infrastructure for data acquisition and storage. To abstract away code for repetitive setup and teardown tasks, the user interacts with a `MeasurementHandler` object through the `measure()` method. The class can be subclassed to customize the aforementioned tasks for different types of experiments (such as those that involve illumination with the laser and detection with the CCD, `LaserCcdMeasurementHandler`), or add default parameters to every measurement (such as leakage currents or the laser power). A measurement's independent parameters are passed to `measure()` as instances of a `Sweep` class which completely determines the measurement structure. `Sweep` objects support syntactic sugar for concatenation (`@`), nesting (`|`), and parallelization (`&`). Dependent parameters (those that should be measured) can be simple parameters or instances of a `Measure` class.¹⁴ The state of external parameters, that is, parameters that are not varied or measured during a measurement, can be defined for the duration of the measurement using the `parameter_contexts` argument, a mapping from `QCoDeS` parameters to valid values thereof. This uses the `Parameter.set_to()` context manager to set the parameters to the given values before the measurement starts and restore their original values upon exit in a controlled manner, allowing users to ensure their device is in a well-defined state. Custom setup and teardown tasks can furthermore be specified through the `add_before_run` and `add_after_run` arguments, respectively.

14: Besides some optimization for measurements of parameters delegating from the same physical parameter, the latter exists mostly for (primitive) live plotting.

```
from mjolnir.measurement.handler import LaserCcdMeasurementHandler
from mjolnir.measurement.sweeps import GridSweep
from mjolnir.measurement.measures import Measure

handler = LaserCcdMeasurementHandler(station)

# excitation_path, sample are instances of the ExcitationPath and
# TrapSample classes, respectively
power_sweep = GridSweep(excitation_path.power_at_sample,
                        rng=(5e-9, 5e-7), num_points=11,
                        spacing='geom')
gate_sweep = GridSweep(sample.trap.central_difference_mode,
                        rng=(-2, -1), num_points=51))

# two-dimensional sweep over power and gate voltage
sweeps = power_sweep | gate_sweep
# keep track of the MXC temperature
measures = sample.fridge.T8

dataset = handler.measure(
    sweeps,
    measures,
    parameter_contexts={
        sample.trap.central_common_mode: -1,
        detection_path.central_wavelength: 825,
    },
    exposure_time=2
)
```

Listing 3.1: Setup and measurement workflow using the `mjolnir` package. `station` is a `QCoDeS Station` object managing the instruments. The `sweeps` object describes a nested loop on whose inner iteration the difference mode parameter of the trap's central gate is swept over a linear grid and on whose outer iteration the laser power, adjusted for the beam splitter ratio, is swept over a logarithmically spaced grid. No dependent parameters (`Measure` objects) need to be explicitly specified as the `LaserCcdMeasurementHandler` measures the CCD spectrum as well as laser power and leakage currents of the swept gates by default. The `parameter_contexts` argument is used to set the spectrometer wavelength to 825 nm and the common mode voltage of the active trap to -1 V. The `exposure_time` argument is passed through to the `initialize` method, where it is used to set up the CCD for acquisition.

A typical workflow for a PL measurement using laser and CCD is sketched in Listing 3.1. The `MeasurementHandler` object automatically takes care of, among other things, arming the CCD, acquiring a background image in the dark, and opening the laser shutter for the duration of the measurement. Acquired data is saved to the QCoDeS database, but a helper function exporting to the xarray Dataset format is available. Saved together with the data are a snapshot of the QCoDeS Station as well as arbitrary custom metadata. More details and examples on the measurement functionality can be found in the documentation.¹⁵ Lastly, I note that the measurement functionality in `mjolnir` is independent of the instrument abstraction and calibration logic and as such could be replaced or augmented with minimal effort by that of other QCoDeS-based frameworks such as `quantify` or `labcore` to make use of their infrastructure. I leave this option for future work.

15: https://qutech.pages.git-ce.rwth-aachen.de/lab_software/python-mjolnir/

3.5 Plotting

Optical measurements using `mjolnir` often produce multi-dimensional datasets by virtue of the default parameter measured, the CCD spectrum, being vector-valued or *batched*. To visualize such datasets with more than two dimensions, `mjolnir` provides the `plot_nd()` function that plots 2D slices through the data as a false-color image and generates interactive slider widgets that allow users to modify the slice coordinates. This facilitates interactively exploring large datasets and recognizing trends present in the data beyond two dimensions. Figure 3.4 shows an exemplary plot window for a four-dimensional data set obtained from a CCD measurement sweeping laser wavelength, power, and a gate voltage, with Listing 3.2 showing the code necessary to produce the plot.

The plotting functionality is implemented using `matplotlib`. While not the most performant library, its flexibility in decorating and customizing plots as well as scaling data, such as the `asinh`-scale normalization used in Figure 3.4, made it the preferred choice. To nonetheless improve the responsiveness of the interactive elements, the plotted artists are *blitted*¹⁶ using the `qutil.plotting.BlitManager` class from the `qutil` library [110]. The data variable to be shown in the main panel can be selected with the `array_target` argument, which accepts a string and chooses the closest match in the dataset since the full parameter names are often a bit unwieldy. Similarly, the coordinates to be plotted on the *x*- and *y*-axes are selected with the `horizontal_target` and `vertical_target` arguments, respectively.

16: Blitting refers to storing constant backgrounds of raster graphics and only redrawing changing elements. See the `matplotlib` documentation.

In addition to plotting measurement data, `mjolnir` implements live plotting of instrument data leveraging the `qutil.plotting.live_view` module. Since most instruments do not support multiple concurrent connections, switching control between the Python console and the graphical user interface (GUI) program provided by the manufacturer can often be

```
import matplotlib as mpl
from mjolnir.plotting import plot_nd

fig, axes, sliders = plot_nd(
    dataset_or_run_id=140, vertical_target='power_at_sample',
    yscale='log', norm=mpl.colors.AsinhNorm(vmin=0),
    fig_kw=dict(figsize=(6.33585, 4.6))
)
```

Listing 3.2: Code to produce the plot shown in Figure 3.4. If `dataset_or_run_id` is an integer, the currently connected QCoDeS database is queried for this run identifier. Otherwise, it should be an xarray Dataset.

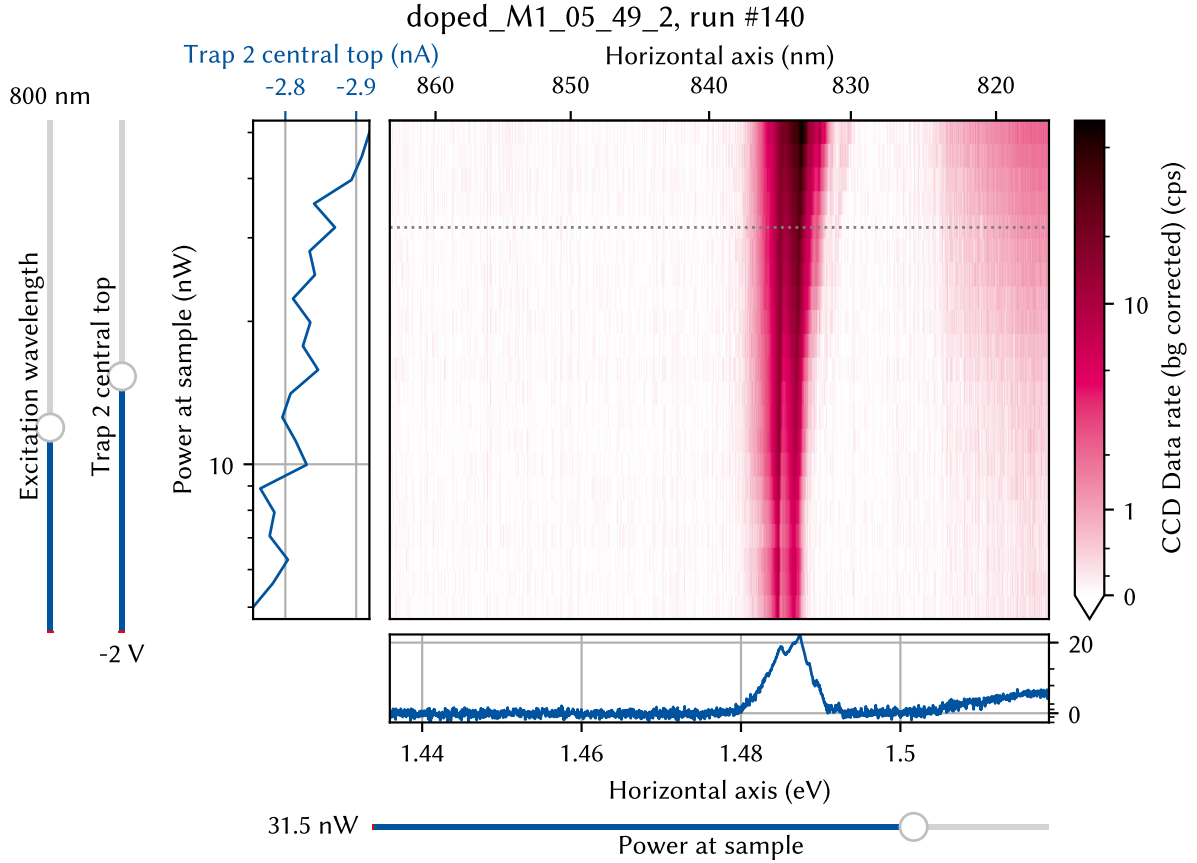


Figure 3.4: The `plot_nd()` plot window. The bottom panel, enabled by default, shows a horizontal line cut through the 2D data of the main panel whose y-value can be set with the adjacent slider widget. The left panel shows the leakage currents of gates that participate in the sweep and, if measured, the laser power. A vertical slider widget is added for each data dimension not displayed on the x or y axis of the main plot. The figure title shows the sample as well as the measurement identifiers assigned by QCoDeS.

tedious.¹⁷ Thus, making use of their continuous data acquisition functionality is prohibitively time-consuming, but at the same time optical experiments frequently call for live observation of instrument data, for example when aligning the optics. Live plotting is currently implemented for three different instruments and corresponding parameters; the Thorlabs PM100D power meter (power reading), the Andor iDus 416 CCD (spectrum or image), and the Swabian Instruments Time Tagger 20 counting card (count rate(s)). Data acquisition is executed in a background thread while the plot, implemented in `matplotlib`, currently runs in the main thread, and hence does not update while the interpreter is blocked. In principle, though, the `live_view` module also supports plotting in a separate process, making a multiprocessing implementation straightforward. Interactive GUI elements in the `matplotlib` figure allow for pausing and automatically rescaling the data.¹⁸ Since for the CCD data acquisition runs using the *run till abort* mode of the device and as such continuously, the instrument is blocked for the duration of the live plot and it therefore needs to be closed before starting a measurement. By contrast, the power meter and Time Tagger parameters are simply queried regularly in sequential mode and can hence in principle remain open and running while performing measurements.

17: For instance, the CCD GUI, Andor Solis, by default disables the thermoelectric cooler when exiting the program.

18: These two features can also be activated with the `SPACE` and `R` keys.



Photoluminescence measurements of doped semiconductor membranes

4

In this chapter, I present and discuss optical measurements of gated semiconductor membranes. All of the samples under investigation had the almost same nominal heterostructure layout; a 20 nm GaAs QW sandwiched between two modulation-doped 90 nm $\text{Al}_{0.33}\text{Ga}_{0.67}\text{As}$ barriers of which 50 nm are an undoped spacer layer. Together with either a 5 nm or 10 nm GaAs cap to on both sides to protect the aluminium from oxidation, the membranes had a thickness of 210 nm or 220 nm after thinning.

Gate electrodes were patterned on the top and bottom side of the membrane using electron-beam lithography (EBL), where here and elsewhere in the present thesis I refer by “top” to gates on the etched and by “bottom” to those on the as-grown surface. That is, “top” gates are on the air side facing the microscope objective when the sample is mounted in the fridge, whereas “bottom” gates are in contact with the epoxy gluing them to the Silicon host chip. Typical designs have gates on the top and bottom sides of the membrane that are contacted at different positions on the edge of the mesa and converge towards the exciton trap site, where only there they overlap laterally. For details about the fabrication process, refer to References [64](#) and [74](#).

I installed and cooled the samples to Millikelvin temperatures in the dilution refrigerator (DR) introduced in Part II, typically using the bottom-loading technique. As detailed there, PL measurements can be performed by illuminating the sample with a cw laser above the band gap through an objective lens in front of the sample. The emitted PL radiation is picked up by the same lens and coupled into a single-mode fiber (SMF) outside the fridge, from where it is sent to a diffraction grating spectrometer with a CCD for spectral analysis.

In total, I show measurements from three different samples. Unfortunately, none of the samples tested had a fully functional exciton trap with four working gates. Several old samples fabricated during the work of Descamps [[64](#)] appeared to have aged, resulting in broken gates or otherwise unconventional behavior. Newly fabricated samples on old heterostructure pieces frequently showed contact problems, either of optical gates to the mesa, between different EBL resolution steps, or Ohmics, while other gates had leakage to ground or the QW.

I pursued two different approaches to positioning the laser on the samples. The first was using the white-light imaging arm of the confocal microscope (see Part II). The larger, thicker gate structures on the samples typically show good contrast in the complementary metal-oxide-semiconductor (CMOS) camera image owing to the large reflectance of Au compared to GaAs (at normal incidence and a single interface $\mathcal{R} = 98\%$ and 32% , respectively, see Section 4.3), allowing orientating oneself following the sample design. However, the simplicity of the optics¹ results in a comparably poor contrast for the smallest features on the scale below $1\text{ }\mu\text{m}$. The magnification factor of the microscope is 30, resulting in a feature size of 160 nm per pixel on the camera. In the best-case scenario, the cryostat vibration noise is on the order of 100 nm RMS (??), or very roughly one pixel. Resolving features only a few pixels in size is thus clearly on the edge of the microscope’s capabilities. Positioning the sample in this way is usually fairly reliable with some experience if one

1: The objective is just a singlet lens, compared to sophisticated commercial objectives containing a large number of optics inside to correct optical aberrations. See for example the [Attocube LT-APO/LWD](#).

takes visual identification of the exciton trap gates as a target. In practice, it is still necessary to fine-tune the position once the light source is switched to the laser because first, the focal distance of the objective lens shifts slightly when switching from a broadband to a monochromatic light source, and second, the focal spot of the laser is much smaller than that of the white light.²

The second approach is to roughly align the position on a large gate feature using the camera image, switch to laser illumination, and monitor the PL signal when biasing the gate. One can then move along the gate towards the exciton trap by following the PL features expected for a gate: a reduced QW emission due to absorption (see Section 4.3) and enhanced reflection of the laser line, as well as a Stark-shifted PL. This has the advantage that the functionality of the gate can be monitored. Biasing also the other gates of the trap under investigation, one can then look for additional Stark shifting of the PL. If the effect of each gate voltage can be observed, the position of the laser will be close to the trap center, and can then be optimized further. While this is in a sense flying in the dark, it is a quite reliable method for an experienced experimentalist if the gates are fully functional.

4.1 Photoluminescence spectroscopy

Figure 4.1 shows a typical PL spectrum obtained on the bare, unbiased QW of a doped membrane sample. This measurement corresponds to the configuration already discussed in Section 2.1. Due to the Pauli exclusion principle, electrons require an energy of at least $E_F (1 + m_c^*/m_{hh}^*)$ above the band gap and, because of the vanishingly small photon momentum, a momentum of at least k_F to be excited into a free state above the Fermi level μ (dotted gray line).³ Once excited, they quickly relax down to the Fermi edge at μ from where they can recombine emitting a photon. As the Fermi sea is at a finite temperature, the high-energy shoulder of the PL spectrum is hence thermally broadened according to the Fermi distribution function of the electron gas (dashed gray line). The associated temperature is around 1.5 K and hence orders of magnitude higher than the lattice temperature of 10 mK. This effect has already been observed by Pinczuk et al. [113]. Like in those experiments, the temperature of the Fermi edge does not vary significantly with excitation power, making local heating of the lattice due to high excitation power an unlikely cause [114]. I show a power-dependence measurement of the Fermi edge supporting this statement in Appendix B. Bockelmann and Bastard [115] showed that in low-dimensional electron gases electron cooling by phonon emission is limited by a finite scattering rate. Thus, under continuous excitation a quasi-equilibrium is established as hot electrons cannot lose heat quickly enough. Although their simulations were performed for higher temperatures and smaller confinement widths, their results of electron temperatures in the range of 2 K for lattice temperatures of 300 mK is comparable to ours.

PL emission is possible also at lower energies as electrons inside the Fermi sea recombine with the free photo-hole that scatters towards the valence band edge. The band gap then defines the low-energy shoulder of the PL spectrum, below which there are – ideally – no states available (dotted gray line). However, the PL reveals there are indeed free states decaying exponentially into the gap, originating most likely from impurities (dashed gray line). Compared to the results of Kamburov et

2: The white light is launched from a 400 μm diameter multi-mode fiber (MMF), compared to a 5 μm diameter SMF for the laser, resulting in a spot 80 times larger.

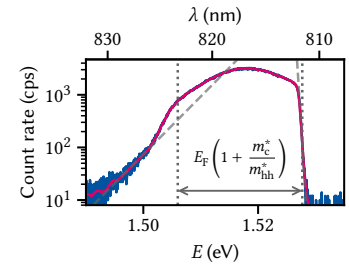


Figure 4.1: PL of the bare 2DEG. Magenta line is a smoothing spline fit to the data. Indicated by dotted gray lines are the Fermi edge at high and the band edge at low energy. The Fermi edge has a Fermi distribution (exponential indicated by a dashed gray line) whose temperature is typically much higher than the lattice temperature (~ 1 K). Below the band edge there is an exponential tail (dashed gray line) due to impurities that permeates far into the gap.

3: This is known as the Burstein-Moss shift [111, 112].

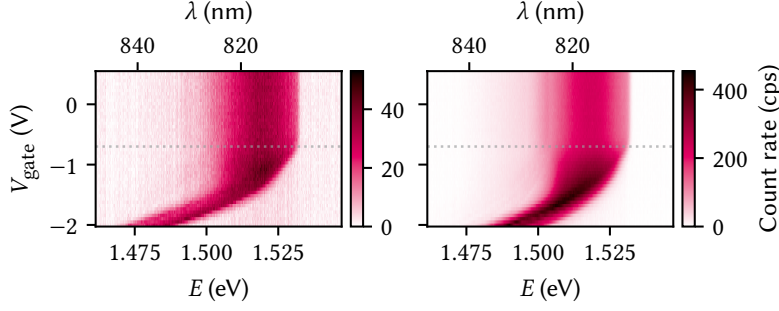



Figure 4.2: PL as function of gate voltage on a single fan-out gate on the bottom (left) and top (right) side of the membrane. The behavior is qualitatively similar but the overall quantum efficiency lower by an order of magnitude for gates on the bottom (as-grown buried) side. Dotted gray lines are a guide to the eye demonstrating that the changes to the PL spectrum set in at the same voltage for both types of gates (around -0.7 V).

al. [81], the PL spectra obtained here are much flatter over energy, with the PL peak typically close to the middle between gap and Fermi edge. Conversely, Kamburov et al. [81] observed a strong peak at the band gap,⁴ indicating that in our samples holes are more strongly localized and therefore have a wider spread in k -space, enabling transitions in a wider range of wave vectors [84]. This would in turn imply increased alloy disorder or interface roughness [86], an observation we shall come back to in Section 4.2.

From the width of the 2DEG emission, we can calculate the charge carrier density by relating it to the Fermi energy in two dimensions [67, 113],

$$n = \frac{m_c^* E_F}{\pi \hbar^2} = \frac{\mu \Delta E}{\pi \hbar^2}, \quad (4.1)$$


where ΔE is the bandwidth of the emission (dashed gray lines in Figure 4.1) and $\mu = m_c^* m_{hh}^* / (m_c^* + m_{hh}^*)$ is the reduced mass of conduction and valence band. For this particular sample, Equation 4.1 yields $n = 5 \times 10^{11} \text{ cm}^{-2}$ or, equivalently, $E_F = 18 \text{ meV}$ and $k_F = 1.8 \times 10^8 \text{ m}^{-1}$. Comparing this value to that obtained from a simulation of the heterostructure with nominal doping concentration $N_d = 6.5 \times 10^{17} \text{ cm}^{-3}$ using a self-consistent Poisson-Schrödinger solver [116], $n = 1.9 \times 10^{11} \text{ cm}^{-2}$ (refer to Appendix B for simulation parameters), shows a significant discrepancy indicating a severe mismatch between nominal and actual doping concentrations.⁵ Finally, we observe that the gap according to the preceding analysis is redshifted from the undoped bulk gap of 1.519 eV [66] by 13 meV .⁶ Descamps [64] hypothesized that the removal of the GaAs substrate and the associated change in strain leads to this lowering of the band gap. However, this effect was also already observed by Pinczuk et al. [113] in “bulk” modulation-doped GaAs QWs. There, the authors put forth a renormalization of the band gap due to many-body interactions as an explanation, an interpretation since well-agreed upon [117] 

5: Note that the carrier density obtained thus does not vary significantly with excitation power, ruling out photo-doping as a source of the discrepancy. See Appendix B for a measurement of the 2DEG PL as function of power.

6: The redshift is in fact larger still due to the confinement energy of the QW, estimated to be 17 meV in Section 2.2.

4.1.1 Quantum-confined Stark shift

Let us now address the behavior of the PL under electric fields. To this end, the laser is positioned on an EBL-written gate and a negative voltage is applied to the gate. Figure 4.2 depicts two measurements on a well-behaved sample. The left (right) panel shows the PL as function of voltage with the laser positioned on a bottom (top) gate. In contrast to the intuition obtained in Section 2.2, there is no immediate effect to be observed once the voltage is switched on. This is most likely due to the presence of the 2DEG screening the external electric field. At $V_{\text{gate}} = -0.7 \text{ V}$, the high-energy shoulder of the emission starts to shift towards lower energies while the low-energy shoulder stays invariant. Per


the previous section, we can interpret this as the charge carrier density and thereby the Fermi energy being lowered as the 2DEG is depleted. As the electric field tilts the bands, the band edges of both conduction and valence band shift by the same amount and therefore the band gap is not modified in this regime.⁷ As the 2DEG is gradually depleted, a broad exciton peak emerges that shifts approximately quadratically with the applied voltage as ionization from the interaction with the Fermi sea of electrons becomes less pronounced (*cf.* Section 2.1). Beyond -1.5 V, the 2DEG is completely depleted. The voltage difference between onset and completion of the depletion matches roughly the value expected from a simulation with  screening for the nominal device parameters (see Tables B.1 and B.2), -0.7 V.

Besides the voltage dependence, another feature stands out from Figure 4.2: the PL intensity is lower by an order of magnitude when on top of a back gate compared to a top gate. This is at first puzzling, as in the latter case there is an additional semi-transparent gate⁸ absorbing and reflecting both laser and PL radiation, whereas in the former there is only the bare heterostructure, so we would expect the exact opposite! I elucidate this issue in Section 4.3.

Moving to a large exciton trap with a single set of top and bottom gates and $5\text{ }\mu\text{m}$ diameter, we can measure the behavior of the Stark shift in the intended setting of local confining gates on either side of the membrane. We define the virtual gates

$$V_{\text{DM}} = V_{\text{T}} - V_{\text{B}}, \quad (4.2)$$

$$V_{\text{CM}} = V_{\text{T}} + V_{\text{B}}, \quad (4.3)$$

where DM (CM) stands for difference (common) mode and T (B) for top and bottom, respectively. Clearly, V_{DM} should ideally be proportional to the out-of-plane electric field across the membrane, $V_{\text{DM}} = Ft$ with t the membrane thickness, whereas V_{CM} should tune the band edge offset from the Fermi level μ . As we observed previously, the presence of the 2DEG screens the electric field generated by V_{DM} . A good operating point is therefore at a negative V_{CM} which should deplete the 2DEG (or at least reduce the charge carrier density). Figure 4.3 shows a PL map as function of the difference mode voltage V_{DM} at $V_{\text{CM}} = -1.3$ V. From Figure 4.2, where the optical measurement of the charge carrier density results in a similar value as for the sample in Figure 4.3, $n \sim 5 \times 10^{11} \text{ cm}^{-2}$, we would expect this common mode voltage to suffice in at least overcoming the screening and reducing the carrier density in the QW. However, there is clearly still 2DEG emission present for a large range of V_{DM} , and the Fermi edge is at the same energy as without a gate bias. Overall, the Stark shift pattern is symmetric but offset by $V_{\text{DM}} = 0.75$ V. This behavior is also observed in the response of the PL to a single gate in this and several other samples, where the onset of an effect by bottom gate is significantly later than that for the top gate, suggesting that the voltage is screened by some mechanism and the bottom gate has a much smaller lever arm than the top gate. Perhaps surprisingly, the gates on the *bottom* side of the membrane display this behavior, *i.e.*, the gates on the *as-grown* surface.⁹ This makes surface states an unlikely candidate for the screening as the quality  of the grown surface should be better than that of the etched surface [64]. A possible cause might be oxygen segregation during growth¹⁰ or other impurities [118].

The fact that the 2DEG is depleted by V_{DM} in the range -0.2 V to -1.4 V and above 1.5 V at all is unexpected. Even with a difference in lever arms as just discussed, the symmetric dependence of the PL emission on V_{DM}

7: We would in fact expect a slight increase in confinement energy as the carrier density is lowered because the band bending due to the surplus electric charge of the 2DEG is lifted.

8: 7 nm Au with a 2 nm Ti adhesion layer.

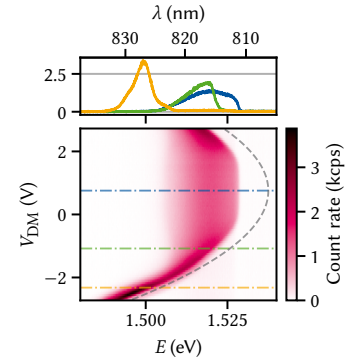


Figure 4.3: PL as function of difference-mode voltage on a large exciton trap. The observed Stark shift follows roughly the expected quadratic dispersion, but is offset by 0.75 V with respect to zero bias. Dashed gray line is a guide to the eye of a parabola with curvature -3.5 meV/V^2 . Line cuts in the upper panel are taken at the voltages indicated by dash-dotted lines in the lower.

9: I note that the sample of Figure 4.2 was fabricated on the same heterostructure as the device in Figure 4(d) of Reference 65, which showed little to no electrical hysteresis unlike most other samples investigated by Descamps [64].

10: A. Ludwig, private communication.

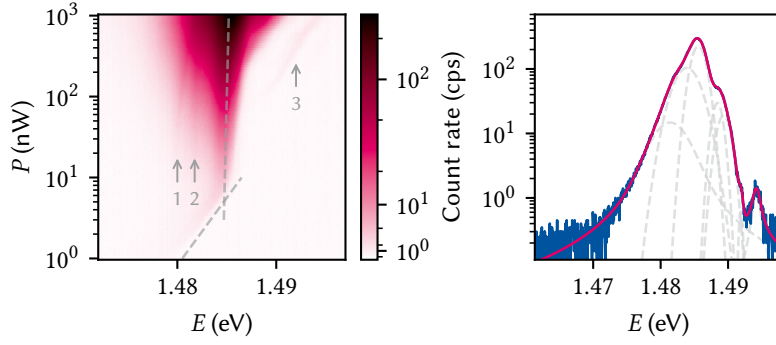


Figure 4.4: PL as function of excitation power P . In the left panel two qualitatively different regimes are indicated by dashed gray lines as guides to the eye; below 10 nW, the main peak displays a blueshift logarithmic in excitation power, $E = 1.485 \text{ eV} + 5 \text{ meV} \log_{10} P$. Above, the blueshift diminishes significantly. Three additional lines, indicated by arrows, with varying power dispersion are visible. Right panel shows a fit to data at $P = 1 \mu\text{W}$. A sum of seven individual lines (dashed, gray) is required to fit the data. The dashed gray lines are the individual contributions.

implies that $V_{\text{DM}} - 0.75 \text{ V}$ *should* correspond to the out-of-plane electric field such that the energy is unchanged in the middle of the quantum well, $V_{\text{DM}} - 0.75 \text{ V} \propto F(z - t/2)$. Staying in the virtual gate picture, a difference in relative lever arms¹¹ $\Delta\alpha = \alpha_{\text{T}} - \alpha_{\text{B}}$ between V_{T} and V_{B} should modify the virtual gates as

$$\begin{pmatrix} \tilde{V}_{\text{DM}} \\ \tilde{V}_{\text{CM}} \end{pmatrix} = \frac{1}{\sqrt{1 + \Delta\alpha^2}} \begin{pmatrix} 1 & \Delta\alpha \\ -\Delta\alpha & 1 \end{pmatrix} \begin{pmatrix} V_{\text{DM}} \\ V_{\text{CM}} \end{pmatrix} \quad (4.4)$$

$$= \frac{1}{\sqrt{1 + \Delta\alpha^2}} \begin{pmatrix} 1 + \Delta\alpha & -1 + \Delta\alpha \\ 1 - \Delta\alpha & 1 + \Delta\alpha \end{pmatrix} \begin{pmatrix} V_{\text{T}} \\ V_{\text{B}} \end{pmatrix} \quad (4.5)$$

and as such not modify the qualitative behavior of V_{DM} besides the offset.¹² That is, in and of itself, V_{DM} should not reduce the charge carrier density in an isolated QW to first order.¹³

One possible explanation for the observed behavior is the depletion of the 2DEG by electrons tunneling out of the well and recombining with the donor ions, rendering one of the doped barriers electrically neutral. With the doping pulling down the conduction band between 50 nm and 90 nm away from the QW, the tunneling rate will be more pronounced than estimated for the undoped case in Section 2.2. Taking the large trap diameter in this case into account, there are $\sim 10^5$ electrons in the unbiased QW on the area of the trap gates. Thus, at a tunneling rate of 1 MHz, all electrons would tunnel out of the QW within 100 ms on average, putting a response of the system into the steady state within the fairly long time scales of a PL measurement¹⁴ well within reasonable bounds. In the literature, this is known as carrier sweep-out and has been studied in the context of solar cells and other electroabsorptive devices [99, 120, 121].

The dashed gray line in Figure 4.3 shows a parabola, $\Delta E \propto \alpha V_{\text{DM}}^2$, with curvature $\alpha = -3.5 \text{ meV/V}^2$ as a guide to the eye. For difference-mode voltages below -1.8 V , the exciton Stark shift follows this quite closely. The upper panel depicts three line cuts at the positions indicated by the dash-dotted lines in the main panel. As can be seen from the cut at -2.3 V (orange), the line shape appears to consist of three individual emission lines assigned by Descamps [64] as the neutral, singly, and doubly negatively charged excitons. I return to the question of line assignment below.

4.1.2 Power dependence

As outlined in Section 2.3, the dependence of emitted PL power on excitation power of individual emission lines can help inferring the exci-

11: Relative gate lever arms are unitless parameters used to quantify the degree of cross-coupling between gates, in contrast to the physical lever arms used to quantify the change in electron energy versus gate voltage employed in ?? . See for example Reference 119.

12: Setting $\Delta\alpha = 0.6$ yields a \tilde{V}_{DM} for which the Stark shift in Figure 4.3 is symmetric about zero.

13: We might instead expect a small change in the apparent gap energy as the well is tilted.

14: Say 0.1 s to 10 s.

tonic species responsible. Moreover, as the density of excitons depends on the excitation power, interaction effects between them influence the energy of the emission. Such a measurement is shown in the left panel of Figure 4.4 for the same common-mode voltage as in Figure 4.3 and $V_{DM} = -2.7$ V (*i.e.*, corresponding to the lowest line in that plot) where the 2DEG is completely depleted. Two qualitatively different regimes can be observed as indicated by the dashed gray lines as guides to the eye. Below 10 nW excitation power, corresponding to approximately 0.75 W/cm² at the beam diameter measured in Part II, the main line displays a blueshift logarithmic in excitation power. Above this value, the blueshift is much less pronounced. It is not understood though why the blueshift abruptly changes in quality at 10 nW excitation power. At powers above 10 nW, two additional lines on the low-energy side of the main peak become visible that appear to converge towards higher powers, while above 100 nW a line appears on the high-energy side that has a similar blueshift as the main peak at low powers. In principle, the blueshift as function of power is to be expected. Increasing the excitation power increases the density of excitons, either because they are spatially localized or because of a finite diffusion speed. The increased density corresponds to an increased overlap of single excitons' constituents and thus in turn leads to an increasingly repulsive Coulomb interaction that raises their energy.¹⁵ This mechanism underpins the use of exciton traps such as SAQDs as single-photon sources; upon spectrally filtering on the emission wavelength of a single exciton, only a single photon can be emitted from the trap at a time since the presence of another exciton in the trap would shift the emission energy of both.

The right panel shows a line cut taken at 1 μ W. A weighted sum of seven individual Voigt profile line shapes [122],

$$V(E; \sigma, \gamma) = G(E; \sigma) * L(E; \gamma), \quad (4.6)$$

that is, a convolution of Gaussian and Lorentzian line shapes given by

$$G(x; \sigma) = \frac{1}{\sigma\sqrt{2\pi}} \exp\left(-\frac{x^2}{2\sigma^2}\right), \quad (4.6a)$$

$$L(x; \gamma) = \frac{1}{\pi} \frac{\gamma}{\gamma^2 + x^2}, \quad (4.6b)$$

is required to obtain an adequate fit. The Voigt profile arises from a combination of two separate line broadening mechanisms that manifest as a Gaussian (Equation 4.6a) and Lorentzian (Equation 4.6b) line shape. The former describes inhomogeneous broadening due to noise faster than the data acquisition time, whereas the latter is the homogeneous broadening due to for example the finite lifetime of the emitting state¹⁶ or power broadening [123]. All but the two outermost lines in the best fit are dominated by the inhomogeneous, Gaussian contribution to Equation 4.6 with widths σ in the range of 0.1 meV to 1 meV and a peak separation on the order of 2 meV.¹⁷

According to Reference 64, the lifetime of a Stark-shifted exciton is on the order of 1 ns due to the reduced wave function overlap. This corresponds to a homogeneous linewidth of $2\gamma = \hbar/\tau \sim 660$ neV, several orders of magnitude below the observed linewidth, and it is thus consistent with the fact that most peaks are best fit by inhomogeneously broadened line shapes. The large a number of lines is certainly unexpected and cannot be explained by different excitonic species. Where it is possible to track individual peaks as function of excitation power, their



15: Of course, the opposite – an attractive interaction – is also possible for small numbers of excitons, resulting in biexcitons. The two cases can be thought of analogously as bonding and anti-bonding orbital configurations.

16: This is also known as the linewidth's transform limit; energy and (life)time are Fourier pairs by Heisenberg's uncertainty principle.

17: The large number of Voigt profiles used to fit the data does tend to overfit the data.

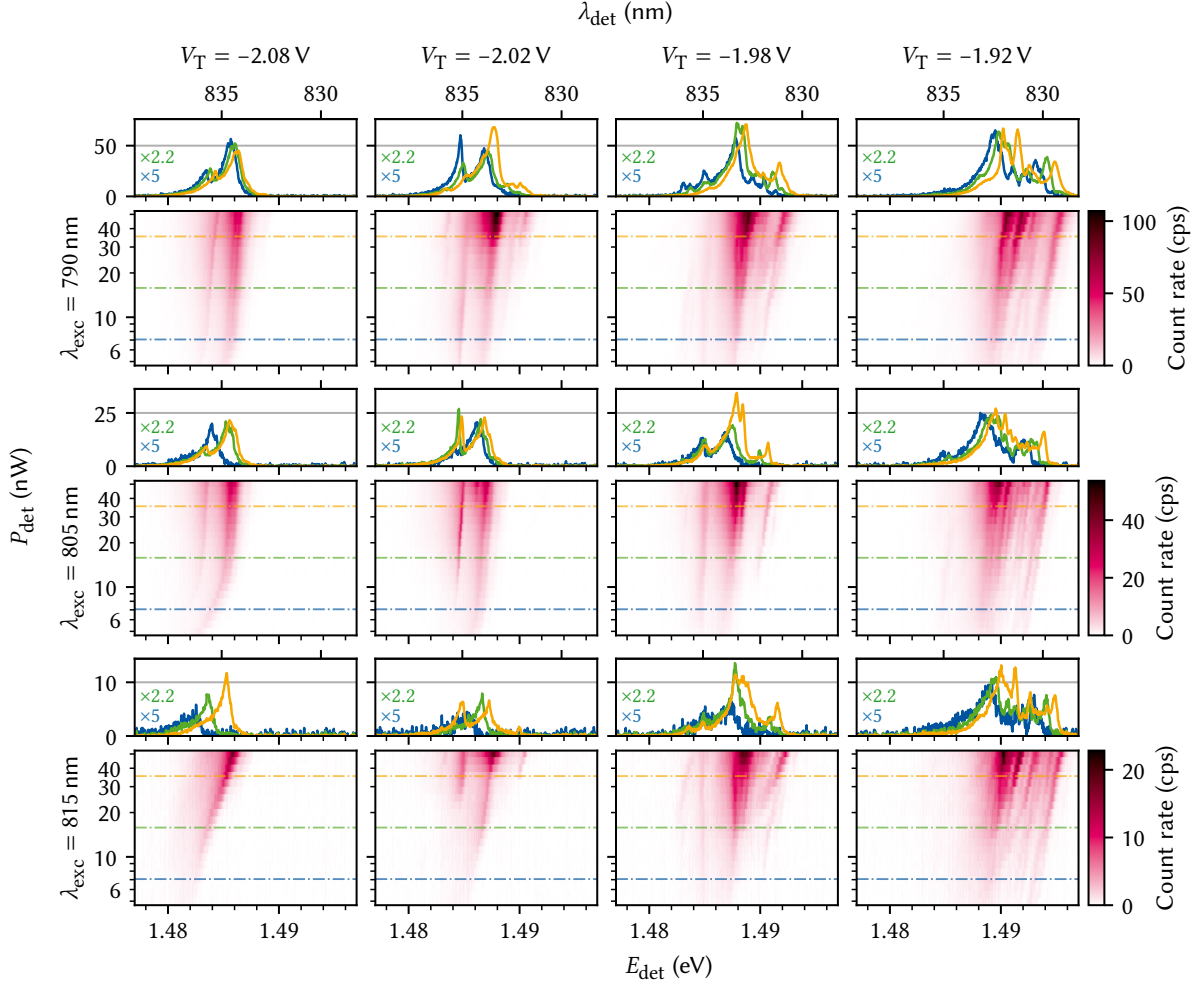


Figure 4.5: Wide-range PL parameter sweep on a large exciton trap plotted as function of excitation power and detection energy. Rows are data for three different excitation wavelengths, columns for four different top gate voltages V_T and share color and line cut scales. Line cuts are taken at the indicated positions of $P_{\text{det}} = 7$ nW, 16 nW, and 35 nW and drawn scaled by the fraction of excitation power with respect to 35 nW.

power dependence is linear, $\int dE V(E) \propto P$, suggesting neutral excitons or band-to-band recombination as origins of the emission.

A possible explanation for the multitude of lines is thus that they originate from different spatial locations, a hypothesis we return to shortly. First, let us conclude this section with a large parameter sweep of this trap, shown in Figure 4.5. Each of the three rows (with separate panels for line cuts each) show data for different excitation wavelengths, λ_{exc} , each of the columns show data for different top gate voltage, V_T , and the PL is plotted as function of detection energy, E_{det} , and excitation power, P_{exc} . The line cuts taken at lower powers (blue and green) are scaled to match the one at the highest power (orange) assuming a linear power dependence. For all data $V_B = 0$ V so that $V_T = V_{\text{DM}} = V_{\text{CM}}$. Despite the comparatively small changes in voltage, the behavior of the sample changes significantly. Whereas for $V_T = -2.08$ V the observed PL features are similar to those in Figure B.2, at $V_T = -1.92$ V there is a very large number of lines in the spectrum, most but not all of which share the same blueshift as function of excitation power. The effect of a different excitation wavelength appears to mostly be a shift of the features along the excitation power axis and thus simply a change in absorption

efficiency, although some features also change qualitatively. I discuss the wavelength dependence in more detail in Section 4.2.

So what is the origin of the substructure of the PL emission? The peak distance is on the order of 1 meV. This value is on the order of magnitude of the change in ground state energy, 470 μeV , we would expect from fluctuations in the width of the QW by one atomic layer of GaAs with lattice constant $a = 5.65 \text{ \AA}$ ¹⁸ for the design well width $L = 20 \text{ nm}$ (Section 2.1). Indeed, there exists a large body of literature that has examined the influence of interface roughness and QW thickness fluctuations on the exciton PL [124–126]. Not only do atomic steps and islands lead to increased PL linewidth and energy shifts, but in fact also to the possible localization of single excitons [127–129]. That is to say, QDs have been found to form at such interface fluctuations. Comparing the spectra shown in Figure 4.5 to those shown by Brunner et al. [127, Figure 1], our main PL line is more reminiscent of what the authors there label as the 2D exciton; our spectra do not show well-separated and sharp lines on the low-energy side of the spectrum. By contrast, the PL spectrum shown by Zrenner et al. [129, Figure 1] is very similar to the one observed here, although they assign this peak to indirect transitions from the AlAs X valley to the GaAs Γ valence band valley in their AlAs/GaAs coupled QW structure, a situation quite unlike ours.

An intricate substructure of the PL emission at lower excitation powers such as this was also observed in other samples. If the individual lines originated from 0D-confined QDs, we would expect their PL emission to display signatures of a single-photon source as outlined above. I therefore performed a $g^{(2)}$ measurement (see ??) on a line that was narrow ($\sim 1 \text{ meV}$) and fairly well-separated such that at its full width at half maximum (FWHM) was resolvable. I excited the sample above the gap and spectrally filtered the emitted PL by using the spectrometer as a monochromator with bandwidth given by the line FWHM. Due to the low brightness, a compromise between high excitation power (leading to power broadening) and measurement duration (to gather statistics) was chosen at 100 nW. However, after 48 h no deviation from a flat and uncorrelated $g^{(2)}$ could be observed.¹⁹

4.1.3 Spatial dependence

As mentioned several times already, the nanopositioners on which the sample is mounted show hysteresis and are therefore not suited for reproducible spatial maps of the sample. The hysteresis is due to the non-adiabaticity of the method of movement in the so-called slip-stick mode (*cf.* ??). What is more, the resistive position readout is also fairly unreliable below, say, 5 μm resolution. Nonetheless, we can at the very least perform simple one-dimensional sweeps after manually positioning the sample at a given starting position and assume that the displacement per step has some sufficiently narrow distribution around a fixed mean. A more sophisticated algorithmic approach using feature detection may allow also two-dimensional maps with a reasonable accuracy.

Figure 4.6 shows the PL collected from the sample as the positioner is stepped perpendicularly across an unbiased gate. The vertical axis also gives a position coordinate which is computed from the steps by fitting the position readout once hysteresis has worn off. The blue and green dash-dotted line correspond to the center of and beside the gate, respectively, with line cuts drawn in the upper panel. Clearly, the PL intensity is quenched significantly by the gate, beyond what one could expect from

18: Meaning the thickness of a single atomic layer is $a/2$.

19: I also attempted a $g^{(2)}$ measurement to no avail in a different parameter regime where a single, isolated emission line appears.

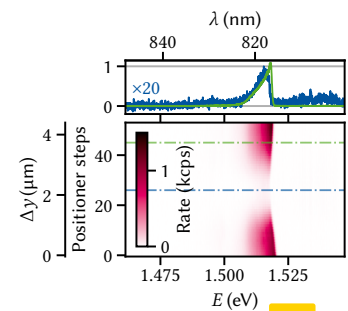


Figure 4.6: PL of the unbiased QW as the laser is stepped across a bottom gate. The line traces in the upper panel are taken at the positions indicated by dash-dotted lines. Positioner steps are converted to distance using a linear fit of the positioner readout after the initial hysteresis has worn off (about 10 steps). The Fermi edge shows a slight redshift when on top of the gate in this sample.

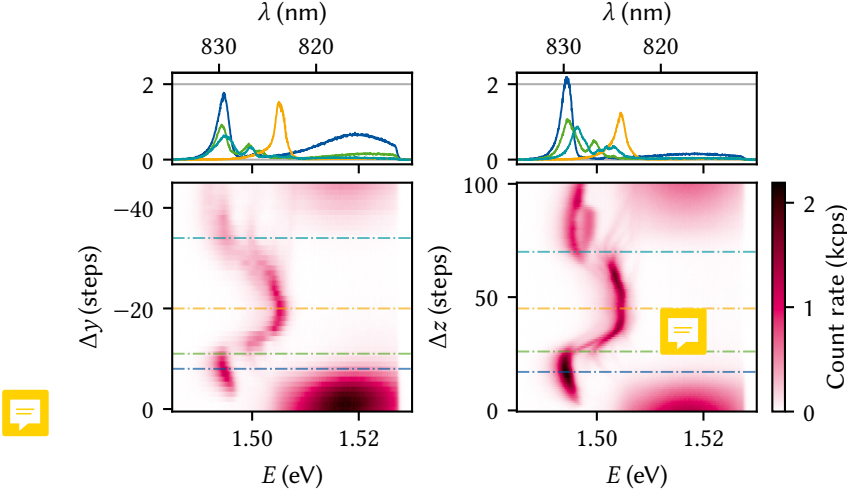


Figure 4.7: PL of a large exciton trap as function of position perpendicular (left) and parallel (right) to gravity. The trap is biased so that the emission is Stark-shifted towards lower energy. Upper panels show line cuts taken along the dash-dotted lines in the lower panels, demonstrating fairly identical behavior along both axes.

simple reflection and absorption of laser and PL radiation. I perform transfer-matrix method (TMM) simulations to explain this behavior in Section 4.3 (see also Figure 4.2). Curiously, the map also shows a shifting of the Fermi edge close to the gate. This behavior was observed consistently on this sample next to an unusual PL line shape (*cf.* Figure 4.1). The former effect could potentially be caused by band-deformation due to strain from the metallic gates.

Figure 4.7 shows two sweeps along orthogonal axes across the biased exciton trap discussed before in Figures 4.3 to 4.5. While this is not unequivocal proof of zero-dimensional confinement, it does suggest that the effective exciton potential is lowered in a laterally local fashion. The left panel of Figure 4.7 shows a scan along the in-plane axis perpendicular to gravity, while the right shows the in-plane axis parallel and against gravity. Regrettably, the resistive position readout did not yield anything but noise in these measurements, prohibiting a conversion of positioner steps into relative position as before. Both scans were acquired with the sample voltage applied to the positioners (30 V), which is the same used in Figure 4.6 as well. We can hence roughly expect 10 steps to correspond to $1\text{ }\mu\text{m}$ in y direction. Naturally, a single step against gravity displaces the sample by a smaller amount compared to the perpendicular direction, but given the circular shape of the trap and the similarity of the PL features the displayed ranges should be roughly the same. The upper panels show line cuts taken at the positions indicated by dash-dotted lines in the lower panels as usual. Both sweeps display very similar features. In the center of the trap, the Stark-shifted emission line consists of a single peak. Towards the edges, two surprising effects take place: first, the Stark shift of the dominant peak increases in magnitude, and second, a large number of additional, faint lines appear. The increase in effective electric field towards the edge of an exciton trap is reminiscent of the simulation of the same type of experiment for an undoped QW by Descamps [64, Figure 6.4], although it was not explained there. Indeed, it also appears to be in conflict with Figure 2.16 *ibid.*, where a monotonic increase in effective exciton potential as function of distance from the trap center was predicted. In the device under study here, there is of course a 2DEG whose presence towards the edge of the trap screens the voltages, in theory contributing to an attenuation of the Stark shift. Why we observe to opposite is thus quite puzzling.

The second surprising feature seen in Figure 4.7 is the addition of faint

lines that appear to branch out from the main exciton line as the laser spot is moved away from the center of the trap. These could be related to the lines observed in Figure 4.5 as well as the large number of lines required to fit the peak in Figure 4.4. If the origin of these are indeed atomic steps or islands in the QW, it makes sense that we observe them in these measurements. The Stark shift of the different lines appears depend on the position as well, indicating different coupling to the electric field and further strengthening the hypothesis that they originate from different spatial locations.



4.2 Photoluminescence excitation spectroscopy

The technique of photoluminescence excitation (PLE) can be used to gain insight into the energy level structure of optically active states [88]. While in a PL experiment we only observe the emission, PLE experiments are sensitive to absorption as well. Thus, excited states that quickly decay non-radiatively before recombining can be probed as absorption at that energy will be enhanced even though emission might not. For well-resolved PL lines, a common practice is to spectrally filter the PL radiation while sweeping the excitation laser wavelength, thus obtaining the luminescence intensity as function of excitation energy, $I_{\text{PLE}}(E_{\text{exc}}; E_{\text{det}})$, for a single detection energy E_{det} . By contrast, a PL measurement is performed at a fixed excitation energy and yields $I_{\text{PL}}(E_{\text{det}}; E_{\text{exc}})$. Alternatively, the entire PL spectrum can be integrated up to the excitation energy rather than filtered at specific energy,

$$I(E_{\text{exc}}) = \int_0^{E_{\text{exc}}} dE_{\text{det}} I(E_{\text{det}}, E_{\text{exc}}), \quad (4.7)$$

which yields a better SNR at the cost of potentially washing out selective transitions.

What do we expect for the PLE of a doped QW? By Fermi's exclusion principle, no free states are available below the Fermi level μ and thus excitation of an electron-hole pair from the valence band into the conduction band is only possible for photon energies above $E_{\text{F}}(1 + m_{\text{c}}^*/m_{\text{hh}}^*)$ (Section 2.1). Accordingly, the PLE spectrum should show an onset at that energy.²⁰ Above it, there exists a continuum of states in the QW plane, and the PLE spectrum should remain approximately constant until higher-lying states can be reached. In a single QW, these can be either higher subbands of heavy-hole valence or conduction bands or indeed light-hole transitions due to heavy-hole–light-hole mixing [130–134]. For the relatively wide QW widths in our samples, we would expect the latter to be on the order of a few meV.

Applying an external electric field should further enhance the light-hole transitions as tilting the QW breaks the symmetry forbidding light-hole transitions [135, 136]. Furthermore, the electric field depletes the 2DEG as we have seen in Figure 4.3 and should result in a laterally local potential well for excitons with discrete and approximately equidistant energy levels as laid out in Subsection 2.2.1. If such were the case, we would expect resonances in the PLE at intervals corresponding to the level spacing $\hbar\omega$ of the potential well that would confirm 0D-confinement.

20: In fact, the FES should lead to a peak at the onset of the spectrum.

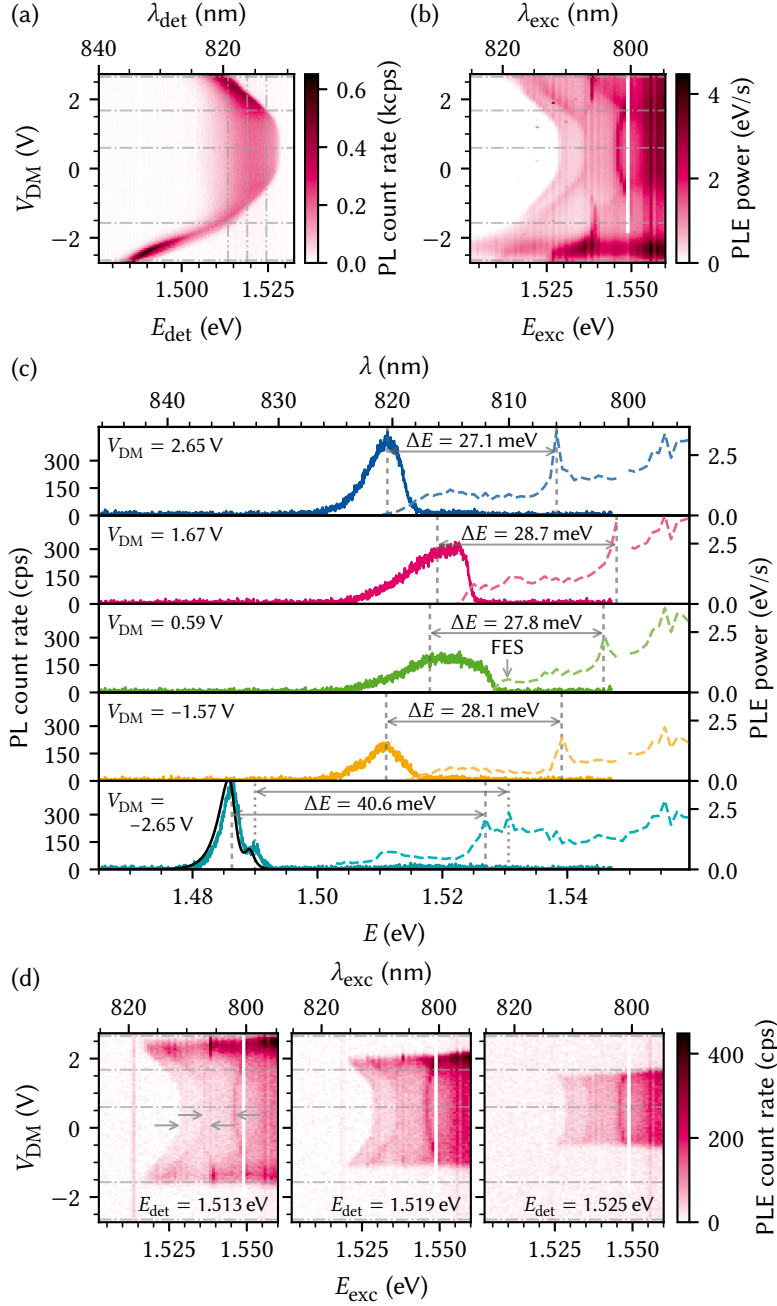


Figure 4.8: Photoluminescence excitation measurement. (a) PL map as function of difference-mode voltage for $\lambda_{exc} = 795$ nm (cf. Figure 4.3). (b) PLE map. Each column corresponds to a map like in (a) integrated up to the laser line at $E_{det} = E_{exc}$. While a 2DEG exists ($V_{DM} \in [-1.6 \text{ V}, 2.6 \text{ V}]$), absorption in PLE sets on just as emission stops in PL at the Fermi edge μ (see also Figure B.1). The Fermi edge feature is replicated at least once at approximately 10 meV above μ , while a feature with positive Stark shift $\alpha > 0$ duplicated at least once as well appears with apexes at $E_{exc} = 1.536 \text{ eV}$ and 1.546 eV . A sharp feature appears as the 2DEG is close to depletion at 1.538 eV . The vertical white bar is missing data. (c) Line cuts of the PL (a, solid lines) and PLE maps (b, dashed) taken at the horizontal dash-dotted gray lines there. At $V_{DM} = -2.65 \text{ V}$, the PL line is split by 3.7 meV which is replicated in the PLE spectrum 40.6 meV higher. The black line shows a fit to a trion and exciton following Reference 137. The features at around 1.555 eV do not shift with the voltage and are thus likely unrelated to the trap. (d) Line cuts of the entire data set at single detection energies indicated by vertical dash-dot-dotted lines in (a). Horizontal dash-dotted lines are again the positions of the line cuts shown in (c). Arrows indicate a splitting of approximately 10 meV.

Figure 4.8 shows PLE data obtained for the large exciton trap discussed previously obtained at $1 \mu\text{W}$ excitation power and $V_{CM} = -1.3 \text{ V}$, *i.e.*, similar conditions as for Figures 4.3 and 4.4. Due to the high excitation power, the measurement does not resolve the multiplet substructure observed in Figure 4.5. The top left panel (a) shows a regular PL map as function of V_{DM} at $\lambda_{exc} = 795 \text{ nm}$ and essentially reproduces the measurement of Figure 4.3. Panel (b) shows the integrated PLE following Equation 4.7. That is, the rightmost column corresponds to panel (a) integrated along E_{det} . Several interesting features are noteworthy. In line with our considerations above, the onset of PLE absorption coincides with the high-energy shoulder of the PL emission over the entire range of voltages investigated. For $V_{DM} > -1.6 \text{ V}$, the absorption edge is replicated some 10 meV higher in energy, although the splitting reduces as the carrier density is decreased. A few possible explanations for this feature

come to mind. First, the two lines could correspond to the negative trion and the neutral exciton. However, the energy difference of ~ 10 meV seems too large for the difference in binding energies, usually on the order of a few meV. Although similar features have been observed and assigned as such [138–140], the splittings in those studies were smaller while at the same time the QWs were thinner and should thus lead to larger binding energies [105, 137]. Similarly, excitons bound to impurities such as ionized donors typically show much lower energy separation to the neutral exciton [141]. A better match with the observed energy difference is the excitonic binding energy of ~ 8 meV, which would imply that the feature at higher energy would correspond to free electron-hole pairs. Alternatively, the lines could correspond to heavy- and light-hole excitons, whose splittings have been found to be on the order of 7 meV for undoped QWs of this width [134] although also smaller values have been reported [142]. The difference in electric-field dependence of the respective binding energies is hard to predict, but the Stark shift should be smaller for light-hole excitons due to their smaller effective mass and hence the narrowing of the energy splitting between the lines for higher voltages is counter-intuitive. Again, though, the presence of the 2DEG in this regime may crucially alter the physics. Finally, we can look to excited QW states as candidates. From Section 2.2, we expect subband splittings to be on the order of 50 meV for the $n_c = 1$ and $n_{hh} = 1$ transition and 8 meV for the (optically suppressed) $n_c = 0$ and $n_{hh} = 1$ transition at zero field. While the last matches fairly closely what we observe at zero field, it too should increase with increasing electric field rather than decrease. Moreover, from the calculation of the oscillator strength (Figure 2.5), we would expect the optical coupling to vanish at a certain electric field value whenever excited states are involved, which is also not observed.

So far, we have exclusively discussed the duplicated feature following the trend of the PL emission edge, but a few more observations can be made by inspecting Figure 4.8(b). Most strikingly, also in the regime of an undepleted 2DEG there is again a duplicated feature with a similar energy splitting as before, but which displays an inverted Stark shift, that is, whose energy is raised by the application of an electric field, or, more phenomenologically, a reduction in charge carrier density. We have seen such a behavior in the theoretical discussion for the first $\Delta n = 0$ excited state of the QW at low fields (Figure 2.5), but similar arguments as above can be made against such an identification. Both of the above features vanish as the 2DEG is depleted at -1.6 V and 2.6 V. In their place, a very sharp feature appears at 1.538 eV that is independent of the electric field. Going to even more negative voltage and fully depleting the 2DEG, the overall luminosity increases (as can also be seen in the PL spectrum) while broad features start to appear as function of excitation power.

Panel (c) of the figure shows line cuts taken at the voltages indicated by dash-dotted lines in panels (a) and (b) with solid lines corresponding to the emission (PL) and dashed lines to absorption (PLE). The energy shift of the two most prominent peaks in both spectra is labeled. Although not a perfect match, the shift of around 28 meV is not far off the energy of transverse optical (TO) phonons in GaAs, known in bulk to be 33 meV [143]. Similarly, the shift of 40 meV at $V_{DM} = -2.65$ V is off by approximately the same amount from the second, AlAs-like TO phonon mode in $\text{Al}_{0.32}\text{Ga}_{0.68}\text{As}$, 44 meV [125, 144, 145]. It is conceivable that the thinning of the heterostructure to a membrane modifies the phonon energies by 5 meV and it would be interesting to perform Raman spectroscopy on the membranes to investigate this further. Additionally, temperature-



dependent measurements could reveal information on the possible existence of a phonon bottleneck [146], which would show as a change in decay rate at a certain temperature corresponding to a crossover in acoustic-phonon-dominated and optical-phonon-dominated cooling of hot electrons.

The data for $V_{\text{DM}} = 0.59 \text{ V}$ show that the Stokes shift between Fermi edge of the PL emission and the FES in the PLE absorption is small, $E_{\text{S}} - E_{\text{F}} \sim 2.5 \text{ meV}$. At the largest voltage, $V_{\text{DM}} = -2.65 \text{ V}$, the PL emission splits up into a doublet peak with a splitting of 3.7 meV . The same splitting is observed between two peaks in the PLE spectrum, but shifted by $\Delta E = 40.6 \text{ meV}$ towards higher energy. These two peaks might correspond to the negative trion and neutral excitons. In fact, their PL emission is well fitted with the lineshape proposed by Esser, Zimmermann, and Runge [137], who describe the trion peak as a convolution of the exciton peak, given by a hyperbolic secant, with a thermally broadened exponential edge. The fit is drawn in black in the same panel, showing good agreement with the data, and yielding $E_{\text{T}} = 1.487 \text{ eV}$, $E_{\text{X}} = 1.490 \text{ eV}$, a linewidth of $\Gamma = 770 \mu\text{eV}$, and a temperature of $T = 1.2 \text{ K}$. The temperature, while hot compared to the lattice temperature, matches fairly well with the temperature obtained from the Fermi edge (Section 4.1). The fact that the peak splits into a doublet structure here whereas it did not in the measurement of Figure 4.3 might be explained by slightly different focal spot positions. Lastly, panel (d) shows line cuts of the data taken at a single detection energy, $I_{\text{PLE}}(E_{\text{exc}}; E_{\text{det}})$, corresponding to the positions indicated by vertical dash-dot-dotted lines in panel (a). The parabolic features discussed previously are clearly not an artefact of integrating over the entire PL spectrum.

To summarize the PLE measurement, several features that systematically shift with the electric field generated by the difference-mode voltage V_{DM} have been observed. However, the data show no indication of an in-plane level splitting arising from confinement, although the resolution in E_{exc} is also likely too low for this large a trap size. Interpolating the harmonic potential found by Descamps [64] for a smaller trap to this trap geometry,²¹ a level splitting of $\Delta E = 2\hbar\omega = 40 \mu\text{eV}$ would be expected (see Subsection 2.2.1), which is far below the linewidth of the exciton of $770 \mu\text{eV}$. I put forth several alternative hypotheses for the origin of the various features, although none match quite precisely with values expected from the literature.

21: For a diameter of 200 nm , $\omega = 738 \text{ GHz}$, and therefore we can interpolate $\omega = 18.5 \text{ GHz}$ for a diameter of $5 \mu\text{m}$ because both ω and ρ enter the potential quadratically.

4.3 Transfer-matrix method simulations of the heterostructure membrane

In the previous sections, we have seen that there is a profound difference in the PL intensity emitted from the sample depending on if there is a semi-transparent metallic gate electrode fabricated on either side of the membrane or not. What is more, Figure 4.2 showed that this reduction is in fact, counterintuitively, more pronounced for gates on the backside of the membrane. In the following, I explain this behavior as a consequence of thin-film interference effects. To this end, I perform TMM simulations of the heterostructure membranes investigated in this part of the present thesis using the PyMoosh package [147] to elucidate the observed quenching of PL when illuminating gate electrodes as well as the overall optical efficiency.²² The TMM is a computationally efficient method of computing the amplitude of in- and outgoing electric fields in layered structures.



22: Strictly speaking, the term TMM only refers to one of the several formalisms implemented in the PyMoosh package. While fast, it is not the most numerically stable, and other methods may be preferred if wall time is not a limiting issue.

I will first briefly recap the simulation method following Reference 147. For more details, refer to *ibid.* and references therein.

4.3.1 Electric fields in layered thin films

Consider a layered structure along z with interfaces at $z_i, i \in \{0, 1, \dots, N+1\}$ that is translationally invariant along x and y . Each layer i may consist of a different dielectric material characterized by a (complex) relative permittivity $\epsilon_{r,i}$.²³ The electric field component along y of an electromagnetic wave transverse electric (TE) mode originating in some far away point satisfies the Helmholtz equation

$$\frac{\partial^2 E_y}{\partial z^2} + \gamma_i^2 E_y = 0, \quad (4.8)$$

where $\gamma_i = \sqrt{\epsilon_{r,i} k_0^2 - k_x^2}$ with $k_0 = \omega/c$ the wave vector in vacuum and k_x the component along x . In layer i of the structure, the solution to Equation 4.8 may be written as a superposition of plane waves incident and reflected on the lower and upper interfaces [147],

$$\begin{cases} E_{y,i}(z) = A_i^+ \exp\{i\gamma_i[z - z_i]\} + B_i^+ \exp\{-i\gamma_i[z - z_i]\}, \\ E_{y,i}(z) = A_i^- \exp\{i\gamma_i[z - z_{i+1}]\} + B_i^- \exp\{-i\gamma_i[z - z_{i+1}]\}, \end{cases} \quad (4.9)$$

where the coefficients with superscript $+$ ($-$) are referenced to the phase at the upper (lower) interface, respectively. Matching these solutions at $z = z_i$ for all i to satisfy the interface conditions imposed by Maxwell's equations gives rise to a linear system of equations, the solution to which can be obtained through several different methods.

A particularly simple method is the transfer-matrix method (T -matrix formalism), which corresponds to writing the interface conditions at $z = z_i$ as the matrix equation

$$\begin{pmatrix} A_{i+1}^+ \\ B_{i+1}^+ \end{pmatrix} = T_{i,i+1} \begin{pmatrix} A_i^- \\ B_i^- \end{pmatrix} \quad (4.10)$$

with

$$T_{i,i+1} = \frac{1}{2\gamma_{i+1}} \begin{pmatrix} \gamma_i + \gamma_{i+1} & \gamma_i - \gamma_{i+1} \\ \gamma_i - \gamma_{i+1} & \gamma_i + \gamma_{i+1} \end{pmatrix} \quad (4.11)$$

the transfer matrix for interface i . Connecting the coefficients for adjacent interfaces within a layer of height $h_i = z_{i+1} - z_i$ requires propagating the phase,

$$\begin{pmatrix} A_i^- \\ B_i^- \end{pmatrix} = C_i \begin{pmatrix} A_i^+ \\ B_i^+ \end{pmatrix}, \quad (4.12)$$

with

$$C_i = \exp\{\text{diag}(-i\gamma_i h_i, i\gamma_i h_i)\}. \quad (4.13)$$

Iterating Equations 4.11 and 4.13, the total transfer matrix $T = T_{0,N+1}$ then reduces to the matrix product

$$T = T_{N,N+1} \prod_{i=0}^{N-1} T_{i,i+1} C_i. \quad (4.14)$$

From T , the reflection and transmission coefficients can be obtained as $r = A_0^- = -T_{01}/T_{00}$ and $t = B_{N+1}^+ = rT_{10} + T_{11}$. Taking the absolute value square of reflection and transmission coefficients then yields the reflectance \mathcal{R} and the transmittance \mathcal{T} , which correspond to the fraction

23: We disregard magnetic materials with relative permeability $\mu_r \neq 1$ for simplicity.

of total incident power being reflected and transmitted, respectively. To obtain the absorptance \mathcal{A} , the fraction of power being absorbed, in layer i , one can compute the difference of the z -components of the Poynting vectors (cf. ??) at the top of layers i and $i + 1$. In the TE case considered here, ?? reduces to [147]

$$S_i = \text{Re} \left[\frac{\gamma_i^*}{\gamma_0} (A_i^+ - B_i^+) (A_i^+ + B_i^+) \right] \quad (4.15)$$

and is hence straightforward to extract from the calculation of either the S or T matrices.

Equation 4.14 is simple to evaluate on a computer, making this method attractive for numerical applications. However, the opposite signs in the argument of the exponentials in Equation 4.13 can lead to instabilities for evanescent waves ($\gamma_i \in \mathbb{C}$) due to finite-precision floating point arithmetic [148]. Rewriting Equation 4.11 to have incoming and outgoing fields on opposite sides of the equality alleviates this issue while sacrificing the simple matrix-multiplication composition rule in what is known as the scattering matrix (S -matrix) formalism. Finally, note that for a thorough accounting of in- and out-going field amplitudes, excitonic effects should be included, for example using the approach by D'Andrea and Del Sole [149].

Beyond the calculation of the aforementioned coefficients, the TMM formalism also allows to compute the full spatial dependence of the fields. Two cases are implemented in PyMoosh: irradiation of the layered structured with a Gaussian beam rather than plane waves of infinite extent, and a current line source inside the structure. In the first case, the previously assumed translational invariance along x leading to a plane-wave spatial dependence is replaced by a superposition of plane waves weighted with a normally distributed amplitude,²⁴

$$E_{y,i}(x, z) = \exp(ik_x x) \rightarrow \int \frac{dk_x}{2\pi} \mathcal{E}_0(k_x) E_{y,i}(k_x, z) \exp(ik_x x), \quad (4.16)$$

with (cf. ??)

$$\mathcal{E}_0(k_x) = \frac{w_0}{2\sqrt{\pi}} \exp \left\{ -ik_x x_0 - \left[\frac{w_0 k_x}{2} \right]^2 \right\} \quad (4.17)$$

and

$$E_{y,i}(k_x, z) = A_i^- \exp\{i\gamma_i(k_x)[z - z_{i+1}]\} + B_i^+ \exp\{-i\gamma_i(k_x)[z - z_i]\}, \quad (4.18)$$

and where we considered only normal incidence for simplicity.

In the second case, Langevin et al. [147] consider an AC current I flowing through a translationally invariant, one-dimensional wire along y at $x = x_s$. This introduces a source term into the Helmholtz equation, Equation 4.8, which, upon Fourier transforming in x direction, leads to

$$\frac{\partial^2 \hat{E}_y}{\partial z^2} + \gamma_i^2 \hat{E}_y = -i\omega\mu_0 I \delta(z) \exp(ik_x x_s). \quad (4.19)$$

The electric field $\hat{E}_{y,i}(k_x, z)$ is thus proportional to the Green's function of Equation 4.19 and can be obtained using a similar procedure as in the case of a distant source incident on the structure by matching the interface conditions. Performing the inverse Fourier transform by means of Equation 4.16 with constant weights, $\mathcal{E}_0(k_x) \equiv 1$, then yields the two-dimensional spatial distribution of the electric field, $E_{y,i}(x, z)$.



24: I.e., the inverse Fourier transform of $\mathcal{E}_0(k_x) E_{y,i}(k_x, z)$.

4.3.2 Quantum well absorptance

We now turn to applying the methods laid out above as implemented in PyMoosh to the membranes under investigation in the present thesis. For the simulations, I considered a membrane of 10/90/20/90/10 nm thick layers of GaAs/Al_{0.34}Ga_{0.66}As/GaAs/Al_{0.34}Ga_{0.66}As/GaAs at zero temperature, $\lambda_0 = 825$ nm, and normal incidence. The material parameters were obtained from References 150, 151, and 152 through PyMoosh's interface to the `refractiveindex.info` database [153]. In the main text I take the half-space below the membrane to be the epoxy resin used to glue the sample to the Silicon host chip, which I assume to have a refractive index of $n_{\text{epo}} = 1.55 + 0i$,²⁵ corresponding to there being no coherent back-scattering at the interface between epoxy and Silicon host chip. I discuss the influence a finite epoxy thickness in Appendix A. I then consider four different scenarios,

1. The bare heterostructure,
2. The heterostructure with only a top gate consisting of 7/2 nm of Au/Ti,
3. The heterostructure with only a bottom gate consisting of 25/5 nm of Au/Ti,
4. The heterostructure with both bottom and top gate with the aforementioned thicknesses,

and compute the absorptance \mathcal{A} in the QW layer and reflectance \mathcal{R} at the respective topmost layer. Both of these parameters will influence the amount of PL collected for a given excitation power. Obviously, the more of the incident laser light is reflected, the less can be absorbed, and the less is absorbed the less can be radiatively emitted. Table 4.1 presents the results of the simulation, which confirms the behavior observed in the experiment: the presence of a gate on the backside of the membrane is the most significant factor in the reduction of incident power being absorbed in the QW despite the fact there is no additional obstructions in the light's path before the QW, highlighting the importance of multilayer effects.

The reason for this lies in the relatively high reflectivity ($\mathcal{R} \sim 75\%$ for GaAs/Ti/Au) of the bottom gate stack. Since furthermore the effective wavelength in GaAs is $\lambda = \lambda_0/n \sim 230$ nm, the structure actually resembles a resonant cavity for which the electric field mode has a node in the center of the cavity, *i.e.*, the QW, and thus the absorption is strongly reduced. In turn, this means that changing the thickness of the membrane we can change the resonance condition of the cavity such that the electric field has a peak or trough at the QW position, maximizing the coupling matrix element leading to absorption. As the width of the QW determines the optical properties, the AlGaAs barrier thickness remains as the only parameter we can reasonably vary. *Reducing* the thickness, however, is ill-advised as it decreases the mobility in the QW due to enhanced scattering and further increases the probability of tunneling through the barrier. I therefore used PyMoosh to optimize QW absorptance over the barrier thickness of a double-gated structure at $\lambda_0 825$ nm with the unoptimized case of 90 nm as a lower bound.

25: Epotek 353ND

Table 4.1: Absorptance \mathcal{A} and reflectance \mathcal{R} in the QW for different configurations of the heterostructure. "Bare" is the standard structure without gate electrodes. "TG" and "BG" are with a gate on either the top or bottom side. "TG+BG" is with gates on both sides as on a trap site.

	\mathcal{A} (%)	\mathcal{R} (%)
Bare	2.9	22.4
TG	1.8	42.0
BG	0.5	82.7
TG+BG	0.4	84.8



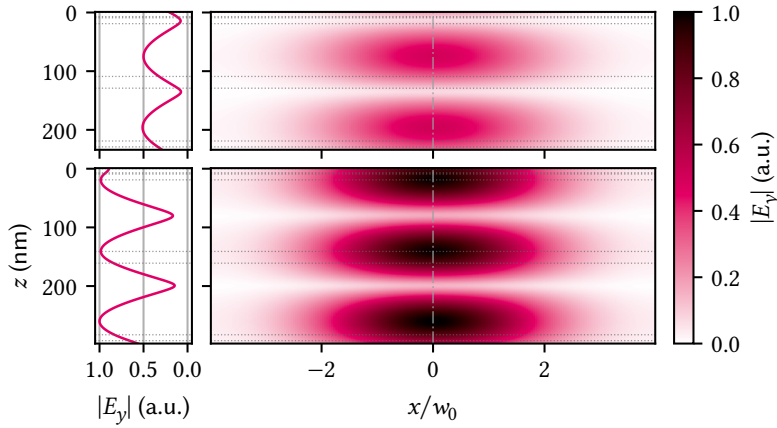


Figure 4.10 depicts the absorptance at the optimal barrier thickness of 122 nm as function of incident wavelength λ_0 . \mathcal{A} is enhanced by a factor of up to 16 over a broad wavelength range compared to the unoptimized case. The resulting barrier thickness is only moderately larger than before and should still be thin enough to allow for sufficiently strong electric fields at moderate voltages. The electric field distribution inside the membrane for illumination by a Gaussian beam with waist radius $w_0 = 624$ nm (Part II) computed according to Equation 4.16 is shown in Figure 4.9 for the (un)optimized case in the (top) bottom panels. The left panels show a line cut taken at $x = 0$. As argued qualitatively above, in the case of a thinner barrier, the field displays a node at the QW position indicated by dashed lines at a depth of $z = 100$ and 120 nm. Conversely, the situation is reversed for the 30 nm thicker barrier, which hosts a field maximum at the depth of the QW.

4.3.3 Field emission

So far, we have considered the absorption of the incident laser radiation in the QW, a situation akin to placing the light source outside above the simulated structure. To see how multilayer interference affects the extraction of light emitted *inside* the structure, we turn to the Green's function calculation of Equation 4.19. That is, we place an infinitely long and in the xz plane point-like current line in the center of the QW to model the radiation emitted from a dipole. Evidently, this is an approximation as the solution will have the same cylindrical symmetry as the source, whereas a more realistic model would contain a point-dipole producing a field distribution as described in ?? . Nonetheless, in the plane of the point-dipole, the field should be well approximated by that of an infinitely long current line. We once again use PyMoosh to perform the simulation.

Figure 4.11 shows the real part of the electric field for two different geometries: the bare heterostructure (left column) and the double-gated structure (right column). The source is indicated by a black dot and interfaces between different materials by dotted lines. The top row shows the results for the unoptimized barrier thickness, where clearly the presence of the gates attenuates the outcoupling from the membrane into the air halfspace above ($z < 0$). For the unoptimized, bare structure the

Figure 4.9: Absolute value of the electric field inside the double-gated heterostructure under illumination with a Gaussian beam at $\lambda_0 = 825$ nm from the top. Top (bottom) panels show the structure with the default (optimized) barrier thickness of 90 nm (122 nm), respectively. Dotted horizontal lines indicate interfaces between different materials while the vertical dash-dotted line indicates the position of the line cuts shown in the left column. Increasing the thickness of the barrier has two beneficial effects; first, the overall field intensity inside the structure is higher by a factor of two, and second, there is a peak rather than a knot in the QW at a depth of ~ 120 nm (~ 150 nm), leading to enhanced absorption.

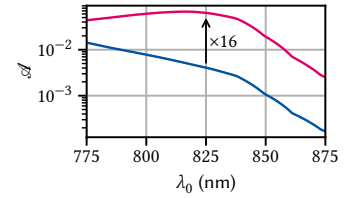


Figure 4.10: QW absorptance \mathcal{A} in a heterostructure with default (blue) and optimized (magenta) barrier thickness and top and bottom gates as function of wavelength. Optimization was performed at 825 nm using the differential evolution algorithm implemented in PyMoosh, resulting in a barrier thickness of 122 nm and an absorptance better by a factor of 16 at 6.3 %.

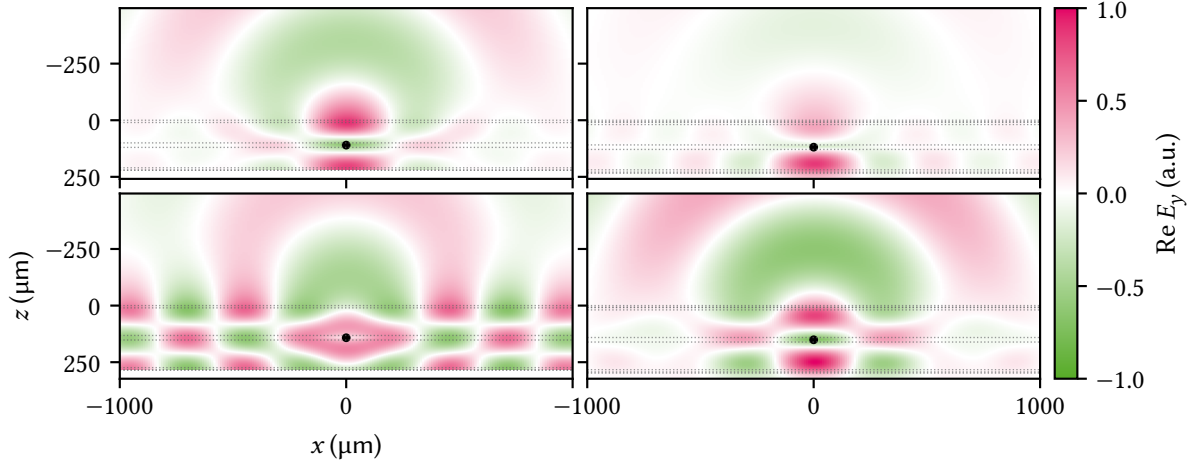


Figure 4.11: Real part of the electric field emitted by a current line located in the QW (black point) for different cases of the unoptimized (top row) and optimized (bottom row) structures. Left column shows the bare structures, right the double-gated ones. The half space $z < 0$ is the air above the membrane in the direction of the objective lens and the dotted lines indicate interfaces between materials. Evidently, the gates reduce the amplitude in the upper half of the membrane and thereby the outcoupling efficiency compared to the bare structure, consistent with what is observed in the experiment. Optimizing the barrier thickness for absorption in the QW drastically improves the outcoupling efficiency into the halfspace $z < 0$ for both the bare and gated structures, although actually the latter (bottom right panel) radiates more power into the surface normal direction when compared with the ungated structure (bottom left).

emission pattern is close to cylindrical as would be the case in a homogeneous medium. Increasing the barrier thickness (bottom left panel) in this case results in a complicated standing-wave pattern inside the membrane. When adding the gates on both sides (bottom right panel), an emission pattern close to that of the unoptimized, bare structure is recovered, albeit with a higher extraction efficiency from the membrane.

These results demonstrate that on top of increasing the absorption efficiency, the extraction efficiency of PL radiation from inside the membrane is further enhanced when increasing the AlGaAs barrier thickness by a modest 32 nm, leading us to expect an improvement larger than 16-fold in the end-to-end optical efficiency of PL experiments.

In this part of the present thesis, I presented and discussed optical measurements of doped semiconductor membranes under perpendicular electric fields. I first gave an introduction to the physics of photoluminescence (PL) in semiconductor QWs in Chapter 2. Starting with the PL of an unbiased 2DEG in a QW, which is defined by the band gap and the Fermi edge at low and high energies, respectively, I then performed calculations of the electron and hole energies in an undoped QW under the influence of an external electric field. This gives rise to the QCSE and quadratically lowers the energy difference between electron and hole ground states. The QW confinement prevents the field ionization of excitons and instead leads to a continuously decreased wave function overlap resulting in enhanced lifetime and reduced oscillator strength. I showed that, when taking into account lateral confinement by application of a local electric field as envisaged by Descamps [64], the oscillator strength vanishes for finite orbital angular momentum quantum numbers under the assumption of rotational symmetry, resulting in an optically resolvable level splitting of $2\hbar\omega$. Furthermore, the model predicts that the oscillator strength of excited states vanishes at certain electric fields because their wave functions have nodes in the QW. Using simple approximations, I finally estimated the Fowler-Nordheim tunneling rate of charge carriers escaping the QW confinement as function of the electric field, finding that below 5 V/nm rates are below 1 MHz. In the analytical calculations, I neglected excitonic effects, which for quantitative results need to be considered. Furthermore, the samples investigated later on in this part of the present thesis all contained a doped QW hosting a 2DEG whose presence certainly alters the picture. Many-body theory is required to fully capture the arising effects such as the FES and Mahan excitons [83].

In Chapter 3, I introduced the `mjolnir` measurement framework that facilitates optical experiments in the Millikelvin confocal microscope presented in Part II. I made the case for its existence and outlined the design goals before sketching the package's implementation and features. Central to these is the abstraction of physical instruments into logical ones, combining the parameters of different devices into logical functionality. Because of the relatively large range of different devices used to control the optical setup, this significantly reduces the level of complexity exposed to the user during the measurement workflow and enables the concise definition of measurements without large amounts of repetitive setup and teardown code. A very simple example is the `ExcitationPath` instrument's `wavelength` parameter, which not only sets the wavelength of the cw laser but also adjusts the `wavelength` parameter of the power meter, thus ensuring the sensor reading is correctly converted. Furthermore, the package implements multiple calibration routines, for instance to automatically update the energy axis of the CCD mounted after the spectrometer. Measurements are implemented as multi-dimensional loops defined by composable `Sweep` objects and run through a central `MeasurementHandler` object that can be customized to execute default setup and teardown tasks as well as perform standard modifications of measurement definitions. Finally, `mjolnir` provides live plotting of power meter readings, CCD data, or APD count rate, as well as an interactive data plotter based on 2D-slices through multidimensional data. Since the rest of the package is independent of the measurement functionality, other QCoDeS-

based measurement frameworks such as quantify can readily replace or augment the latter, for instance to benefit from more sophisticated measurement control workflows that include timing control flows and broader support for buffered sweeps, or leverage the data analysis capabilities.

Employing the *mjolnir* software framework, I conducted optical measurements of doped QW membranes that I presented in Chapter 4. With the aim of demonstrating the spatial 0D-confinement of excitons by electrostatic means, I characterized the PL as function of position and electric field applied by means of local gate electrodes on the top and bottom sides of the membrane. The 2DEG PL of the unbiased QW was found to be in good agreement with the intuition obtained in Chapter 2, although it also revealed a significant mismatch between nominal and actual charge carrier densities for multiple samples. Defining the difference-mode (V_{DM}) and common-mode (V_{CM}) voltages as the difference and sum of top and bottom gate voltages, respectively, the electric field across the membrane is expected to be proportional to V_{DM} . In most samples investigated, the QCSE was not symmetric in V_{DM} , however, but showed an offset of around 700 mV, corresponding to an admixture of V_{CM} , that can be explained by built-in screening on one side of the membrane, the origin of which is unknown. Updating the virtual gate matrix to compensate for this effect (Equation 4.4) in future measurements would simplify their interpretation.

For small V_{DM} , the field inside the QW is entirely screened by the 2DEG. Surprisingly, though, at about ± 1 V from the symmetry point, the charge carrier density starts to reduce until the 2DEG is fully depleted at about the same amount higher voltages again. I proposed that this is due to carrier sweep-out by Fowler-Nordheim tunneling that establishes an equilibrium between ionized dopants in the AlGaAs barrier and the charge carriers in the well. As the electric field is increased, the tunnel coupling increases and more ionized donors neutralize with electrons from the QW. This reduces the band bending, in turn broadens the tunnel barrier, and hence counteracts the increased transparency due to the tilting of the bands by the electric field. Overall, the emission energy could be tuned by 20 meV in the fully depleted regime.

Measuring the power dependence of the Stark-shifted emission line revealed no biexciton peaks. Instead, a substructure of a considerable number of individual lines appeared. At very small excitation powers, the main emission line displayed a logarithmic blue shift whose strength drastically changes above 10 nW. Several exciton traps showed an intricate substructure of the main emission line, whose constituents coupled differently to the electric field. As one-dimensional position sweeps across a trap also showed, the most likely explanation are a number of different emitters at different spatial locations within the area covered by the microscope focus. Possible candidates are impurities, defects, or interface steps or islands. While the literature has shown these to also be capable of binding excitons, no signatures of confinement were observed in $g^{(2)}$ measurements.

Such could also be revealed by photoluminescence excitation (PLE), a measurement of which I presented in Section 4.2. While the trap diameter was large and the expected orbital splitting of an excitonic quantum dot quite small and not observed, several interesting features appeared nonetheless. I put forth several hypotheses for the origin of the duplicated absorption edge as well as a second duplicated feature with positive Stark shift. Among them were light-hole excitons, excited QW states,

and optical phonons, although none yield a quantitative agreement with the literature. For the largest electric field, where the 2DEG is fully depleted, both the PL and PLE displayed a peak splitting of the same magnitude, ~ 3 meV but 40 meV apart. The PL line was well fitted by a trion and exciton line shape. In the regime of finite electron densities it might be interesting to investigate if trion-polaritons occur in this system [154–156].

Finally, I addressed the observed quenching of PL intensity when the microscope focus is moved on top of gates on the backside of the membrane. I appealed to multilayer interference effects that lead to a reduction in both absorption of irradiant photons in the QW as well as in outcoupling efficiency. Using the transfer-matrix method (TMM), I simulated the membrane heterostructure for different configurations of gates on either sides and found good qualitative agreement with the behavior observed in experiments. I then optimized the AlGaAs barrier thickness for higher absorptance and, based on this, proposed increasing the current thickness of 90 nm by a modest 30 nm to achieve a 16-fold improved absorptance and better outcoupling efficiency.

Ultimately, though, I did not observe signatures of exciton confinement by local electrostatic potentials, which would be a significant step towards the realization of a spin-photon interface to semiconductor spin qubits by top-down fabrication. Where does this leave the concept introduced by Descamps [64]? Firstly, none of the samples that I investigated were fully functional, and as such we cannot make any definitive statements about the feasibility of the concept. Indeed, we can take the opposite point of view: none of the measurements presented in the present thesis provide any negative evidence that would *prohibit* electrostatic exciton trapping as envisioned in Reference 64. All observed deviations from the expected behavior should be possible to resolve by improved sample growth in close feedback with experimental characterization. Access to the full parameter space of virtual difference-mode and common-mode voltages of a sufficiently small central gate pair surrounded by a larger guard gate can reasonably be expected to provide enough tunability to confine single excitons. Given the above, the guard common mode should be used to overcome the screening and deplete the 2DEG. Then, the central difference mode should have a large enough window of operation before the Schottky barrier breaks down ($V_{DM} \approx \pm 1.4$ V) to provide a localized electric field that, going by the calculations in Chapter 2, lowers the exciton energy by up to 25 meV, and results in a quantum dot orbital level splitting on the order of 0.5 meV, large enough to be resolved by PLE. The optimization of the heterostructure design I proposed should furthermore provide higher radiative efficiency and thus allow measurements over a wider range of excitation powers while only modestly lowering the achievable electric field for a given voltage. To enable resonance-fluorescence (RF) measurements, the coherence of excitation and subsequent emission under the current polarization configuration of the confocal microscope should be investigated (see ??).

Moving beyond GaAs, Reznikov [78] proposed an implementation of the device concept in another material system, Ge/Si_{1-x}Ge_x. Hole spin qubits in this system have quickly matured in recent years. What is more, by carefully engineering the alloy composition and strain of the QW, a semi-direct¹ bandgap as well as type-I confinement² is projected to be achievable. Favorably, the optical gap can be tuned to the telecom O-band and thus alleviate the need for quantum frequency conversion to match quantum network operation wavelengths. However, the optical characteriza-

1: *I.e.*, the band structure has conduction and valence band minima and maxima at the Γ -point, but the Γ -valley is not the lowest conduction band valley.

2: *I.e.*, the band alignment of the valence band is inverted compared to the conduction band and both electrons and holes are confined in the QW.

tion of this system will be challenging as the quasi-direct band gap leads to reduced PL efficiency due to valley coupling.

Acknowledgements An overview of wafers measured in this part of the present thesis is given in Table B.1. Nikolai Spitzer^a grew wafer #15460 (“HONEY”). Julian Ritzmann^a grew wafer #15271 (“FIG”). Chao Zhao^b grew wafer #M1_05_49. Thomas Descamps fabricated the sample DOPED M1_05_49-2. Sebastian Kindel fabricated the samples HONEY H13 and FIG F10.

a: Ruhr-Universität Bochum.

b: Then at Forschungszentrum Jülich.

Part IV

A FILTER-FUNCTION FORMALISM FOR UNITAL QUANTUM OPERATIONS

APPENDIX

Dependence of TMM simulations on epoxy thickness



In Section 4.3, I carried out transfer-matrix method (TMM) simulations of the membrane structure to elucidate the quenching of photoluminescence (PL) intensity when focusing the laser on gates on the top or bottom side of the membrane. There, I assumed incoherent scattering of photons at the epoxy/Si interface below the membrane. This assumption is based on the fact that Descamps [64] found the epoxy thickness, on the order of a few μm , to vary significantly across the chip. If the variation is fast enough, we can expect the phase of back-scattered photons to average out and hence destroy coherence. Nonetheless, we should estimate the influence of coherent back-scattering. Figure A.1 shows the reflectance \mathcal{R} and QW absorptance \mathcal{A} as function of the epoxy thickness. The dashed line indicates the value resulting from the incoherent simulation. Both quantities vary significantly with the epoxy thickness, but the incoherent values \mathcal{A}_∞ and \mathcal{R}_∞ are close to the average. From the fact that neither the PL nor the reflected laser intensity varies spatially by such large amounts in experiments, we can conclude that either the thickness variation is small enough to not play a significant role or that it varies fast enough to validate the assumption of incoherent back-scattering.

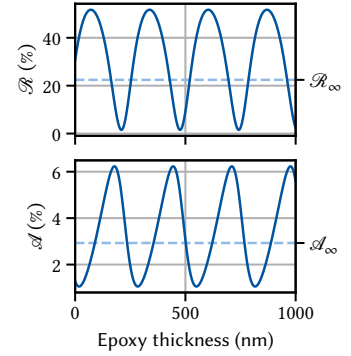


Figure A.1: Reflectance (top) and quantum well (QW) absorptance (bottom) as function of epoxy thickness assuming coherent back-scattering. The period corresponds to the wavelength in epoxy, $\lambda_{\text{epo}} = \lambda_0/n_{\text{epo}}$.

Additional measurements

In this appendix, I give additional information on simulation parameters and show further measurements.

B.1 Self-consistent Poisson-Schrödinger simulation of the membrane band structure

The samples studied in Chapter 4 were all grown using molecular beam epitaxy (MBE) and had similar nominal designs. To compare the design charge carrier density with the measurements obtained from PL of the Fermi edge, I simulated the band structure using a self-consistent Poisson-Schrödinger solver [116]. Table B.1 shows the nominal doping concentration N_d as well as the charge carrier density in the QW, n , obtained from a simulation using the parameters given in Table B.2.

Table B.1: Heterostructure parameters used in the present thesis. The doping density N_d is nominal, whereas the charge carrier density in the QW, n , is computed using the nominal doping values with parameters given in Table B.2.

WAFER	N_d (cm ⁻³)	n (cm ⁻²)
M1_05_49	6.5×10^{17}	1.95×10^{11}
15460 (HONEY)	1.8×10^{18}	4.26×10^{11}
15271 (FIG)	8.0×10^{17}	3.91×10^{11}

B.2 Additional data

B.2.1 Combined plot of PL and PLE data

In Section 4.2, I showed PLE measurements of a large exciton trap. When integrating the PL spectrum over the detection energy, the data showed several distinct features including an onset of the absorption that depends on the electric field applied by the difference-mode voltage V_{DM} . Figure B.1 shows the same data as panels (a) and (b) of Figure 4.8, but drawn in the same plot. It is clear that the onset of absorption occurs just as the PL emission drops off, indicating a small Stokes shift.

Table B.2: Simulation parameters used to compute the charge carrier density n in Table B.1.

PARAMETER	VALUE	UNIT
E_{DX}^a	-71.5	meV
ΔE_c^b	240	meV
m_c	0.067	m_e
Δz	0.5	nm
T	10	mK
V_{FP}^c	0.76	V

^a Energy of the DX-center below the Fermi level.

^b Conduction band offset at the GaAs/Al-GaAs interface.

^c Fermi level pinning voltage.

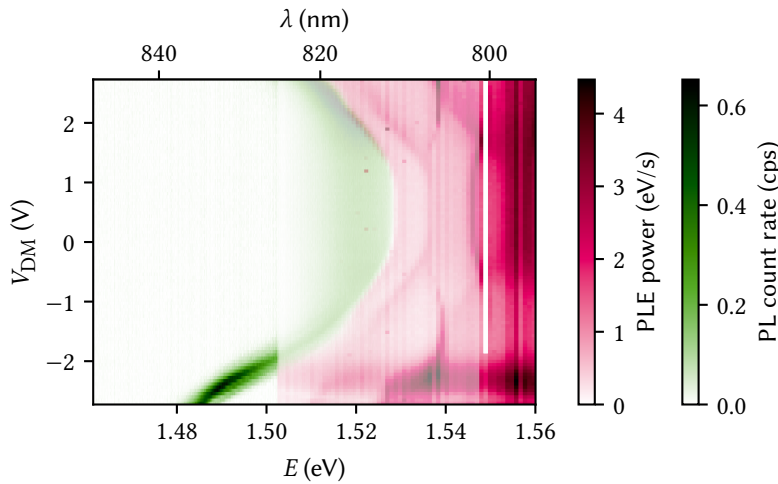


Figure B.1: Combined plot of the PL with excitation at 795 nm (green) and photoluminescence excitation (PLE) (magenta). The data overlap in the range of 801 nm to 825 nm, where they are plotted with 50 % transparency. The onset of the absorption edge in PLE coincides with the high-energy shoulder of the PL emission.

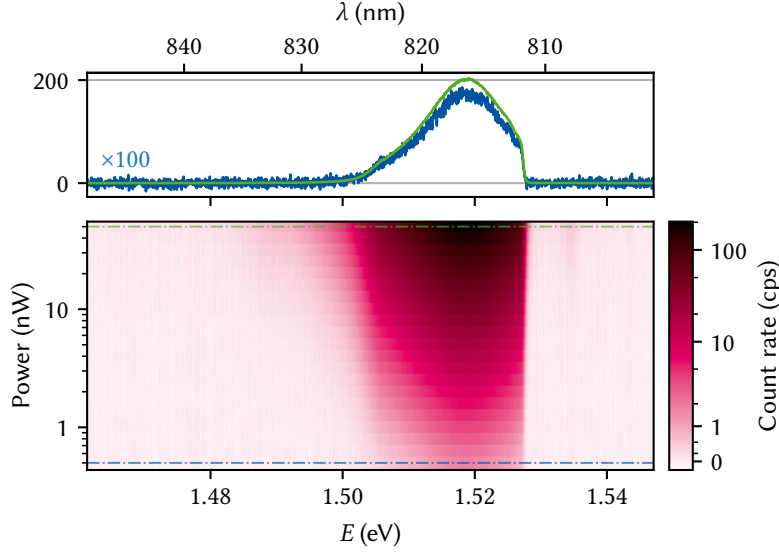


Figure B.2: Two-dimensional electron gas (2DEG) PL of an unbiased QW as function of excitation power. The Fermi edge at 1.5275 eV does not broaden over two orders of magnitude as the line cuts in the upper panels also show.

B.2.2 2DEG PL as function of power

In Section 4.1, it was determined that the electrons recombining from the Fermi edge of the 2DEG were much hotter at ~ 1 K than the cryostat temperature at ~ 10 mK. The fit to the trion-exciton lineshape in Section 4.2 yielded similar results. Figure B.2 demonstrates that this is not a local heating of the lattice due to excess laser power. Shown is the 2DEG PL as function of excitation power from 5 nW to 500 nW, with the upper panel showing line cuts at highest and lowest power. There is no discernible broadening in the Fermi edge on the high-energy side of the spectrum.

Bibliography

- [1] Michael A. Nielsen and Isaac L. Chuang. *Quantum Computation and Quantum Information: 10th Anniversary Edition*. 10th ed. Cambridge University Press, 2011 (cited on page 4).
- [2] Christoph Simon. “Towards a Global Quantum Network.” In: *Nature Photonics* 11.11 (11 Nov. 2017), pp. 678–680. doi: [10.1038/s41566-017-0032-0](https://doi.org/10.1038/s41566-017-0032-0) (cited on page 4).
- [3] H. J. Kimble. “The Quantum Internet.” In: *Nature* 453.7198 (7198 June 2008), pp. 1023–1030. doi: [10.1038/nature07127](https://doi.org/10.1038/nature07127) (cited on page 4).
- [4] C H Bennett and G Brassard. “Quantum Cryptography: Public Key Distribution and Coin Tossing.” In: International Conference on Computers, Systems & Signal Processing. Vol. 1. Bangalore, India, Dec. 1984, pp. 175–179. doi: [10.1016/j.tcs.2014.05.025](https://doi.org/10.1016/j.tcs.2014.05.025) (cited on page 4).
- [5] Artur K. Ekert. “Quantum Cryptography Based on Bell’s Theorem.” In: *Physical Review Letters* 67.6 (Aug. 5, 1991), pp. 661–663. doi: [10.1103/PhysRevLett.67.661](https://doi.org/10.1103/PhysRevLett.67.661) (cited on page 4).
- [6] David Deutsch et al. “Quantum Privacy Amplification and the Security of Quantum Cryptography over Noisy Channels.” In: *Physical Review Letters* 77.13 (Sept. 23, 1996), pp. 2818–2821. doi: [10.1103/PhysRevLett.77.2818](https://doi.org/10.1103/PhysRevLett.77.2818) (cited on page 4).
- [7] Nicolas Gisin et al. “Quantum Cryptography.” In: *Reviews of Modern Physics* 74.1 (Mar. 8, 2002), pp. 145–195. doi: [10.1103/RevModPhys.74.145](https://doi.org/10.1103/RevModPhys.74.145) (cited on page 4).
- [8] Anqi Huang et al. “Implementation Vulnerabilities in General Quantum Cryptography.” In: *New Journal of Physics* 20.10 (Oct. 2018), p. 103016. doi: [10.1088/1367-2630/aade06](https://doi.org/10.1088/1367-2630/aade06) (cited on page 4).
- [9] Xiao-Ling Pang et al. “Hacking Quantum Key Distribution via Injection Locking.” In: *Physical Review Applied* 13.3 (Mar. 3, 2020), p. 034008. doi: [10.1103/PhysRevApplied.13.034008](https://doi.org/10.1103/PhysRevApplied.13.034008) (cited on page 4).
- [10] J. I. Cirac et al. “Distributed Quantum Computation over Noisy Channels.” In: *Physical Review A* 59.6 (June 1, 1999), pp. 4249–4254. doi: [10.1103/PhysRevA.59.4249](https://doi.org/10.1103/PhysRevA.59.4249) (cited on page 4).
- [11] Hugo Jacinto, Élie Gouzien, and Nicolas Sangouard. *Network Requirements for Distributed Quantum Computation*. Apr. 11, 2025. doi: [10.48550/arXiv.2504.08891](https://doi.org/10.48550/arXiv.2504.08891). URL: <http://arxiv.org/abs/2504.08891> (visited on 04/15/2025). Pre-published (cited on page 4).
- [12] D. Main et al. “Distributed Quantum Computing across an Optical Network Link.” In: *Nature* 638.8050 (Feb. 2025), pp. 383–388. doi: [10.1038/s41586-024-08404-x](https://doi.org/10.1038/s41586-024-08404-x) (cited on page 4).
- [13] A.M. Childs. “Secure Assisted Quantum Computation.” In: *Quantum Information and Computation* 5.6 (Sept. 2005), pp. 456–466. doi: [10.26421/QIC5.6-4](https://doi.org/10.26421/QIC5.6-4) (cited on page 4).
- [14] Vittorio Giovannetti et al. “Efficient Universal Blind Quantum Computation.” In: *Physical Review Letters* 111.23 (Dec. 3, 2013), p. 230501. doi: [10.1103/PhysRevLett.111.230501](https://doi.org/10.1103/PhysRevLett.111.230501) (cited on page 4).
- [15] Y.-C. Wei et al. “Universal Distributed Blind Quantum Computing with Solid-State Qubits.” In: *Science* 388.6746 (May 2025), pp. 509–513. doi: [10.1126/science.adu6894](https://doi.org/10.1126/science.adu6894) (cited on page 4).
- [16] Zachary Eldredge et al. “Optimal and Secure Measurement Protocols for Quantum Sensor Networks.” In: *Physical Review A* 97.4 (Apr. 23, 2018), p. 042337. doi: [10.1103/PhysRevA.97.042337](https://doi.org/10.1103/PhysRevA.97.042337) (cited on page 4).
- [17] Vittorio Giovannetti, Seth Lloyd, and Lorenzo Maccone. “Quantum-Enhanced Measurements: Beating the Standard Quantum Limit.” In: *Science* 306.5700 (Nov. 19, 2004), pp. 1330–1336. doi: [10.1126/science.1104149](https://doi.org/10.1126/science.1104149) (cited on page 4).
- [18] C. L. Degen, F. Reinhard, and P. Cappellaro. “Quantum Sensing.” In: *Reviews of Modern Physics* 89.3 (July 25, 2017), p. 035002. doi: [10.1103/RevModPhys.89.035002](https://doi.org/10.1103/RevModPhys.89.035002) (cited on page 4).
- [19] Daniel Gottesman, Thomas Jennewein, and Sarah Croke. “Longer-Baseline Telescopes Using Quantum Repeaters.” In: *Physical Review Letters* 109.7 (Aug. 16, 2012), p. 070503. doi: [10.1103/PhysRevLett.109.070503](https://doi.org/10.1103/PhysRevLett.109.070503) (cited on page 4).
- [20] E. T. Khabiboulline et al. “Optical Interferometry with Quantum Networks.” In: *Physical Review Letters* 123.7 (Aug. 15, 2019), p. 070504. doi: [10.1103/PhysRevLett.123.070504](https://doi.org/10.1103/PhysRevLett.123.070504) (cited on page 4).

- [21] The Event Horizon Telescope Collaboration et al. “First M87 Event Horizon Telescope Results. IV. Imaging the Central Supermassive Black Hole.” In: *The Astrophysical Journal Letters* 875.1 (Apr. 2019), p. L4. doi: [10.3847/2041-8213/ab0e85](https://doi.org/10.3847/2041-8213/ab0e85) (cited on page 4).
- [22] P. Kómár et al. “A Quantum Network of Clocks.” In: *Nature Physics* 10.8 (Aug. 2014), pp. 582–587. doi: [10.1038/nphys3000](https://doi.org/10.1038/nphys3000) (cited on page 4).
- [23] Steven Weinberg. “Testing Quantum Mechanics.” In: *Annals of Physics* 194.2 (Sept. 1, 1989), pp. 336–386. doi: [10.1016/0003-4916\(89\)90276-5](https://doi.org/10.1016/0003-4916(89)90276-5) (cited on page 4).
- [24] A. Einstein, B. Podolsky, and N. Rosen. “Can Quantum-Mechanical Description of Physical Reality Be Considered Complete?” In: *Physical Review* 47.10 (May 15, 1935), pp. 777–780. doi: [10.1103/PhysRev.47.777](https://doi.org/10.1103/PhysRev.47.777) (cited on page 4).
- [25] J. S. Bell. “On the Einstein Podolsky Rosen Paradox.” In: *Physics Physique Fizika* 1.3 (Nov. 1, 1964), pp. 195–200. doi: [10.1103/PhysicsPhysiqueFizika.1.195](https://doi.org/10.1103/PhysicsPhysiqueFizika.1.195) (cited on page 4).
- [26] John F. Clauser et al. “Proposed Experiment to Test Local Hidden-Variable Theories.” In: *Physical Review Letters* 23.15 (Oct. 13, 1969), pp. 880–884. doi: [10.1103/PhysRevLett.23.880](https://doi.org/10.1103/PhysRevLett.23.880) (cited on page 4).
- [27] B. Hensen et al. “Loophole-Free Bell Inequality Violation Using Electron Spins Separated by 1.3 Kilometres.” In: *Nature* 526.7575 (Oct. 2015), pp. 682–686. doi: [10.1038/nature15759](https://doi.org/10.1038/nature15759) (cited on page 4).
- [28] Simon Storz et al. “Loophole-Free Bell Inequality Violation with Superconducting Circuits.” In: *Nature* 617.7960 (May 2023), pp. 265–270. doi: [10.1038/s41586-023-05885-0](https://doi.org/10.1038/s41586-023-05885-0) (cited on page 4).
- [29] Zheng-Da Li et al. “Testing Real Quantum Theory in an Optical Quantum Network.” In: *Physical Review Letters* 128.4 (Jan. 24, 2022), p. 040402. doi: [10.1103/PhysRevLett.128.040402](https://doi.org/10.1103/PhysRevLett.128.040402) (cited on page 4).
- [30] Peter Shadbolt et al. “Testing Foundations of Quantum Mechanics with Photons.” In: *Nature Physics* 10.4 (Apr. 2014), pp. 278–286. doi: [10.1038/nphys2931](https://doi.org/10.1038/nphys2931) (cited on page 4).
- [31] C. M. Knaut et al. “Entanglement of Nanophotonic Quantum Memory Nodes in a Telecom Network.” In: *Nature* 629.8012 (May 2024), pp. 573–578. doi: [10.1038/s41586-024-07252-z](https://doi.org/10.1038/s41586-024-07252-z) (cited on pages 4, 5).
- [32] Jian-Long Liu et al. “Creation of Memory–Memory Entanglement in a Metropolitan Quantum Network.” In: *Nature* 629.8012 (May 2024), pp. 579–585. doi: [10.1038/s41586-024-07308-0](https://doi.org/10.1038/s41586-024-07308-0) (cited on pages 4, 5).
- [33] Stephan Kucera et al. “Demonstration of Quantum Network Protocols over a 14-Km Urban Fiber Link.” In: *npj Quantum Information* 10.1 (Sept. 14, 2024), p. 88. doi: [10.1038/s41534-024-00886-x](https://doi.org/10.1038/s41534-024-00886-x) (cited on pages 4, 5).
- [34] Arian J. Stolk et al. “Metropolitan-Scale Heralded Entanglement of Solid-State Qubits.” In: *Science Advances* 10.44 (Oct. 30, 2024), eadp6442. doi: [10.1126/sciadv.adp6442](https://doi.org/10.1126/sciadv.adp6442) (cited on pages 4, 5).
- [35] Johannes Nokkala, Jyrki Piilo, and Ginestra Bianconi. “Complex Quantum Networks: A Topical Review.” In: *Journal of Physics A: Mathematical and Theoretical* 57.23 (June 7, 2024), p. 233001. doi: [10.1088/1751-8121/ad41a6](https://doi.org/10.1088/1751-8121/ad41a6) (cited on page 4).
- [36] Koji Azuma et al. “Quantum Repeaters: From Quantum Networks to the Quantum Internet.” In: *Reviews of Modern Physics* 95.4 (Dec. 20, 2023), p. 045006. doi: [10.1103/RevModPhys.95.045006](https://doi.org/10.1103/RevModPhys.95.045006) (cited on page 5).
- [37] W. K. Wootters and W. H. Zurek. “A Single Quantum Cannot Be Cloned.” In: *Nature* 299.5886 (5886 Oct. 1982), pp. 802–803. doi: [10.1038/299802a0](https://doi.org/10.1038/299802a0) (cited on page 5).
- [38] D. Dieks. “Communication by EPR Devices.” In: *Physics Letters A* 92.6 (Nov. 22, 1982), pp. 271–272. doi: [10.1016/0375-9601\(82\)90084-6](https://doi.org/10.1016/0375-9601(82)90084-6) (cited on page 5).
- [39] M. Żukowski et al. ““Event-ready-detectors” Bell Experiment via Entanglement Swapping.” In: *Physical Review Letters* 71.26 (Dec. 27, 1993), pp. 4287–4290. doi: [10.1103/PhysRevLett.71.4287](https://doi.org/10.1103/PhysRevLett.71.4287) (cited on page 5).
- [40] Jian-Wei Pan et al. “Experimental Entanglement Swapping: Entangling Photons That Never Interacted.” In: *Physical Review Letters* 80.18 (May 4, 1998), pp. 3891–3894. doi: [10.1103/PhysRevLett.80.3891](https://doi.org/10.1103/PhysRevLett.80.3891) (cited on page 5).

- [41] H.-J. Briegel et al. “Quantum Repeaters: The Role of Imperfect Local Operations in Quantum Communication.” In: *Physical Review Letters* 81.26 (Dec. 28, 1998), pp. 5932–5935. DOI: [10.1103/PhysRevLett.81.5932](https://doi.org/10.1103/PhysRevLett.81.5932) (cited on page 5).
- [42] W. Dür et al. “Quantum Repeaters Based on Entanglement Purification.” In: *Physical Review A* 59.1 (Jan. 1, 1999), pp. 169–181. DOI: [10.1103/PhysRevA.59.169](https://doi.org/10.1103/PhysRevA.59.169) (cited on page 5).
- [43] W. Dür and H. J. Briegel. “Entanglement Purification and Quantum Error Correction.” In: *Reports on Progress in Physics* 70.8 (July 2007), p. 1381. DOI: [10.1088/0034-4885/70/8/R03](https://doi.org/10.1088/0034-4885/70/8/R03) (cited on page 5).
- [44] Veysel Bayrakci and Fatih Ozaydin. “Quantum Zeno Repeaters.” In: *Scientific Reports* 12.1 (1 Sept. 12, 2022), p. 15302. DOI: [10.1038/s41598-022-19170-z](https://doi.org/10.1038/s41598-022-19170-z) (cited on page 5).
- [45] V. Krutyanskiy et al. “Telecom-Wavelength Quantum Repeater Node Based on a Trapped-Ion Processor.” In: *Physical Review Letters* 130.21 (May 22, 2023), p. 213601. DOI: [10.1103/PhysRevLett.130.213601](https://doi.org/10.1103/PhysRevLett.130.213601) (cited on page 5).
- [46] Zheng-Da Li et al. “Experimental Quantum Repeater without Quantum Memory.” In: *Nature Photonics* 13.9 (9 Sept. 2019), pp. 644–648. DOI: [10.1038/s41566-019-0468-5](https://doi.org/10.1038/s41566-019-0468-5) (cited on page 5).
- [47] David D. Awschalom et al. “Quantum Technologies with Optically Interfaced Solid-State Spins.” In: *Nature Photonics* 12.9 (9 Sept. 2018), pp. 516–527. DOI: [10.1038/s41566-018-0232-2](https://doi.org/10.1038/s41566-018-0232-2) (cited on page 5).
- [48] Hans K.C. Beukers et al. “Remote-Entanglement Protocols for Stationary Qubits with Photonic Interfaces.” In: *PRX Quantum* 5.1 (Mar. 29, 2024), p. 010202. DOI: [10.1103/PRXQuantum.5.010202](https://doi.org/10.1103/PRXQuantum.5.010202) (cited on page 5).
- [49] Nicolas Sangouard et al. “Quantum Repeaters Based on Atomic Ensembles and Linear Optics.” In: *Reviews of Modern Physics* 83.1 (Mar. 21, 2011), pp. 33–80. DOI: [10.1103/RevModPhys.83.33](https://doi.org/10.1103/RevModPhys.83.33) (cited on page 5).
- [50] Jacob P. Covey, Harald Weinfurter, and Hannes Bernien. “Quantum Networks with Neutral Atom Processing Nodes.” In: *npj Quantum Information* 9.1 (Sept. 16, 2023), p. 90. DOI: [10.1038/s41534-023-00759-9](https://doi.org/10.1038/s41534-023-00759-9) (cited on page 5).
- [51] E. Togan et al. “Quantum Entanglement between an Optical Photon and a Solid-State Spin Qubit.” In: *Nature* 466.7307 (7307 Aug. 2010), pp. 730–734. DOI: [10.1038/nature09256](https://doi.org/10.1038/nature09256) (cited on page 5).
- [52] C. T. Nguyen et al. “Quantum Network Nodes Based on Diamond Qubits with an Efficient Nanophotonic Interface.” In: *Physical Review Letters* 123.18 (Oct. 30, 2019), p. 183602. DOI: [10.1103/PhysRevLett.123.183602](https://doi.org/10.1103/PhysRevLett.123.183602) (cited on page 5).
- [53] L. Bergeron et al. “Silicon-Integrated Telecommunications Photon-Spin Interface.” In: *PRX Quantum* 1.2 (Oct. 2, 2020), p. 020301. DOI: [10.1103/PRXQuantum.1.020301](https://doi.org/10.1103/PRXQuantum.1.020301) (cited on page 5).
- [54] Mohammad Mirhosseini et al. “Superconducting Qubit to Optical Photon Transduction.” In: *Nature* 588.7839 (Dec. 2020), pp. 599–603. DOI: [10.1038/s41586-020-3038-6](https://doi.org/10.1038/s41586-020-3038-6) (cited on page 5).
- [55] Changqing Wang et al. “High-Efficiency Microwave-Optical Quantum Transduction Based on a Cavity Electro-Optic Superconducting System with Long Coherence Time.” In: *npj Quantum Information* 8.1 (Dec. 21, 2022), p. 149. DOI: [10.1038/s41534-022-00664-7](https://doi.org/10.1038/s41534-022-00664-7) (cited on page 5).
- [56] I. N. Stranski and L. Krastanow. “Zur Theorie der orientierten Ausscheidung von Ionenkristallen aufeinander.” In: *Monatshefte für Chemie und verwandte Teile anderer Wissenschaften* 71.1 (Dec. 1, 1937), pp. 351–364. DOI: [10.1007/BF01798103](https://doi.org/10.1007/BF01798103) (cited on page 5).
- [57] Nobuyuki Koguchi, Satoshi Takahashi, and Toyohiro Chikyow. “New MBE Growth Method for InSb Quantum Well Boxes.” In: *Journal of Crystal Growth* 111.1 (May 2, 1991), pp. 688–692. DOI: [10.1016/0022-0248\(91\)91064-H](https://doi.org/10.1016/0022-0248(91)91064-H) (cited on page 5).
- [58] Nobuyuki Koguchi, Keiko Ishige, and Satoshi Takahashi. “New Selective Molecular-beam Epitaxial Growth Method for Direct Formation of GaAs Quantum Dots.” In: *Journal of Vacuum Science & Technology B: Microelectronics and Nanometer Structures Processing, Measurement, and Phenomena* 11.3 (May 1, 1993), pp. 787–790. DOI: [10.1116/1.586789](https://doi.org/10.1116/1.586789) (cited on page 5).
- [59] Nobuyuki Koguchi Nobuyuki Koguchi and Keiko Ishige Keiko Ishige. “Growth of GaAs Epitaxial Microcrystals on an S-Terminated GaAs Substrate by Successive Irradiation of Ga and As Molecular Beams.” In: *Japanese Journal of Applied Physics* 32 (5R May 1, 1993), p. 2052. DOI: [10.1143/JJAP.32.2052](https://doi.org/10.1143/JJAP.32.2052) (cited on page 5).

- [60] Richard J. Warburton. “Single Spins in Self-Assembled Quantum Dots.” In: *Nature Materials* 12.6 (June 2013), pp. 483–493. DOI: [10.1038/nmat3585](https://doi.org/10.1038/nmat3585) (cited on page 5).
- [61] Guido Burkard et al. “Semiconductor Spin Qubits.” In: *Reviews of Modern Physics* 95.2 (June 14, 2023), p. 025003. DOI: [10.1103/RevModPhys.95.025003](https://doi.org/10.1103/RevModPhys.95.025003) (cited on page 6).
- [62] Peter Stano and Daniel Loss. *Review of Performance Metrics of Spin Qubits in Gated Semiconducting Nanostructures*. Mar. 24, 2025. DOI: [10.48550/arXiv.2107.06485](https://doi.org/10.48550/arXiv.2107.06485). URL: <http://arxiv.org/abs/2107.06485> (visited on 03/24/2025). Pre-published (cited on page 6).
- [63] Benjamin Jöcker et al. “Transfer of a Quantum State from a Photonic Qubit to a Gate-Defined Quantum Dot.” In: *Physical Review B* 99.20 (May 13, 2019), p. 205415. DOI: [10.1103/PhysRevB.99.205415](https://doi.org/10.1103/PhysRevB.99.205415) (cited on page 6).
- [64] Thomas Descamps. “Electrostatic Exciton Trap in a Thin Semiconductor Membrane for Optical Coupling to a GaAs Spin Qubit.” PhD thesis. Aachen: RWTH Aachen University, 2021 (cited on pages 6, 8, 12, 13, 24, 26–29, 32, 36, 42, 44, 48).
- [65] Thomas Descamps et al. “Semiconductor Membranes for Electrostatic Exciton Trapping in Optically Addressable Quantum Transport Devices.” In: *Physical Review Applied* 19.4 (Apr. 28, 2023), p. 044095. DOI: [10.1103/PhysRevApplied.19.044095](https://doi.org/10.1103/PhysRevApplied.19.044095) (cited on pages 6, 27).
- [66] I. Vurgaftman, J. R. Meyer, and L. R. Ram-Mohan. “Band Parameters for III–V Compound Semiconductors and Their Alloys.” In: *Journal of Applied Physics* 89.11 (June 2001), pp. 5815–5875. DOI: [10.1063/1.1368156](https://doi.org/10.1063/1.1368156) (cited on pages 8, 26).
- [67] Thomas Ihn. *Semiconductor Nanostructures: Quantum States and Electronic Transport*. Oxford University Press, Nov. 26, 2009 (cited on pages 8, 26).
- [68] Horst L. Stormer. “Nobel Lecture: The Fractional Quantum Hall Effect.” In: *Reviews of Modern Physics* 71.4 (July 1, 1999), pp. 875–889. DOI: [10.1103/RevModPhys.71.875](https://doi.org/10.1103/RevModPhys.71.875) (cited on page 8).
- [69] R. H. Harrell et al. “Fabrication of High-Quality One- and Two-Dimensional Electron Gases in Undoped GaAs/AlGaAs Heterostructures.” In: *Applied Physics Letters* 74.16 (Apr. 19, 1999), pp. 2328–2330. DOI: [10.1063/1.123840](https://doi.org/10.1063/1.123840) (cited on page 8).
- [70] J. C. H. Chen et al. “Fabrication and Characterization of Ambipolar Devices on an Undoped AlGaAs/-GaAs Heterostructure.” In: *Applied Physics Letters* 100.5 (Jan. 30, 2012), p. 052101. DOI: [10.1063/1.3673837](https://doi.org/10.1063/1.3673837) (cited on page 8).
- [71] Hai-Ou Li et al. “Fabrication and Characterization of an Undoped GaAs/AlGaAs Quantum Dot Device.” In: *Journal of Applied Physics* 116.17 (Nov. 3, 2014), p. 174504. DOI: [10.1063/1.4900915](https://doi.org/10.1063/1.4900915) (cited on page 8).
- [72] L. A. Tracy, T. W. Hargett, and J. L. Reno. “Few-Hole Double Quantum Dot in an Undoped GaAs/AlGaAs Heterostructure.” In: *Applied Physics Letters* 104.12 (Mar. 24, 2014), p. 123101. DOI: [10.1063/1.4868971](https://doi.org/10.1063/1.4868971) (cited on page 8).
- [73] Matthias E. Röbber. “Contacting Backgated Two-dimensional Electron Gases for Quantum Dot Spin Qubits in GaAs.” MA thesis. Aachen: RWTH Aachen University, Sept. 2016 (cited on page 8).
- [74] Sebastian Kindel. PhD thesis. Aachen: RWTH Aachen University, 2025 (cited on pages 8, 24).
- [75] Takafumi Fujita et al. “Distinguishing Persistent Effects in an Undoped GaAs/AlGaAs Quantum Well by Top-Gate-Dependent Illumination.” In: *Journal of Applied Physics* 129.23 (June 21, 2021), p. 234301. DOI: [10.1063/5.0047558](https://doi.org/10.1063/5.0047558) (cited on page 8).
- [76] A. Shetty et al. “Effects of Biased and Unbiased Illuminations on Two-Dimensional Electron Gases in Dopant-Free GaAs/AlGaAs.” In: *Physical Review B* 105.7 (Feb. 7, 2022), p. 075302. DOI: [10.1103/PhysRevB.105.075302](https://doi.org/10.1103/PhysRevB.105.075302) (cited on page 8).
- [77] Huiyi Wang. “Stability Investigation of GaAs Quantum Dot Devices under Illumination.” MA thesis. Aachen: RWTH Aachen University, Nov. 4, 2023. 65 pp. (cited on page 8).
- [78] Maxim Reznikov. “Investigating Device Stability and Exploring New Materials for Semiconductor Spin Qubit Optical Interfaces.” MA thesis. Aachen: RWTH Aachen University, June 2024 (cited on pages 8, 44).
- [79] R. C. Miller, D. A. Kleinman, and A. C. Gossard. “Energy-Gap Discontinuities and Effective Masses for GaAs – Al_xGa_{1-x}As Quantum Wells.” In: *Physical Review B* 29.12 (June 15, 1984), pp. 7085–7087. DOI: [10.1103/PhysRevB.29.7085](https://doi.org/10.1103/PhysRevB.29.7085) (cited on pages 9, 10).

- [80] John H. Davies. *The Physics of Low-Dimensional Semiconductors: An Introduction*. Cambridge: Cambridge Univ. Press, 2009. 438 pp. (cited on pages 9, 11–13).
- [81] D. Kamburov et al. “Use of Micro-Photoluminescence as a Contactless Measure of the 2D Electron Density in a GaAs Quantum Well.” In: *Applied Physics Letters* 110.26 (June 26, 2017), p. 262104. doi: [10.1063/1.4985439](https://doi.org/10.1063/1.4985439) (cited on pages 9, 25, 26).
- [82] G. D. Mahan. “Excitons in Metals.” In: *Physical Review Letters* 18.12 (Mar. 20, 1967), pp. 448–450. doi: [10.1103/PhysRevLett.18.448](https://doi.org/10.1103/PhysRevLett.18.448) (cited on page 9).
- [83] G. D. Mahan. “Excitons in Degenerate Semiconductors.” In: *Physical Review* 153.3 (Jan. 15, 1967), pp. 882–889. doi: [10.1103/PhysRev.153.882](https://doi.org/10.1103/PhysRev.153.882) (cited on pages 9, 42).
- [84] M. S. Skolnick et al. “Observation of a Many-Body Edge Singularity in Quantum-Well Luminescence Spectra.” In: *Physical Review Letters* 58.20 (May 18, 1987), pp. 2130–2133. doi: [10.1103/PhysRevLett.58.2130](https://doi.org/10.1103/PhysRevLett.58.2130) (cited on pages 9, 26).
- [85] T. Mélin and F. Laruelle. “Fermi-Edge Singularities in $\text{Al}_x\text{Ga}_{1-x}\text{As}$ Quantum Wells: Extrinsic versus Many-Body Scattering Processes.” In: *Physical Review Letters* 85.4 (July 24, 2000), pp. 852–855. doi: [10.1103/PhysRevLett.85.852](https://doi.org/10.1103/PhysRevLett.85.852) (cited on page 9).
- [86] A. Gabbay et al. “Effect of Valence Subband Dispersion on Near-Band-Gap Transitions in $\text{GaAs} / \text{Al}_x\text{Ga}_{1-x}\text{As}$ Quantum Wells Containing a Two-Dimensional Electron Gas.” In: *Physical Review B* 77.16 (Apr. 21, 2008), p. 165329. doi: [10.1103/PhysRevB.77.165329](https://doi.org/10.1103/PhysRevB.77.165329) (cited on pages 9, 26).
- [87] Lucio Claudio Andreani and Alfredo Pasquarello. “Accurate Theory of Excitons in $\text{GaAs-Ga}_{1-x}\text{Al}_x\text{As}$ Quantum Wells.” In: *Physical Review B* 42.14 (Nov. 15, 1990), pp. 8928–8938. doi: [10.1103/PhysRevB.42.8928](https://doi.org/10.1103/PhysRevB.42.8928) (cited on page 9).
- [88] G. D. Gilliland. “Photoluminescence Spectroscopy of Crystalline Semiconductors.” In: *Materials Science and Engineering: R: Reports* 18.3 (1997), pp. 99–399. doi: [10.1016/S0927-796X\(97\)80003-4](https://doi.org/10.1016/S0927-796X(97)80003-4) (cited on pages 9, 33).
- [89] Tania Palmieri et al. “Mahan Excitons in Room-Temperature Methylammonium Lead Bromide Perovskites.” In: *Nature Communications* 11.1 (Feb. 12, 2020), p. 850. doi: [10.1038/s41467-020-14683-5](https://doi.org/10.1038/s41467-020-14683-5) (cited on page 9).
- [90] N. F. Mott. “Metal-Insulator Transition.” In: *Reviews of Modern Physics* 40.4 (Oct. 1, 1968), pp. 677–683. doi: [10.1103/RevModPhys.40.677](https://doi.org/10.1103/RevModPhys.40.677) (cited on page 9).
- [91] André Schleife et al. “Optical Absorption in Degenerately Doped Semiconductors: Mott Transition or Mahan Excitons?” In: *Physical Review Letters* 107.23 (Nov. 30, 2011), p. 236405. doi: [10.1103/PhysRevLett.107.236405](https://doi.org/10.1103/PhysRevLett.107.236405) (cited on page 9).
- [92] Thomas Olsen et al. “Simple Screened Hydrogen Model of Excitons in Two-Dimensional Materials.” In: *Physical Review Letters* 116.5 (Feb. 2, 2016), p. 056401. doi: [10.1103/PhysRevLett.116.056401](https://doi.org/10.1103/PhysRevLett.116.056401) (cited on page 10).
- [93] D. A. B. Miller et al. “Band-Edge Electroabsorption in Quantum Well Structures: The Quantum-Confined Stark Effect.” In: *Physical Review Letters* 53.22 (Nov. 26, 1984), pp. 2173–2176. doi: [10.1103/PhysRevLett.53.2173](https://doi.org/10.1103/PhysRevLett.53.2173) (cited on pages 10, 11, 14).
- [94] A. Rabinovitch and J. Zak. “Electrons in Crystals in a Finite-Range Electric Field.” In: *Physical Review B* 4.8 (Oct. 15, 1971), pp. 2358–2370. doi: [10.1103/PhysRevB.4.2358](https://doi.org/10.1103/PhysRevB.4.2358) (cited on page 11).
- [95] D. A. B. Miller et al. “Electric Field Dependence of Optical Absorption near the Band Gap of Quantum-Well Structures.” In: *Physical Review B* 32.2 (July 15, 1985), pp. 1043–1060. doi: [10.1103/PhysRevB.32.1043](https://doi.org/10.1103/PhysRevB.32.1043) (cited on page 11).
- [96] A. V. Kavokin. “Exciton Oscillator Strength in Quantum Wells: From Localized to Free Resonant States.” In: *Physical Review B* 50.11 (Sept. 15, 1994), pp. 8000–8003. doi: [10.1103/PhysRevB.50.8000](https://doi.org/10.1103/PhysRevB.50.8000) (cited on pages 12, 13).
- [97] E. Karimi et al. “Radial Quantum Number of Laguerre-Gauss Modes.” In: *Physical Review A* 89.6 (June 16, 2014), p. 063813. doi: [10.1103/PhysRevA.89.063813](https://doi.org/10.1103/PhysRevA.89.063813) (cited on page 12).
- [98] Robert C. Hilborn. “Einstein Coefficients, Cross Sections, f Values, Dipole Moments, and All That.” In: *American Journal of Physics* 50.11 (Nov. 1, 1982), pp. 982–986. doi: [10.1119/1.12937](https://doi.org/10.1119/1.12937) (cited on page 13).

- [99] A. Larsson et al. “Tunable Superlattice P-i-n Photodetectors: Characteristics, Theory, and Application.” In: *IEEE Journal of Quantum Electronics* 24.5 (May 1988), pp. 787–801. doi: [10.1109/3.195](#) (cited on pages 13, 28).
- [100] R. C. Miller and D. A. Kleinman. “Excitons in GaAs Quantum Wells.” In: *Journal of Luminescence* 30.1 (Feb. 1, 1985), pp. 520–540. doi: [10.1016/0022-2313\(85\)90075-4](#) (cited on page 14).
- [101] Satoshi Kako et al. “Biexciton in Single GaN/AlN Self-Assembled Quantum Dots.” In: *Conference on Lasers and Electro-Optics/International Quantum Electronics Conference and Photonic Applications Systems Technologies*. International Quantum Electronics Conference. San Francisco, California: OSA, 2004, IThC5. doi: [10.1364/IQEC.2004.IThC5](#) (cited on page 14).
- [102] G.E. Dialynas et al. “Anti-Binding of Biexcitons in (211)B InAs/GaAs Piezoelectric Quantum Dots.” In: *Physica E: Low-dimensional Systems and Nanostructures* 40.6 (Apr. 2008), pp. 2113–2115. doi: [10.1016/j.physe.2007.10.036](#) (cited on page 14).
- [103] S. Amloy et al. “Size Dependent Biexciton Binding Energies in GaN Quantum Dots.” In: *Applied Physics Letters* 99.25 (Dec. 19, 2011), p. 251903. doi: [10.1063/1.3670040](#) (cited on page 14).
- [104] Gleb Finkelstein, Hadas Shtrikman, and Israel Bar-Joseph. “Optical Spectroscopy of a Two-Dimensional Electron Gas near the Metal-Insulator Transition.” In: *Physical Review Letters* 74.6 (Feb. 6, 1995), pp. 976–979. doi: [10.1103/PhysRevLett.74.976](#) (cited on page 15).
- [105] Axel Esser et al. “Photoluminescence and Radiative Lifetime of Trions in GaAs Quantum Wells.” In: *Physical Review B* 62.12 (Sept. 15, 2000), pp. 8232–8239. doi: [10.1103/PhysRevB.62.8232](#) (cited on pages 15, 35).
- [106] Israel Bar-Joseph. “Trions in GaAs Quantum Wells.” In: *Semiconductor Science and Technology* 20.6 (June 1, 2005), R29–R39. doi: [10.1088/0268-1242/20/6/R01](#) (cited on page 15).
- [107] Tobias Hangleiter, *Mjolnir* Aug. 8, 2025 (cited on page 16).
- [108] Thorlabs. *NDC-25C-4 Unmounted Continuously Variable ND Filter, Ø25 mm, OD: 0.04 - 4.0*. URL: <https://www.thorlabs.com/thorproduct.cfm?partnumber=NDC-25C-4> (visited on 08/11/2025) (cited on page 19).
- [109] Andreas Mayer et al. “Diversity of Immune Strategies Explained by Adaptation to Pathogen Statistics.” In: *Proceedings of the National Academy of Sciences* 113.31 (Aug. 2, 2016), pp. 8630–8635. doi: [10.1073/pnas.1600663113](#) (cited on page 20).
- [110] Tobias Hangleiter et al., *Qutil* version 2024.11.1, Nov. 21, 2024. Zenodo. doi: [10.5281/ZENODO.14200303](#) (cited on page 22).
- [111] Elias Burstein. “Anomalous Optical Absorption Limit in InSb.” In: *Physical Review* 93.3 (Feb. 1, 1954), pp. 632–633. doi: [10.1103/PhysRev.93.632](#) (cited on page 25).
- [112] T. S. Moss. “The Interpretation of the Properties of Indium Antimonide.” In: *Proceedings of the Physical Society. Section B* 67.10 (Oct. 1954), p. 775. doi: [10.1088/0370-1301/67/10/306](#) (cited on page 25).
- [113] A. Pinczuk et al. “Optical Processes of 2D Electron Plasma in GaAs-(AlGa)As Heterostructures.” In: *Solid State Communications* 50.8 (May 1, 1984), pp. 735–739. doi: [10.1016/0038-1098\(84\)90975-X](#) (cited on pages 25, 26).
- [114] R. Ulbrich. “Energy Relaxation of Photoexcited Hot Electrons in GaAs.” In: *Physical Review B* 8.12 (Dec. 15, 1973), pp. 5719–5727. doi: [10.1103/PhysRevB.8.5719](#) (cited on page 25).
- [115] U. Bockelmann and G. Bastard. “Phonon Scattering and Energy Relaxation in Two-, One-, and Zero-Dimensional Electron Gases.” In: *Physical Review B* 42.14 (Nov. 15, 1990), pp. 8947–8951. doi: [10.1103/PhysRevB.42.8947](#) (cited on page 25).
- [116] Hendrik Bluhm, *poisson_schroedinger_1D* May 14, 2024 (cited on pages 26, 49).
- [117] S. C. Jain et al. “Modified Simple Expression for Bandgap Narrowing in N-Type GaAs.” In: *Solid-State Electronics* 35.5 (May 1, 1992), pp. 639–642. doi: [10.1016/0038-1101\(92\)90030-G](#) (cited on page 26).
- [118] G.N. Nguyen et al. “Influence of Molecular Beam Effusion Cell Quality on Optical and Electrical Properties of Quantum Dots and Quantum Wells.” In: *Journal of Crystal Growth* 550 (Nov. 2020), p. 125884. doi: [10.1016/j.jcrysgro.2020.125884](#) (cited on page 27).
- [119] C. Volk et al. “Loading a Quantum-Dot Based “Qubyte” Register.” In: *npj Quantum Information* 5.1 (Dec. 2019), p. 29. doi: [10.1038/s41534-019-0146-y](#) (cited on page 28).

- [120] H. Schneider and K. V. Klitzing. “Thermionic Emission and Gaussian Transport of Holes in a GaAs/Al_xGa_{1-x}As Multiple-Quantum-Well Structure.” In: *Physical Review B* 38.9 (Sept. 15, 1988), pp. 6160–6165. doi: [10.1103/PhysRevB.38.6160](#) (cited on page 28).
- [121] A.M. Fox et al. “Quantum Well Carrier Sweep out: Relation to Electroabsorption and Exciton Saturation.” In: *IEEE Journal of Quantum Electronics* 27.10 (Oct. 1991), pp. 2281–2295. doi: [10.1109/3.97272](#) (cited on page 28).
- [122] *Voigt Profile*. In: *Wikipedia*. June 12, 2025 (cited on page 29).
- [123] M. L. Citron et al. “Experimental Study of Power Broadening in a Two-Level Atom.” In: *Physical Review A* 16.4 (Oct. 1, 1977), pp. 1507–1512. doi: [10.1103/PhysRevA.16.1507](#) (cited on page 29).
- [124] M. Tanaka and H. Sakaki. “Atomistic Models of Interface Structures of GaAs-Al_xGa_{1-x}As ($x = 0.2-1$) Quantum Wells Grown by Interrupted and Uninterrupted MBE.” In: *Journal of Crystal Growth* 81.1 (Feb. 2, 1987), pp. 153–158. doi: [10.1016/0022-0248\(87\)90383-6](#) (cited on page 31).
- [125] D. Gammon, B. V. Shanabrook, and D. S. Katzer. “Excitons, Phonons, and Interfaces in GaAs/AlAs Quantum-Well Structures.” In: *Physical Review Letters* 67.12 (Sept. 16, 1991), pp. 1547–1550. doi: [10.1103/PhysRevLett.67.1547](#) (cited on pages 31, 35).
- [126] K. Leosson et al. “Exciton Localization and Interface Roughness in Growth-Interrupted GaAs/AlAs Quantum Wells.” In: *Physical Review B* 61.15 (Apr. 15, 2000), pp. 10322–10329. doi: [10.1103/PhysRevB.61.10322](#) (cited on page 31).
- [127] K. Brunner et al. “Sharp-Line Photoluminescence and Two-Photon Absorption of Zero-Dimensional Biexcitons in a GaAs/AlGaAs Structure.” In: *Physical Review Letters* 73.8 (Aug. 22, 1994), pp. 1138–1141. doi: [10.1103/PhysRevLett.73.1138](#) (cited on page 31).
- [128] K. Brunner et al. “Sharp-Line Photoluminescence of Excitons Localized at GaAs/AlGaAs Quantum Well Inhomogeneities.” In: *Applied Physics Letters* 64.24 (June 13, 1994), pp. 3320–3322. doi: [10.1063/1.111265](#) (cited on page 31).
- [129] A. Zrenner et al. “Quantum Dots Formed by Interface Fluctuations in AlAs/GaAs Coupled Quantum Well Structures.” In: *Physical Review Letters* 72.21 (May 23, 1994), pp. 3382–3385. doi: [10.1103/PhysRevLett.72.3382](#) (cited on page 31).
- [130] G. Bastard et al. “Low-Temperature Exciton Trapping on Interface Defects in Semiconductor Quantum Wells.” In: *Physical Review B* 29.12 (June 15, 1984), pp. 7042–7044. doi: [10.1103/PhysRevB.29.7042](#) (cited on page 33).
- [131] R. C. Miller et al. “New Evidence of Extensive Valence-Band Mixing in GaAs Quantum Wells through Excitation Photoluminescence Studies.” In: *Physical Review B* 32.12 (Dec. 15, 1985), pp. 8452–8454. doi: [10.1103/PhysRevB.32.8452](#) (cited on page 33).
- [132] F. Laruelle and B. Etienne. “Optical Investigation of the Heavy Hole-Light Hole Splitting in Thin GaAs/GaAlAs Quantum Wells.” In: *Solid State Communications* 65.7 (Feb. 1, 1988), pp. 565–569. doi: [10.1016/0038-1098\(88\)90339-0](#) (cited on page 33).
- [133] D. C. Reynolds et al. “Well-Resolved Higher Excited States of the Light- and Heavy-Hole Free Excitons in a 225-Å Al_xGa_{1-x}As-GaAs Multi-Quantum-Well Structure.” In: *Physical Review B* 37.6 (Feb. 15, 1988), pp. 3117–3119. doi: [10.1103/PhysRevB.37.3117](#) (cited on page 33).
- [134] Y. El Khalifi et al. “Dependence of the Light-Hole–Heavy-Hole Splitting on Layer Thickness and Substrate Orientation in GaAs-(GaAl) As Single Quantum Wells.” In: *Physical Review B* 39.18 (June 15, 1989), pp. 13533–13536. doi: [10.1103/PhysRevB.39.13533](#) (cited on pages 33, 35).
- [135] R. T. Collins, K. v. Klitzing, and K. Ploog. “Photocurrent Spectroscopy of GaAs/Al_xGa_{1-x}As Quantum Wells in an Electric Field.” In: *Physical Review B* 33.6 (Mar. 15, 1986), pp. 4378–4381. doi: [10.1103/PhysRevB.33.4378](#) (cited on page 33).
- [136] R. T. Collins et al. “Mixing between Heavy-Hole and Light-Hole Excitons in GaAs/Al_xGa_{1-x}As Quantum Wells in an Electric Field.” In: *Physical Review B* 36.3 (July 15, 1987), pp. 1531–1534. doi: [10.1103/PhysRevB.36.1531](#) (cited on page 33).
- [137] A. Esser, R. Zimmermann, and E. Runge. “Theory of Trion Spectra in Semiconductor Nanostructures.” In: *physica status solidi (b)* 227.2 (Oct. 2001), pp. 317–330. doi: [10.1002/1521-3951\(200110\)227:2<317::AID-PSSB317>3.0.CO;2-S](#) (cited on pages 34–36).

- [138] S. A. Brown et al. “Evolution of the Interband Absorption Threshold with the Density of a Two-Dimensional Electron Gas.” In: *Physical Review B* 54.16 (Oct. 15, 1996), R11082–R11085. DOI: [10.1103/PhysRevB.54.R11082](https://doi.org/10.1103/PhysRevB.54.R11082) (cited on page 35).
- [139] V. Huard et al. “Bound States in Optical Absorption of Semiconductor Quantum Wells Containing a Two-Dimensional Electron Gas.” In: *Physical Review Letters* 84.1 (Jan. 3, 2000), pp. 187–190. DOI: [10.1103/PhysRevLett.84.187](https://doi.org/10.1103/PhysRevLett.84.187) (cited on page 35).
- [140] G. Yusa, H. Shtrikman, and I. Bar-Joseph. “Onset of Exciton Absorption in Modulation-Doped GaAs Quantum Wells.” In: *Physical Review B* 62.23 (Dec. 15, 2000), pp. 15390–15393. DOI: [10.1103/PhysRevB.62.15390](https://doi.org/10.1103/PhysRevB.62.15390) (cited on page 35).
- [141] I. Essaoudi, B. Stébé, and A. Ainane. “Quantum-Confined Stark Effects of an Exciton Bound to an Ionized Donor in a GaAs/Ga_{1-x}Al_xAs Quantum Well.” In: *Physical Review B* 64.23 (Nov. 16, 2001), p. 235311. DOI: [10.1103/PhysRevB.64.235311](https://doi.org/10.1103/PhysRevB.64.235311) (cited on page 35).
- [142] M. N. Bataev et al. “Heavy-Hole–Light-Hole Exciton System in GaAs/AlGaAs Quantum Wells.” In: *Physical Review B* 106.8 (Aug. 10, 2022), p. 085407. DOI: [10.1103/PhysRevB.106.085407](https://doi.org/10.1103/PhysRevB.106.085407) (cited on page 35).
- [143] D. Strauch and B. Dorner. “Phonon Dispersion in GaAs.” In: *Journal of Physics: Condensed Matter* 2.6 (Feb. 1990), p. 1457. DOI: [10.1088/0953-8984/2/6/006](https://doi.org/10.1088/0953-8984/2/6/006) (cited on page 35).
- [144] M. Ilegems and G. L. Pearson. “Infrared Reflection Spectra of Ga_{1-x}Al_xAs Mixed Crystals.” In: *Physical Review B* 1.4 (Feb. 15, 1970), pp. 1576–1582. DOI: [10.1103/PhysRevB.1.1576](https://doi.org/10.1103/PhysRevB.1.1576) (cited on page 35).
- [145] J. Leng et al. “Disorder Activated Optical Modes and the Phonon Dispersion of Al_xGa_{1-x}As Lattice Vibration.” In: *Solid State Communications* 69.3 (Jan. 1, 1989), pp. 311–315. DOI: [10.1016/0038-1098\(89\)90858-2](https://doi.org/10.1016/0038-1098(89)90858-2) (cited on page 35).
- [146] B. N. Murdin et al. “Direct Observation of the LO Phonon Bottleneck in Wide GaAs/Al_xGa_{1-x}As Quantum Wells.” In: *Physical Review B* 55.8 (Feb. 15, 1997), pp. 5171–5176. DOI: [10.1103/PhysRevB.55.5171](https://doi.org/10.1103/PhysRevB.55.5171) (cited on page 36).
- [147] Denis Langevin et al. “PyMoosh: A Comprehensive Numerical Toolkit for Computing the Optical Properties of Multilayered Structures.” In: *Journal of the Optical Society of America B* 41.2 (Feb. 1, 2024), A67. DOI: [10.1364/JOSAB.506175](https://doi.org/10.1364/JOSAB.506175) (cited on pages 36–38).
- [148] Denny Dütz et al. “Distributed Bragg Reflectors for Thermal Isolation of Semiconductor Spin Qubits.” In preparation (cited on page 38).
- [149] A. D’Andrea and R. Del Sole. “Exciton Quantization and Polariton Propagation in Semiconductor Slabs: From Semi-Infinite Crystals to Quantum Wells.” In: *Physical Review B* 41.3 (Jan. 15, 1990), pp. 1413–1423. DOI: [10.1103/PhysRevB.41.1413](https://doi.org/10.1103/PhysRevB.41.1413) (cited on page 38).
- [150] Dmitry I. Yakubovsky et al. “Optical Constants and Structural Properties of Thin Gold Films.” In: *Optics Express* 25.21 (Oct. 16, 2017), pp. 25574–25587. DOI: [10.1364/OE.25.025574](https://doi.org/10.1364/OE.25.025574) (cited on page 39).
- [151] Kevin J. Palm et al. “Dynamic Optical Properties of Metal Hydrides.” In: *ACS Photonics* 5.11 (Nov. 21, 2018), pp. 4677–4686. DOI: [10.1021/acsp Photonics.8b01243](https://doi.org/10.1021/acsp Photonics.8b01243) (cited on page 39).
- [152] Konstantinos Papatryfonos et al. “Refractive Indices of MBE-grown Al_xGa_(1-x)As Ternary Alloys in the Transparent Wavelength Region.” In: *AIP Advances* 11.2 (Feb. 18, 2021), p. 025327. DOI: [10.1063/5.0039631](https://doi.org/10.1063/5.0039631) (cited on page 39).
- [153] Mikhail N. Polyanskiy. “Refractiveindex.Info Database of Optical Constants.” In: *Scientific Data* 11.1 (Jan. 18, 2024), p. 94. DOI: [10.1038/s41597-023-02898-2](https://doi.org/10.1038/s41597-023-02898-2) (cited on page 39).
- [154] Maarten Baeten and Michiel Wouters. “Many-Body Effects of a Two-Dimensional Electron Gas on Trion-Polaritons.” In: *Physical Review B* 91.11 (Mar. 23, 2015), p. 115313. DOI: [10.1103/PhysRevB.91.115313](https://doi.org/10.1103/PhysRevB.91.115313) (cited on page 44).
- [155] M. M. Glazov. “Optical Properties of Charged Excitons in Two-Dimensional Semiconductors.” In: *The Journal of Chemical Physics* 153.3 (July 21, 2020), p. 034703. DOI: [10.1063/5.0012475](https://doi.org/10.1063/5.0012475) (cited on page 44).
- [156] Di Huang et al. “Quantum Dynamics of Attractive and Repulsive Polarons in a Doped MoSe₂ Monolayer.” In: *Physical Review X* 13.1 (Mar. 2, 2023), p. 011029. DOI: [10.1103/PhysRevX.13.011029](https://doi.org/10.1103/PhysRevX.13.011029) (cited on page 44).

Special Terms

Numbers

2DEG two-dimensional electron gas. iv, 8, 9, 14, 15, 25–29, 32–35, 42–44, 50

2DHG two-dimensional hole gas. 15

A

APD avalanche photodiode. 20, 42

B

BS beam splitter. 21

C

CCD charge-coupled device. 17–24, 42

CMOS complementary metal-oxide-semiconductor. 24

cw continuous-wave. 16, 19, 24, 42

D

DAC digital-to-analog converter. 18

DPSS diode-pumped solid state. 17

DR dilution refrigerator. 24

DUT device under test. 17, 18

E

EBL electron-beam lithography. 24, 26

EPR Einstein-Podolsky-Rosen. 4, 5

F

FES Fermi-edge singularity. 9, 26, 33, 36, 42

FWHM full width at half maximum. 31

G

GDQD gate-defined quantum dot. 6, 8

GUI graphical user interface. 22, 23

L

LD Loss-DiVincenzo. 6

M

MBE molecular beam epitaxy. 49

MMF multi-mode fiber. 25

N

ND neutral-density. 17–20

NIR near-infrared. 8

O

OAQD optically active quantum dot. 5, 6, 8

OD optical density. 19, 20

P

PL photoluminescence. iv, 6–9, 15, 16, 22, 24–28, 30–36, 39, 41–45, 48–50

PLE photoluminescence excitation. iv, 7, 33–36, 43, 44, 49

PTR pulse tube refrigerator. 20

Q

QCSE quantum-confined Stark effect. 6, 10–12, 14, 42, 43

QD quantum dot. 5, 6, 31
QEC quantum error correction. 5
QW quantum well. 6, 9–15, 24–28, 31–33, 35, 39–44, 48–50

R

RF resonance-fluorescence. 44
RMS root mean square. 20, 24

S

SAQD self-assembled quantum dot. 5, 6, 29
SMF single-mode fiber. 24, 25
SNR signal-to-noise ratio. 20, 33
ST singlet-triplet. 6

T

TE transverse electric. 37, 38
TMM transfer-matrix method. iv, 32, 36–38, 44, 48
TO transverse optical. 35

Declaration of Authorship

I, Tobias Hangleiter, declare that this thesis and the work presented in it are my own and has been generated by me as the result of my own original research.

I do solemnly swear that:

1. This work was done wholly or mainly while in candidature for the doctoral degree at this faculty and university;
2. Where any part of this thesis has previously been submitted for a degree or any other qualification at this university or any other institution, this has been clearly stated;
3. Where I have consulted the published work of others or myself, this is always clearly attributed;
4. Where I have quoted from the work of others or myself, the source is always given. This thesis is entirely my own work, with the exception of such quotations;
5. I have acknowledged all major sources of assistance;
6. Where the thesis is based on work done by myself jointly with others, I have made clear exactly what was done by others and what I have contributed myself;
7. Parts of this work have been published before as:

- [1] Pascal Cerfontaine, Tobias Hangleiter, and Hendrik Bluhm. “Filter Functions for Quantum Processes under Correlated Noise.” In: *Physical Review Letters* 127.17 (Oct. 18, 2021), p. 170403. doi: [10.1103/PhysRevLett.127.170403](https://doi.org/10.1103/PhysRevLett.127.170403).
- [2] Thomas Descamps, Feng Liu, Tobias Hangleiter, Sebastian Kindel, Beata E. Kardynał, and Hendrik Bluhm. “Millikelvin Confocal Microscope with Free-Space Access and High-Frequency Electrical Control.” In: *Review of Scientific Instruments* 95.8 (Aug. 9, 2024), p. 083706. doi: [10.1063/5.0200889](https://doi.org/10.1063/5.0200889).
- [3] Tobias Hangleiter, Pascal Cerfontaine, and Hendrik Bluhm. “Filter-Function Formalism and Software Package to Compute Quantum Processes of Gate Sequences for Classical Non-Markovian Noise.” In: *Physical Review Research* 3.4 (Oct. 18, 2021), p. 043047. doi: [10.1103/PhysRevResearch.3.043047](https://doi.org/10.1103/PhysRevResearch.3.043047).
- [4] Tobias Hangleiter, Pascal Cerfontaine, and Hendrik Bluhm. “Erratum: Filter-function Formalism and Software Package to Compute Quantum Processes of Gate Sequences for Classical Non-Markovian Noise [Phys. Rev. Research 3, 043047 (2021)].” In: *Physical Review Research* 6.4 (Oct. 16, 2024), p. 049001. doi: [10.1103/PhysRevResearch.6.049001](https://doi.org/10.1103/PhysRevResearch.6.049001).

Aachen, August 15, 2025.